Resonance Raman Spectroscopy of Single-Walled Carbon Nanotubes

by

Sandra Dawn Marie Brown

B.A./M.A., Hunter College of CUNY (1994)

Submitted to the Department of Physics
in partial fulfillment of the requirements for the degree of

Doctor of Philosophy in Physics

at the

MASSACHUSETTS INSTITUTE OF TECHNOLOGY

May 2000
[June 2000]

Author .....
Department of Physics
May 11, 2000

Certified by .....
Mildred S. Dresselhaus
Institute Professor
Thesis Supervisor

Accepted by .....
Thomas J. Greytak
Professor, Associate Department Head for Education

Resonance Raman Spectroscopy of Single-Walled Carbon Nanotubes

by

Sandra Dawn Marie Brown

Submitted to the Department of Physics
on May 11, 2000, in partial fulfillment of the
requirements for the degree of
Doctor of Philosophy in Physics

Abstract

The unusual one-dimensional properties of phonons in crystalline arrays of carbon nanotubes is presented. The main technique for probing the phonon spectra is Raman spectroscopy and the many unique and unusual features of the Raman spectra of carbon nanotubes are highlighted. Various features of the first-order Raman spectra are emphasized, with regard to their 1D behavior and special characteristics, such as the radial breathing mode, and the tangential G-band ($\sim$1600cm^{-1}) associated with carbon atom displacements on the cylindrical shell of the nanotube (C–C stretching motion of the atoms). The strong coupling between electrons and phonons in this one-dimensional system furthermore gives rise to highly unusual resonance Raman spectra, and unique features in the Stokes and anti-Stokes Raman spectra.

The Raman tangential G-band feature associated with semiconducting nanotubes have a different characteristic lineshape than those associated with metallic carbon nanotubes. The differences in the electronic density of states of metallic nanotubes relative to semiconducting nanotubes leads to differing resonance behaviors, thus resulting in differing lineshapes in the tangential G-band region of the Raman spectrum. A diameter selective resonance process allows resonant enhancement of the Raman tangential G-band for the metallic nanotubes in a narrow range of laser excitation energies for a sample of nanotubes with a narrow distribution of diameters.

The anti-Stokes Raman spectra of single-wall carbon nanotubes (SWNTs) are unique relative to other crystalline systems, especially in exhibiting large asymmetries with regard to their corresponding Stokes spectra. This asymmetry is due to the unique resonant enhancement phenomena arising from their one-dimensional electronic (1D) density of states. The anti-Stokes spectra are therefore selective of specific carbon nanotubes, as previously reported for the Stokes spectra, but the anti-Stokes spectra are selective of *different* single wall nanotubes than for the corresponding Stokes spectra at a given laser excitation energy E_{laser}. The unique behavior of the anti-Stokes spectra for the first-order tangential modes, which allow accurate identification of the range of E_{laser} where metallic nanotubes contribute to the resonant Raman spectra, is discussed. A detailed Breit–Wigner–Fano lineshape analysis of the

tangential G-band features attributable to metallic carbon nanotubes is presented. Only two components are needed to account for the entire G-band, both with predominantly A (A_{1g}) symmetry, and the nanotube curvature causes the differences in their frequencies and gives rise to the Breit–Wigner–Fano coupling.

Analysis of the second-order resonant Raman spectra of single-walled carbon nanotubes using different laser energies in the range 1.58–2.71 eV is presented. Major emphasis is given to the overtones and combination modes associated with the two dominant features of the first-order spectra, the radial breathing mode and the tangential mode. Both of these modes, as well as their second-order counterparts, are associated with resonant enhancement phenomena arising from electron-phonon coupling to the unique one-dimensional density of electronic states for the single-wall carbon nanotubes. Overtones, combination modes, and the behavior of the D band and G' band in the Stokes and anti-Stokes spectra are also discussed briefly. Comparison between the Stokes and anti-Stokes spectra show that the resonance Raman process is stronger for metallic than for semiconducting nanotubes.

The surface-enhanced resonant Raman scattering (SERRS) spectra of single-walled carbon nanotubes (SWNTs) adsorbed on silver and gold metal island films and on colloidal silver cluster substrates were investigated using different laser excitation wavelengths. The observed enhancement in the SERRS signal of the SWNTs results from: (1) an "electromagnetic" SERS enhancement due to resonances between optical fields and the electronic excitations in the metallic nanostructures, (2) a "chemical" SERS enhancement due to the interaction between the SWNTs and the metal surfaces, and (3) a selective resonance Raman effect between the incident and scattered photons and electronic transitions between the 1D van Hove singularities in the electronic density of states of metallic and semiconducting nanotubes. We have observed changes in the relative intensities and shifts in the peak frequencies of several vibrational modes of the SWNTs upon adsorption on a metal surface, which indicate a specific interaction of the nanotubes with the metal surface. Changes in the resonant Raman spectra due to interaction with the silver or gold surfaces are apparent in the second-order Raman bands, especially in the dispersive features, such as the second-order Raman G' band, which upshifts in the SERRS spectra relative to the resonant Raman scattering (RRS) spectra, providing evidence of a significant perturbation of the electronic levels for the adsorbed nanotubes. In addition, the SERRS spectra show an additional enhancement of the Raman signal for specific features in the vibrational spectra of the metallic nanotubes, in contrast to the case for the semiconducting nanotubes for which the normal RRS and SERRS spectral profiles are very similar. These results can be rationalized in terms of a specific charge-transfer enhancement effect for the metallic nanotubes. The surface-enhanced Raman spectroscopy studies show that the coupling, which results in the Breit–Wigner–Fano lineshape of some of the Raman features associated with metallic nanotubes, is to a surface plasmon based electronic continuum.

Thesis Supervisor: Mildred S. Dresselhaus
Title: Institute Professor

Acknowledgments

The first people I have to thank are my parents. During a time of immense political upheaval in Jamaica (the 70's), one of my first childhood memories is of my father stepping outside the house and pleading with gunmen to not massacre the entire family (because we belonged to an opposing political party). My mother crocheted arts and craft to help supplement the family income. They are the ones who taught me resolve against all adversities, the survival instinct, and I am forever grateful to them. I also want to thank my siblings (Lorna, Colleen, Christopher, Marcia and Howell), their spouses and my nephews (Brian, Timothy, Matthew and Samuel) for being such a joyful bunch. We have not always gotten along, but we have always been a solid force together. To my grandmothers (one of whom passed away many years ago), Aunt Ruby, Aunt Maudlin, Aunt Lurline, Uncle, Uncle Jack, Uncle Mikey and family, I say thank you for having provided so much support over the years.

I must thank Drs. Millie and Gene Dresselhaus for giving me the opportunity to work with them. I just showed up one day, and they never asked any questions. They are excellent scientists, and I have learned so much from them, even while I know that I still have a lot more to learn. The present and former members of MGM, a unique, constantly supportive group, will always stay with me. I think Millie sets the tone for the collaborative spirit of the group. Dr. Ibo Matthews had an incredible intuition about physics (which I have come to appreciate), and he has become a life-long friend. Dr. Xiangzhong Sun was very pensive, very focussed (I like to think very Zen), and quite brilliant. Steve Cronin is an extremely versatile and resourceful scientist, and always found a way to make me laugh. Dr. Alessandra Marucci and Dr. Paola Corio were great hang-out companions, always very supportive, and working with them was absolutely wonderful fun. Laura Doughty is such a gentle soul. I know I will miss her lovely voice trailing down the corridor. I will retain fond memories of the many different members of MGM (Dr. Nathan Belk, Marcie Black, Dr. James Chen, Dr. Siegfried Fleischer, Dr. Lyndon Hicks, Dr. Ado Jorio, Dr. Taka Koga, Yuming Lin, Boris Pevzner, Oded Rabin, Hao Xin, Dr. Herb Zeiger and Dr. Zhibo Zhang)

who have come and gone over the years.

I want also want to thank the collaborators and visiting scientists (Dr. Morinobu Endo, Dr. Marcos Pimenta, Dr. Richiiro Saito, Dr. Katrin Kneipp and Dr. Huiming Cheng) who have passed though MGM over the years and willingly provided samples and shared of their expertise with us. I thank the staff of the CMSE Shared Experimental Facilities (Tim McClure and Libby Shaw) and Crystal Growth Facility (Dr. Fang-cheng Chou) for being so helpful and patient over the years. I also thank the members of the George Harrison Spectroscopy Laboratory (Dr. Ramachandra Dasari, Dr. Gene Hanlon and Karen Shafer) for having provided such excellent equipment and for taking such personal interest in the Carbon Nanotubes research project.

I want to thank all the friends I've made during my time at MIT, because they made the place a lot more tolerable. Marta Dark, the quiet force, is much stronger than she gives herself credit for. Without her support and friendship, I don't think I would have survived here. She helped me keep this glass bowl environment in perspective, and without I think I would have gone quietly mad. The current and former minority graduate students in the physics department (Kimani Stancil, Tehani Finch, Grum Teklemariam, Lisa Dyson, Pam Blakeslee, Gillian Reynolds, Vicentica Valdes, Lyndie Williamson, Isaac Chappel, Jermaine Massey, Bill Hoston and Victor Martinez) have a special place in my heart. In a field where people can't see beyond the surface, you all taught me something about not fitting the norm and not being bothered by it. This department managed to shut out some of you (a grave injustice) but you are resourceful, and I know that you will move on to great things. To the population of BGSA (especially Robbin Chapman, Stephanie Burrows, Nicole Love and Tamara Williams) I give my undying gratitude for providing constant affirmation of my identity, and sometimes, a shoulder to cry on. Alison Morgan is a treasure, and she helped humanized science and scientists for me. Elizabeth Koontz, my drinking buddy (just kidding....sort of) has charted this whole thesis course along with me (we are done, girl!!).

There are also people who didn't give up on me after I left Hunter College and slipped into my three year depression. Dr. Greenbaum from Hunter College (my un-

dergraduate research supervisor) was always willing to offer advice and has remained a source of encouragement over the years. Andre white, who makes obscene amounts of money because he works with McKinsey, never let my obvious envy get in the way of our friendship. Erika Chaves and Rich Cowperthwait were sane voices from the outside world reassuring me that it would be ok.

Various people in the MIT Physics department also need to be acknowledged. Peggy Berkovitz (former Department Administrator) gave the Physics department it's heart. Her dedication to the women graduate students went beyond the dinners and various other gatherings (such as the short-lived Physics Women's Knitting Club), but she also provided a willing ear to our troubles. The department will be lost without her. The Women's Group of the physics department (most notably Zhenya Zastavker, Nicole Morgan, Jessica Thomas and Rebecca Christianson) have also been a great source of encouragement. Pat Solakoff (Administrative Assistant) not only saved my tooth (she knows), but also helped strengthen my resolve to stay here during that miserable first semester. The women in the department office (Alicia Duarte, Claudia LaBollita-James and Nancy Savioli) were always very welcoming and cheered me up every time I stopped by.... If that didn't work, then at least they gave me candy and cookies. I also thank the administrative staff (Virginia M. Esau and Christopher Naylor) whom I constantly bugged about conference travel money. I will be forever be grateful to everyone mentioned here.

As to my thoughts on MIT.....

Lasciate ogni speranza voi che entrante

Contents

List of Figures

List of Tables

Chapter 1

Introduction

Carbon nanotubes provide a remarkable model one-dimensional (1D) system of carbon, due to their very high aspect ratios (nanometers in diameter and microns in length). The single-walled nanotubes (SWNTs) used in this study are hollow cylinders with walls only one atom thick, with about 20-50 carbon atoms around the circumference, and capped at the ends. The nanotubes possess properties that both mirror and contrast bulk graphite. In fact, many of their physical and electronic properties were predicted based on the zone-folding technique applied to the graphene sheet, which is a single layer of crystalline graphite. The one-dimensionality of carbon nanotubes, however, causes them to exhibit electronic and vibrational properties that make them unique relative to other sp^2 carbons. They also exhibit the remarkable property that, depending on the nanotube diameter and orientation of the hexagons of the nanotube structure with respect to the nanotube axis, they can be either metallic or semiconducting. The vibrational properties are also remarkable, since the nanotube cylinder can support vibrations that are not found in graphite (such as a breathing mode where all the atoms vibrate radially). The SWNTs also exhibit remarkable Raman spectra which provide a wealth of information about the 1D electronic density of states through a strong resonant coupling between the incident and scattered photons and the electronic transitions between the van Hove singularities in the 1D density of states in the valence and conduction bands of the nanotubes. Raman spectroscopy, in fact, turns out to be a very powerful tool for studying not just the vibrational

properties but also the strong coupling between electrons and phonons in the nanotubes, resulting in highly unusual resonance behavior of the spectra. In this thesis, I will describe how much rich information I have gained from the carbon nanotubes through using resonance Raman spectroscopy as my principal investigative tool.

Chapter 2 briefly reviews the basic structure and notation used to describe single-walled carbon nanotubes (SWNTs), followed by a description of the unique 1D electronic and vibrational characteristics of the carbon nanotubes. Chapter 3 describes the general theory of light scattering under pre-resonant and resonant conditions and the Raman lineshapes (Lorentzian oscillators versus Breit–Wigner–Fano interaction lineshapes) that will be used in the analyses of the spectra. In Chapter 4, I will present first-order Raman spectra in the Stokes spectrum from the three samples of carbon nanotubes (with different diameter distributions) that I used for the study, where comparisons of their resonant Raman response yields valuable information about their 1D and 2D behavior, with particular emphasis given to the high frequency ($\sim$1600cm^{-1}) tangential G-band feature attributed to semiconducting single-walled carbon nanotubes. The results presented in Chapter 4 do not allow any definitive pronouncements about the tangential G-band features attributed to metallic nanotubes, because I was never able to obtain the contributions from metallic nanotubes alone. In taking advantage of an unusual asymmetry between the Stokes and anti-Stokes Raman tangential G-band spectra (presented in Chapter 5) where we are able to collect the Raman spectra from only metallic carbon nanotubes, I will show how we begin to see differences in the strength of the electron-phonon coupling of the metallic nanotubes as compared to the semiconducting ones. The Breit–Wigner–Fano lineshape, which describes a discrete line interacting with a continuum, will prove to best fit the Raman bands from the metallic nanotubes. However, these experiments do not allow a definitive determination to be made of the interaction mechanism, whether it is between the G-band phonon and a multiphonon continuum or an electronic continuum. This study also points out the importance of the (Stokes and anti-Stokes) Raman *scattered* photon in causing completely *different* carbon nanotubes to contribute resonantly to the Raman spectra at a given laser excitation energy. Study

of the second-order Raman spectrum in Chapter 6 will give further evidence for this increased electron-phonon coupling for the metallic nanotubes. The results of surface-enhanced Raman spectroscopy experiments performed will be described in Chapter 7, where I am finally able to identify the source of the continuum as a collective excitation of the free carriers that populate the Fermi level of the metallic nanotubes. Chapter 8 will summarize all of the information I have gained about the carbon nanotubes throughout the resonant Raman studies, and will point out future directions for research study in this field.

Chapter 2

Carbon Nanotubes

2.1 Introduction

This chapter provides an introduction to the structure and electronic and vibrational properties of carbon nanotubes. Many of the properties of single-walled carbon nanotubes were derived from simple zone-folding of the electronic and phonon dispersion relations of 2D graphite [29, 102]. I will first briefly review the electronic properties of graphite, where the dispersion relation can be calculated using the tight-binding method [102]. I will then introduce the notation used to describe the carbon nanotube structure, show how this is related to the graphene sheet, and describe the nanotube electronic and phonon dispersion relations. I will also describe some experiments that have been carried out that confirm the predicted electronic density of states of the carbon nanotubes.

2.1.1 2D Graphite

The 2D electronic energy dispersion relations of a 2D graphene sheet (a single layer of the crystalline graphite lattice) are calculated [102] by solving the eigenvalue problem for a (2×2) Hamiltonian $\mathcal{H}$ and a (2×2) overlap integral matrix $\mathcal{S}$, associated with

the two distinct A and B atom sites in 2D graphite,

$$\mathcal{H} = \begin{pmatrix} \epsilon_{2p} & tf(k) \\ tf(k)^* & \epsilon_{2p} \end{pmatrix} \text{ and } \mathcal{S} = \begin{pmatrix} 1 & sf(k) \\ sf(k)^* & 1 \end{pmatrix}, \tag{2.1}$$

where t and s denote the transfer integral and overlap integral, respectively, ϵ_{2p} is the site energy of the $2p$ atomic orbital and

$$f(k) = e^{ik_x a/\sqrt{3}} + 2e^{-ik_x a/2\sqrt{3}} \cos\frac{k_y a}{2}. \tag{2.2}$$

Here $a = \sqrt{3}a_{\mathrm{C-C}}$ (where $a_{\mathrm{C-C}}$ is the nearest-neighbor C–C distance [1.421 Å in graphite]). Solution of the secular equation

$$\det(\mathcal{H} - E\mathcal{S}) = 0 \tag{2.3}$$

implied by Eq. (2.1) leads to the eigenvalues

$$E^{\pm}_{g2D}(\vec{k}) = \frac{\epsilon_{2p} \pm tw(\vec{k})}{1 \pm sw(\vec{k})} \tag{2.4}$$

for $t < 0$, where the + signs in the numerator and denominator go together, to give the dispersion relation for the bonding π energy band, and likewise for the $-$ sign, which gives the dispersion relation for the antibonding π^* band. If $t > 0$ in Eq. (2.4), then the $\pm$ in the numerator becomes $\mp$. The function $w(\vec{k})$ in Eq. (2.4) is given by

$$\begin{aligned} w(\vec{k}) &= \sqrt{|f(\vec{k})|^2} \\ &= \sqrt{1 + 4\cos\frac{\sqrt{3}k_x a}{2}\cos\frac{k_y a}{2} + 4\cos^2\frac{k_y a}{2}}. \end{aligned} \tag{2.5}$$

Figure 2-1 shows the unit cell and Brillouin zone of the 2D graphene sheet, and in Fig. 2-2 we plot the electronic energy dispersion relations for 2D graphite as a function of the two-dimensional k values in the hexagonal Brillouin zone.

Near the K-point at the corner of the hexagonal Brillouin zone of graphite, $w(\vec{k})$

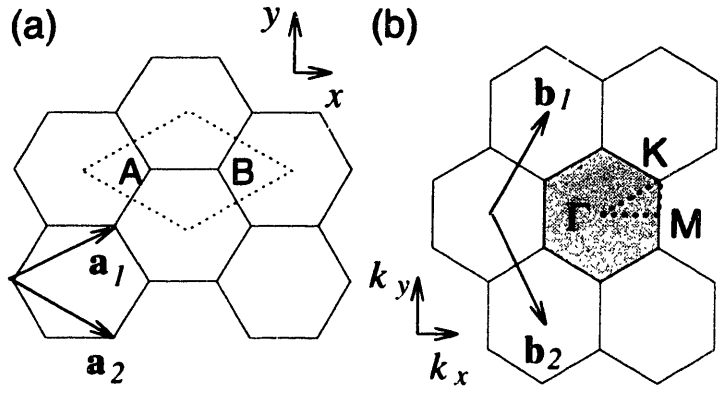

Figure 2-1: (a) The unit cell and (b) Brillouin zone of two-dimensional graphite are shown as the dotted rhombus and the shaded hexagon, respectively. $\mathbf{a}_i$, and $\mathbf{b}_i$, $(i = 1, 2)$ are basis vectors and reciprocal lattice vectors, respectively. Energy dispersion relations are obtained along the perimeter of the dotted triangle connecting the high symmetry points, Γ, K and M.

has a linear dependence on $k \equiv |\vec{k}|$ measured from the K point as

$$w(\vec{k}) = \frac{\sqrt{3}}{2}ka + \ldots, \quad \text{for } ka \ll 1. \tag{2.6}$$

Thus the expansion of Eq. (2.4) for small k yields

$$E^{\pm}_{g2D}(\vec{k}) = \epsilon_{2p} \pm (|t| - s\epsilon_{2p})w(\vec{k}) + \ldots \tag{2.7}$$

so that the antibonding and bonding bands are symmetric near the K point, independent of the value of s. When we adopt $\epsilon_{2p} = 0$ and $s = 0$ for Eq. (2.4) and assume a linear approximation for $w(k)$, then $\gamma_0 = -t$ (where γ_0 is the $\pi - \pi$ overlap energy) and we get the linear dispersion relation for graphite given by McClure [75],

$$E(k) = \pm\frac{\sqrt{3}}{2}\gamma_0 ka = \pm\frac{3}{2}\gamma_0 k a_{C-C}, \tag{2.8}$$

where a_{C-C} is the nearest neighbor carbon-carbon distance. If the physical phenomena under consideration only involve small k vectors, it is convenient to use Eq. (2.8) to calculate the electronic transition energies. The experimental value of γ_0 for 3D graphite is 3.16 eV [30], but the value for carbon nanotubes was only recently estab-

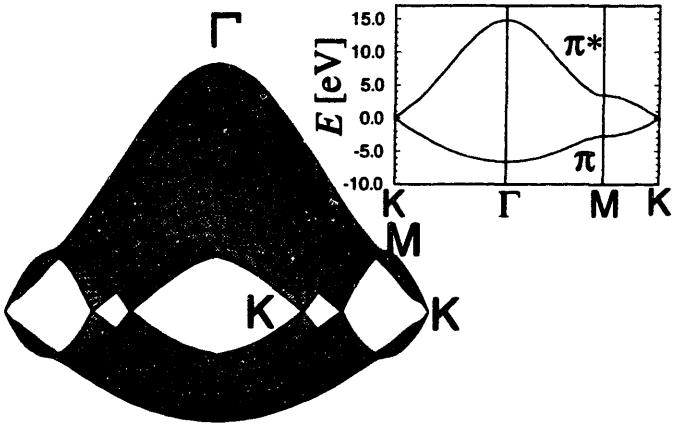

Figure 2-2: The energy dispersion relations for the π and π^* bands in 2D graphite are shown throughout the whole region of the Brillouin zone. The inset shows the energy dispersion along the high symmetry directions of the 2D Brillouin zone [103].

lished to be 2.9±0.2 eV[24], through comparison of the results of various experiments including scanning tunneling microscopy/spectroscopy [124] (shown in Fig. 2-12) and results from the comparison of the resonant Raman spectra of two different diameter distributions of carbon nanotubes (see Chapter 4).

2.1.2 Structure and Notation

A single wall carbon nanotube (SWNT) can be conceptualized as a single graphene sheet, one atom thick, composed of a honeycomb arrangement of carbon atoms, that is rolled up into a seamless cylinder [26]. Figure 2-3 shows how this rectangle of the graphene sheet can be oriented (relative to the hexagons in the honeycomb) to produce the many different types of nanotubes. We first specify the chiral vector ($\mathbf{C}_h$) for the nanotube:

$$\mathbf{C}_h = n\mathbf{a}_1 + m\mathbf{a}_2 \equiv (n, m) \tag{2.9}$$

where the vectors $\mathbf{a}_1$ and $\mathbf{a}_2$ are lattice translation vectors for graphite. The two numbers n and m can take on integer values, and describe the vector $\mathbf{C}_h$ which connects two crystallographically equivalent sites O and A on the two-dimensional (2D) graphene sheet where a carbon atom is located at each vertex of the honeycomb structure [28]. The length of the translation vector $\mathbf{T}$ is determined by traveling away

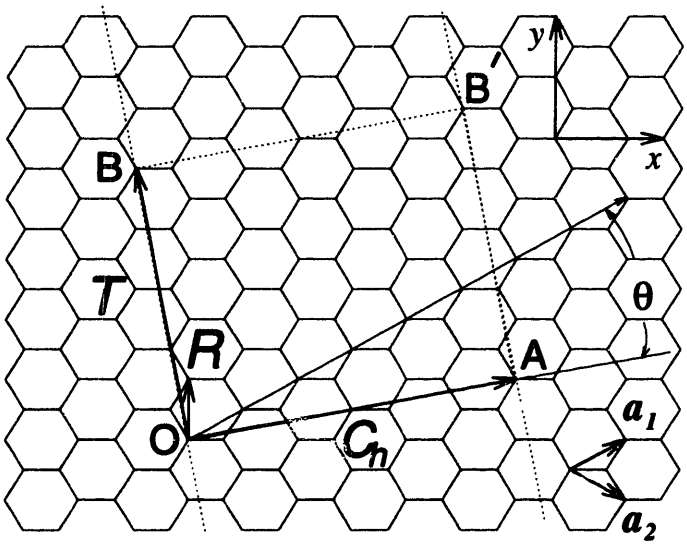

Figure 2-3: The unrolled honeycomb lattice of a nanotube. When we connect sites O and A, and sites B and B', a nanotube can be constructed. $\overrightarrow{OA}$ and $\overrightarrow{OB}$ define the chiral vector $\mathbf{C}_h$ and the translational vector $\mathbf{T}$ of the nanotube, respectively. The rectangle $OAB'B$ defines the unit cell for the nanotube. The figure is constructed for an $(n, m) = (4, 2)$ nanotube.

from point O (at right angles to vector $\mathbf{C}_h$) until you reach an equivalent lattice site to O (point B). A seamless cylinder joint of the nanotube is made by joining the line OB to the parallel line AB' in Fig. 2-3. In terms of the integers (n, m), the nanotube diameter d_t is given by

$$d_t = C_h/\pi = \sqrt{3}a_{\mathrm{C-C}}(m^2 + mn + n^2)^{1/2}/\pi \tag{2.10}$$

where C_h is the length of the chiral vector $\mathbf{C}_h$, and the chiral angle θ is given by

$$\theta = \tan^{-1}[\sqrt{3}m/(m + 2n)]. \tag{2.11}$$

When the angle θ is zero (see Fig. 2-3), then the result is called a zigzag nanotube; and when θ is 30°, then it is called an armchair nanotube. Any angle of θ in between these two extremes gives rise to chiral nanotubes. Figure 2-4 shows the different type of carbon nanotubes. The vector $\mathbf{C}_h$ connects two crystallographically equivalent sites O and A on the two-dimensional (2D) graphene sheet where a carbon atom is

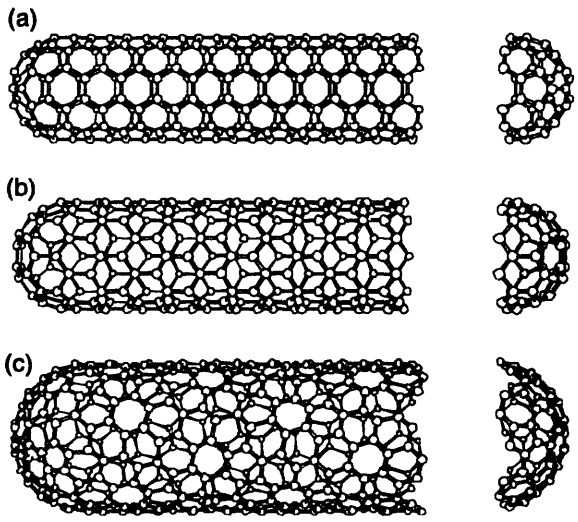

Figure 2-4: Schematic models for single-wall carbon nanotubes. (a) an "armchair" (n, n) nanotube, (b) a "zigzag" $(n, 0)$ nanotube, and (c) a "chiral" (n, m) nanotube $(n \neq m)$ [29].

located at each vertex of the honeycomb structure [28]. Thus, a nanotube can be specified by either its (n, m) indices or equivalently by d_t and θ. Next we define the unit cell $OBB'A$ of the 1D nanotube in terms of the unit cell of the 2D honeycomb lattice defined by the vectors $\mathbf{a}_1$ and $\mathbf{a}_2$ (Fig. 2-3).

In Fig. 2-1 we show (a) the unit cell and (b) the Brillouin zone of two-dimensional graphite as a dotted rhombus and shaded hexagon, respectively, where $\mathbf{a}_1$ and $\mathbf{a}_2$ are basis vectors in real space, and $\mathbf{b}_1$ and $\mathbf{b}_2$ are reciprocal lattice basis vectors. In the x, y coordinates shown in the Fig. 2-1, the real space basis vectors $\mathbf{a}_1$ and $\mathbf{a}_2$ of the hexagonal lattice are expressed as

$$\mathbf{a}_1 = \left(\frac{\sqrt{3}}{2}a, \frac{a}{2}\right), \quad \mathbf{a}_2 = \left(\frac{\sqrt{3}}{2}a, -\frac{a}{2}\right), \tag{2.12}$$

where $a = |\mathbf{a}_1| = |\mathbf{a}_2| = 1.42 \times \sqrt{3} = 2.46\,\text{Å}$ is the lattice constant of two-dimensional graphite. Correspondingly the basis vectors $\mathbf{b}_1$ and $\mathbf{b}_2$ of the reciprocal lattice are given by:

$$\mathbf{b}_1 = \left(\frac{2\pi}{\sqrt{3}a}, \frac{2\pi}{a}\right), \quad \mathbf{b}_2 = \left(\frac{2\pi}{\sqrt{3}a}, -\frac{2\pi}{a}\right) \tag{2.13}$$

corresponding to a lattice constant of $4\pi/\sqrt{3}a$ in reciprocal space. The direction of the basis vectors b_1 and b_2 of the reciprocal hexagonal lattice are rotated by 30° from the basis vectors a_1 and a_2 of the hexagonal lattice in real space, as shown in Fig. 2-1. Here we define the three high symmetry points, Γ, K and M as the center, the corner, and the center of the edge, respectively. The energy dispersion relations are calculated for the triangle ΓMK shown by the dotted lines in Fig. 2-1(b).

To define the unit cell for the 1D nanotube, we define $\overrightarrow{OB}$ in Fig. 2-3 as the shortest repeat distance along the nanotube axis, thereby defining the translation vector $\mathbf{T}$

$$\mathbf{T} = t_1\mathbf{a}_1 + t_2\mathbf{a}_2 \equiv (t_1, t_2) \tag{2.14}$$

where the coefficients t_1 and t_2 are related to (n, m) by

$$\begin{aligned} t_1 &= (2m + n)/d_R \\ t_2 &= -(2n + m)/d_R \end{aligned} \tag{2.15}$$

and d_R is the greatest common divisor of $(2n + m, 2m + n)$ and is given by

$$d_R = \begin{cases} d & \text{if } n - m \text{ is not a multiple of } 3d \\ 3d & \text{if } n - m \text{ is a multiple of } 3d, \end{cases} \tag{2.16}$$

in which d is the greatest common divisor of (n, m). The magnitude of the translation vector $T = |\mathbf{T}|$ is

$$|\mathbf{T}| = \sqrt{3}L/d_R \tag{2.17}$$

where L is the length of the chiral vector $C_h = \pi d_t$ and d_t is the nanotube diameter. The unit cell of the nanotube is defined as the area delineated by the vectors $\mathbf{T}$ and $\mathbf{C}_h$. The number of hexagons, N, contained within the unit cell of a nanotube is determined by the integers (n, m) and is given by

$$N = \frac{2(m^2 + n^2 + nm)}{d_R}. \tag{2.18}$$

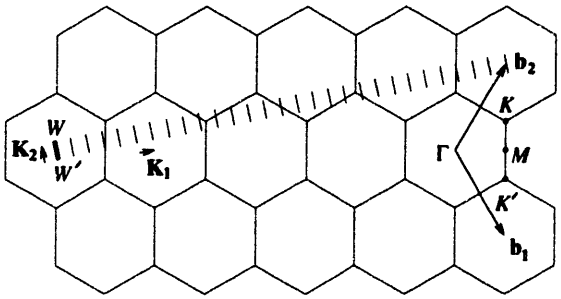

Figure 2-5: The Brillouin zone of a carbon nanotube is represented by the line segment WW' which is parallel to $\mathbf{K}_2$. The vectors $\mathbf{K}_1$ and $\mathbf{K}_2$ are reciprocal lattice vectors corresponding to $\mathbf{C}_h$ and $\mathbf{T}$, respectively. The figure corresponds to $\mathbf{C}_h = (4,2)$, $\mathbf{T} = (4,-5)$, $N = 28$, $\mathbf{K}_1 = (5\mathbf{b}_1 + 4\mathbf{b}_2)/28$, $\mathbf{K}_2 = (4\mathbf{b}_1 - 2\mathbf{b}_2)/28$.

The addition of a single hexagon to the honeycomb structure in Fig. 2-3 corresponds to the addition of two carbon atoms. Assuming a value $a_{C-C} = 0.142\,\text{nm}$ on a carbon nanotube, we obtain $d_t = 1.356\,\text{nm}$ and $N = 20$ for a (10,10) nanotube. Since the nanotube real space unit cell is much larger than that for a 2D graphene sheet, the 1D Brillouin zone (BZ) for the nanotube is much smaller than the BZ for a single 2-atom graphene 2D unit cell. Because the local crystal structure of the nanotube is so close to that of a graphene sheet, and because the Brillouin zone is small, Brillouin zone-folding techniques have been commonly used to obtain approximate electron and phonon dispersion relations for carbon nanotubes with specific symmetry (n,m).

Whereas the lattice vector $\mathbf{T}$, given by Eq. (2.14), and the chiral vector $\mathbf{C}_h$, given by Eq. (2.9) both determine the unit cell of the carbon nanotube in real space, the corresponding vectors in reciprocal space are the reciprocal lattice vectors $\mathbf{K}_2$ along the nanotube axis and $\mathbf{K}_1$ in the circumferential direction (see Fig. 2-5), which gives the discrete k values in the direction of the chiral vector $\mathbf{C}_h$. The vectors $\mathbf{K}_1$ and $\mathbf{K}_2$ are obtained from the relation $\mathbf{R}_i \cdot \mathbf{K}_j = 2\pi\delta_{ij}$, where $\mathbf{R}_i$ and $\mathbf{K}_j$ are, respectively, the lattice vectors in real and reciprocal space, and $\mathbf{K}_1$ and $\mathbf{K}_2$ therefore satisfy the relations

$$\begin{aligned} \mathbf{C}_h \cdot \mathbf{K}_1 &= 2\pi, \qquad & \mathbf{T} \cdot \mathbf{K}_1 &= 0, \\ \mathbf{C}_h \cdot \mathbf{K}_2 &= 0, \qquad & \mathbf{T} \cdot \mathbf{K}_2 &= 2\pi. \end{aligned} \tag{2.19}$$

From Eqs. (2.19) it follows that $\mathbf{K}_1$ and $\mathbf{K}_2$ can be written as:

$$\mathbf{K}_1 = \frac{1}{N}(-t_2\mathbf{b}_1 + t_1\mathbf{b}_2), \quad \mathbf{K}_2 = \frac{1}{N}(m\mathbf{b}_1 - n\mathbf{b}_2), \tag{2.20}$$

where $\mathbf{b}_1$ and $\mathbf{b}_2$ are the reciprocal lattice vectors of a two-dimensional graphene sheet given by Eq. (2.13). The N wave vectors $\mu\mathbf{K}_1$ ($\mu = 0, \cdots, N-1$) give rise to N discrete k vectors in the circumferential direction. For each of the μ discrete values of the circumferential wave vectors, a one-dimensional electronic energy band appears, whereas each μ gives rise to 6 branches in the phonon dispersion relations. Because of the translational symmetry of $\mathbf{T}$, we have continuous wave vectors in the direction of $\mathbf{K}_2$ for a carbon nanotube of infinite length.

Typically, the experimental single wall nanotube (SWNT) samples have a distribution of diameters and chiral angles because of the absence of experimental techniques at present for producing SWNTs with a unique d_t and θ. The carbon nanotube materials used in this study are produced by the pulsed-laser vaporization, and carbon arc discharge methods. The diameter distribution (d_t) of the nanotubes produced in these processes depend on such parameters as the mixture and type of transition metal catalysts used and the oven temperature, and therefore for each sample of nanotube studied, I will specify the catalyst mixture as well as d_t.

The SWNTs appear in a scanning electron microscope (SEM) image as a mat of carbon nanotubes bundles 10–20 nm in diameter and up to 100 μm or more in length (see Fig. 2-6) and containing between 30–500 SWNTs. The nanotubes within a bundle are twisted together, thereby maximizing the bonding interaction between SWNTs within the bundles where the hexagons on adjacent nanotubes tend to be in the same AB registry as in crystalline graphite [39]. The nanotube bundles attract one another and wrap around each other to form ropes [39]. These nanotube ropes are accompanied by varying amounts of amorphous carbon, residual catalyst, and other unwanted material, from which the nanotube ropes must be separated. A number of experimental observations have also been made on a material called "bucky paper", which refers to a flat tangled mat of bundles of carbon nanotubes that are collected

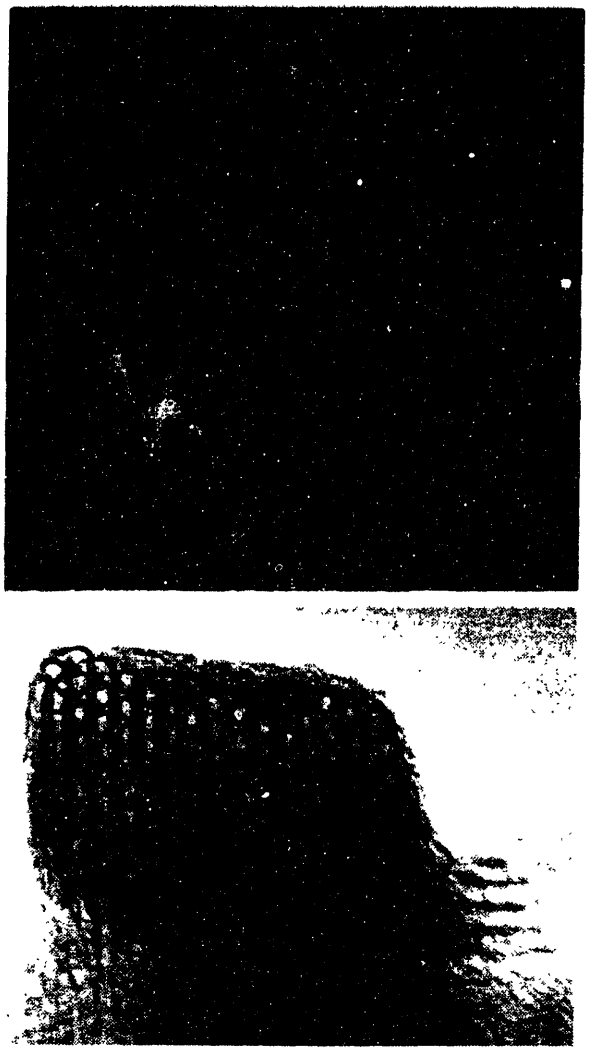

Figure 2-6: (a) Ropes of single-wall carbon nanotubes observed by scanning electron microscopy (SEM). The ropes are 10–20 nm thick and $\sim$100 μm long. (b) At higher magnification, the TEM image shows that each rope contains a bundle of single-wall nanotubes with diameters of $\sim$1.4 nm, arranged in a triangular lattice (with lattice constant 1.7 nm). The lower image is seen when the rope bends through the image plane of the transmission electron microscope (TEM) [118].

on filter paper as a suspension of SWNT bundles is passed through the filter paper.

Under transmission electron microscope (TEM) examination, each nanotube rope is found to consist primarily of bundles of single-wall carbon nanotubes that are mostly aligned along a common axis [see Fig. 2-6(a)]. X-ray diffraction (which views many ropes at once) and transmission electron microscopy (which typically views one or two ropes) show that the diameters of the single-wall nanotubes have a strongly peaked narrow distribution of diameters. Typical nanotube diameters in the ropes are between 0.9–1.8 nm, depending on the catalyst and growth conditions, though smaller diameter nanotubes as small as 0.4 nm have been reported [1]. For the synthesis conditions used in the early work (pulsed-laser vaporization using 1 to 2 atom % of Ni/Co in a furnace at 1200°C), the diameter distribution was strongly peaked at 1.38±0.2 nm, very close to the diameter of an ideal (10,10) nanotube. X-ray diffraction measurements [45, 118] further showed that, within these "ropes", the single-wall nanotubes form a two-dimensional triangular lattice with a lattice constant of 1.7 nm, and an inter-tube separation of 0.315 nm at closest approach within a rope, in good agreement with prior theoretical modeling results [17, 15]. The diameter and chiral angle of individual nanotubes are measured by transmission electron microscopy [40], and by scanning tunneling microscopy [83, 124] techniques.

2.1.3 Electronic Structure

Because of the strong coupling between electrons and phonons in the resonance Raman effect, the remarkable electronic properties of carbon nanotubes play an important role in discussing the unusual Raman spectra of these unique one-dimensional structures. In single wall carbon nanotubes, confinement of the structure in the radial direction is provided by the monolayer thickness of the nanotube in the radial direction. Circumferentially, the periodic boundary condition applies to the enlarged unit cell that is formed in real space. The application of this periodic boundary condition to the graphene electronic states leads to the prediction of a remarkable electronic structure for carbon nanotubes.

The 1D electronic energy band structure for carbon nanotubes [37, 38, 80, 100, 117]

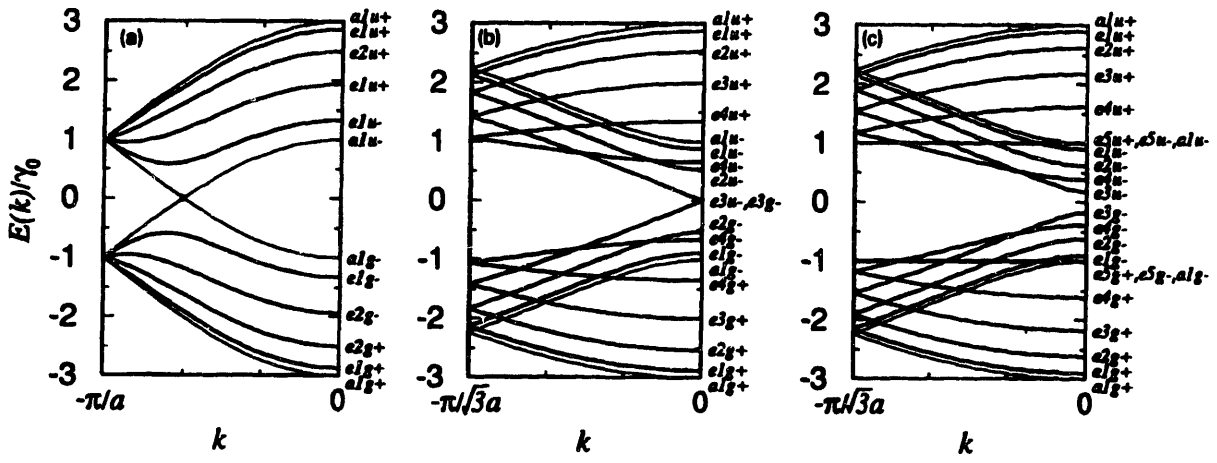

Figure 2-7: One-dimensional energy dispersion relations for (a) armchair (5,5) nanotubes, (b) zigzag (9,0) nanotubes, and (c) zigzag (10,0) nanotubes. The energy bands with a symmetry are non-degenerate, while the e-bands are doubly degenerate at a general wave vector k [104, 105, 106].

is related to the energy band structure calculated for the 2D graphene honeycomb sheet used to form the nanotube. These calculations for the electronic structure of SWNTs [102] show that about 1/3 of the nanotubes are metallic and 2/3 are semiconducting, depending on the nanotube diameter d_t and chiral angle θ. It can be shown that metallic conduction in a (n, m) carbon nanotube is achieved when

$$2n + m = 3q \tag{2.21}$$

where q is an integer. All armchair carbon nanotubes ($\theta = 30°$) are metallic since they always satisfy Eq. (2.21).

Calculated dispersion relations based on these simple zone folding considerations for tight binding energy bands are shown for metallic nanotubes $(n, m) = (5, 5)$ and (9,0) in Figs. 2-7(a) and (b), respectively, and for a semiconducting nanotube $(n, m) = (10, 0)$ in Fig. 2-7(c) [104]. These results are consistent with more detailed calculations of the band structure [70]. The calculated electronic structure can be either metallic or semiconducting depending on the choice of (n, m) as given by Eq. (2.21), although there is no difference in the local chemical bonding between the carbon atoms in the

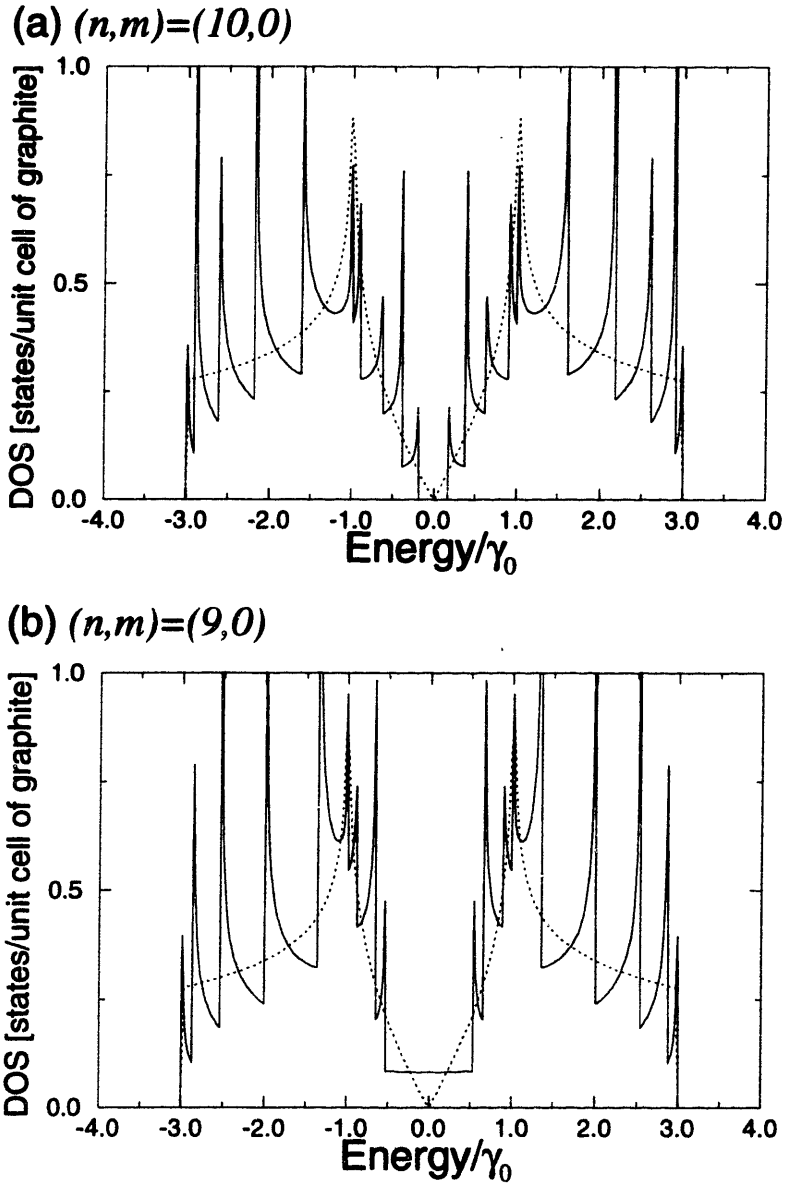

Figure 2-8: Electronic 1D density of states per unit cell of a 2D graphene sheet for two $(n, 0)$ zigzag nanotubes: (a) the $(10, 0)$ nanotube which has semiconducting behavior, (b) the $(9, 0)$ nanotube which has metallic behavior. Also shown in the figure is the density of states for the 2D graphene sheet (dotted line) [101].

nanotubes, and no doping impurities are present [105].

These surprising results and the unique features of the electronic structure of SWNTs can be understood on the basis of the electronic structure of a graphene sheet which is a zero gap semiconductor [86] with bonding and antibonding π bands that are degenerate at the K-point (zone corner) of the hexagonal 2D Brillouin zone [102]. The periodic boundary conditions for the 1D carbon nanotubes of small diameter permit only a few wave vectors to exist in the circumferential direction, and these wave vectors k satisfy the relation $n\lambda = \pi d_t$ where $\lambda = 2\pi/k$ is the de Broglie wavelength. Metallic conduction occurs when one of these allowed wave vectors k passes through the K-point of the 2D Brillouin zone, where the 2D valence and conduction bands are degenerate because of the special symmetry of the 2D graphene lattice [102]. As the nanotube diameter increases, more wave vectors become allowed for the circumferential direction, so that the nanotubes become more two-dimensional and the semiconducting band gap disappears. The band gap for semiconducting carbon nanotubes is proportional to the reciprocal nanotube diameter $1/d_t$. At a nanotube diameter of $d_t \sim 3\,\text{nm}$, the band gap becomes comparable to thermal energies at room temperature, showing that small diameter nanotubes are needed to observe 1D quantum effects.

Of particular importance to the discussion of the resonant Raman spectra is the 1D density of states plots shown in Fig. 2-8 for: (a) a semiconducting (10,0) zigzag carbon nanotube, and (b) a metallic (9,0) zigzag carbon nanotube. The results for the 1D electronic density of states show sharp singularities associated with the $(E - E_0)^{-1/2}$ van Hove singularities about each subband edge at energy E_0 (see Fig. 2-7). The electronic density of states plots in Fig. 2-8 show that the metallic nanotubes have a small, but non-vanishing 1D density of states at the Fermi level (which is at $E = 0$ in Fig. 2-8), and this non-vanishing density of states is independent of energy until the energies of the first subband edges of the valence and conduction bands are reached. In contrast, for a 2D graphene sheet (dashed curve), the 2D density of states is zero at the Fermi level (where also $E = 0$ in Fig. 2-8), and varies linearly with energy, as we move away from the Fermi level. Furthermore, the density of states for the semiconducting

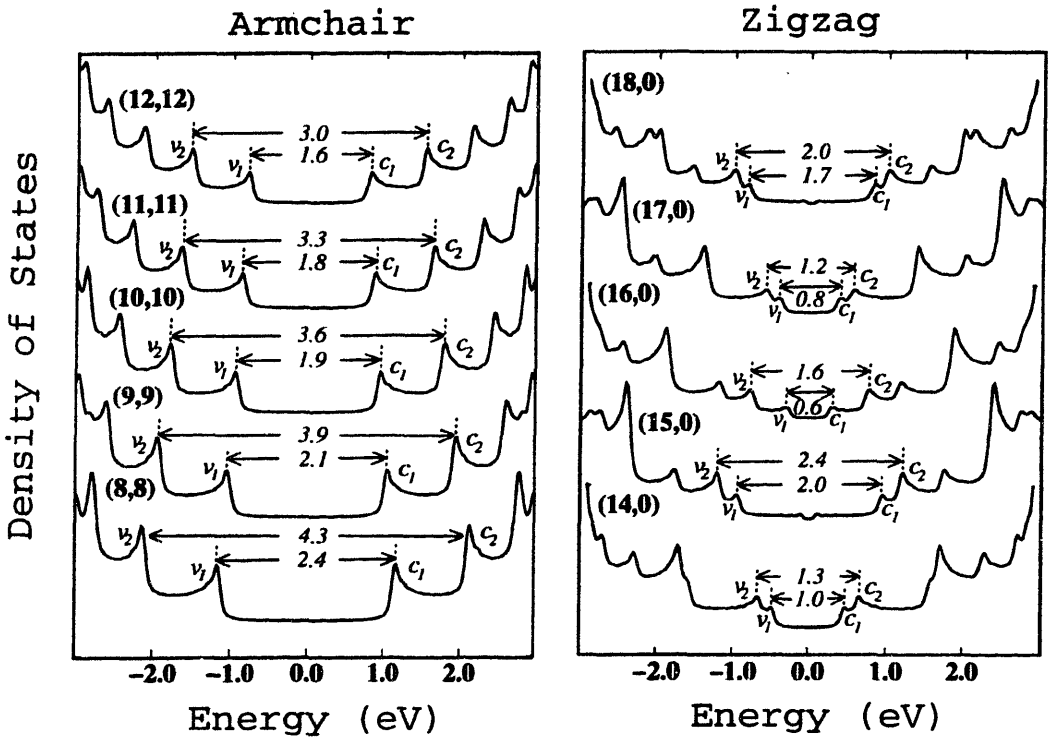

Figure 2-9: Electronic 1D density of states (DOS) calculated with a tight binding model for (8,8), (9,9), (10,10), (11,11), and (12,12) armchair nanotubes and for (14,0), (15,0), (16,0), (17,0), and (18,0) zigzag nanotubes and assuming a nearest neighbor carbon-carbon interaction energy $\gamma_0 = 3.0\,\text{eV}$ [18]. Wavevector conserving optical transitions can occur between mirror image singularities in the 1D density of states, i.e., $v_1 \rightarrow c_1$ and $v_2 \rightarrow c_2$, etc., and these optical transitions are given in the figure in units of eV. These interband transitions are denoted in the text by E_{11}, E_{22}, etc. and are responsible for the resonant Raman effect discussed extensively in this review [18].

1D nanotubes is zero throughout the band gap, as shown in Fig. 2-8(a), and their band gap energy E_g is equal to the energy difference $E_{11}(d_t)$ between the two van Hove singularities in the 1D density of states that span the Fermi level, where it is noted that E_g is proportional to the reciprocal nanotube diameter $E_g \propto 1/d_t$. Because of these singularities in the density of states, high optical absorption is expected when the photon energy matches the energy separation between an occupied peak in the electron density of states and one that is empty. This situation occurs at the band gap for the semiconducting nanotubes, but also at higher energies for transitions from an occupied subband edge state to the corresponding unoccupied subband edge state. Such transitions between subband edge states can occur for both semiconducting and metallic nanotubes. Comparing the density of states curves in Fig. 2-8, we see that the smallest energy separation ($E_{11}(d_t)$) between subband edge states for the semiconducting nanotube (10,0) is much smaller than the corresponding separation between subband edges for the metallic (9,0) nanotube.

The general characteristics that are predicted for the 1D electronic density of states of carbon nanotubes have recently been confirmed by low temperature STM/STS (scanning tunneling microscopy/spectroscopy) studies carried out on isolated single-wall carbon nanotubes [25, 83, 124] as discussed below. Insight into the variation of the electronic density of states (based on more detailed calculations of the electronic structure than the tight binding approximation) with nanotube diameter d_t is provided by Fig. 2-9 where the density of states is presented for (8,8), (9,9), (10,10), (11,11), and (12,12) armchair nanotubes and for (14,0), (15,0), (16,0), (17,0), and (18,0) zigzag nanotubes [95]. Referring to Fig. 2-9, we see that the lowest energy transition for the armchair nanotube, denoted by $E_{11}^M(d_t)$, varies monotonically from 2.4 eV for the (8,8) nanotube to 1.6 eV for the (12,12) armchair nanotube.

The interpretation of the interband transitions between van Hove singularities for zigzag nanotubes and chiral nanotubes can be understood by plotting the energies for the transitions between the van Hove singularities in the valence and conduction bands $E_{ii}(d_t)$ of all possible (n, m) nanotubes, including not only armchair and zigzag nanotubes, as shown in Fig. 2-9, but also all chiral nanotubes. Such a plot of $E_{ii}(d_t)$

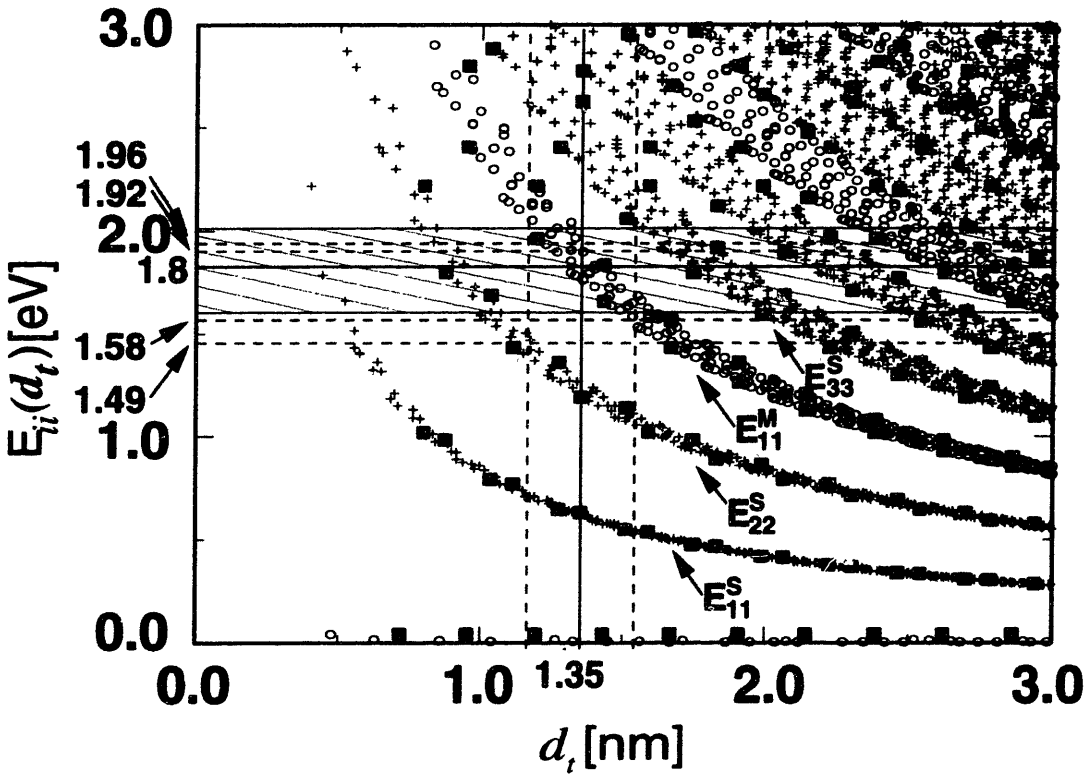

Figure 2-10: Calculation [24, 52, 99] for $\gamma_0 = 2.9\,\text{eV}$ of the energy separations $E_{ii}(d_t)$ for all (n, m) values vs nanotube diameter in the range $0.7 < d_t < 3.0\,\text{nm}$. Semiconducting and metallic nanotubes are indicated by crosses and open circles, respectively, and the four lowest energy transitions are labelled by $E^S_{11}(d_t)$, $E^S_{22}(d_t)$, $E^M_{11}(d_t)$, and $E^S_{33}(d_t)$, where S and M, respectively, refer to semiconducting and metallic nanotubes. The filled squares denote zigzag tubes. The vertical lines denote $d_t = 1.49 \pm 0.20\,\text{nm}$ for a particular single wall carbon nanotube sample. The cross-hatch pattern denotes the range in E_{laser} where metallic nanotubes are expected to contribute resonantly to both the Stokes and anti-Stokes spectra for the indicated diameter distribution.

vs d_t is shown in Fig. 2-10. In this plot, the nearest neighbor carbon-carbon transfer energy γ_0 was taken to be 2.9 eV which provides a good fit to a variety of experiments, including our resonance Raman scattering, optical absorption and scanning tunneling spectroscopy studies [24]. Figure 2-10 is used extensively to interpret resonance Raman spectra in carbon nanotubes, and will re-appear several times in this thesis with different energy windows and diameter distributions shaded, in order to demonstrate its incredible utility. The two lowest energy transitions $E_{11}^S(d_t)$ and $E_{22}^S(d_t)$ are for semiconducting nanotubes, while the next higher energy transition is $E_{11}^M(d_t)$ for metallic nanotubes, followed by $E_{33}^S(d_t)$, as indicated in the figure [52, 103]. The bounds on $E_{ii}(d_t)$ at constant d_t and i are delineated by zigzag nanotubes and are due to trigonal warping effects [103], arising from the non-circular constant energy surfaces that develop with increasing wave vector away from the K-point in the Brillouin zone. This trigonal warping effect is most important for zigzag nanotubes (see Fig. 2-11) and least important for armchair tubes, for which a simple analytical expression for $E_{11}^M(d_t)$ can be written as

$$E_{11}^M(d_t) = 6a_{C-C}\gamma_0/d_t \tag{2.22}$$

where a_{C-C} is the nearest neighbor carbon-carbon distance. It should be mentioned that Eq. (2.22) is only valid for chiral and zigzag nanotubes in the limit of large d_t. For example, the (15,0) zigzag nanotube with diameter $d_t = 1.17$ nm has a lower and upper bound for $E_{11}^M(d_t) = 2.0$ and 2.4 eV, as shown in Fig. 2-9.

Since measurements of dI/dV in the STS (scanning tunneling spectroscopy) mode of a scanning tunneling microscope yield a signal (shown in Fig. 2-12) which is proportional to the 1D density of states, this has become a powerful tool for studying the electronic structure of both metallic and semiconducting single wall carbon nanotubes [83, 124]. The top four traces in Fig. 2-12 show that the bandgap is $E_{11}^S(d_t) \simeq 0.6$ eV for the indicated semiconducting nanotubes, while the lower 3 traces show energy separations of $E_{11}^M(d_t) \simeq 1.8$ eV for metallic nanotubes. The combined STM/STS studies [111, 124] are consistent with: (1) about 2/3 of the nanotubes being semi-

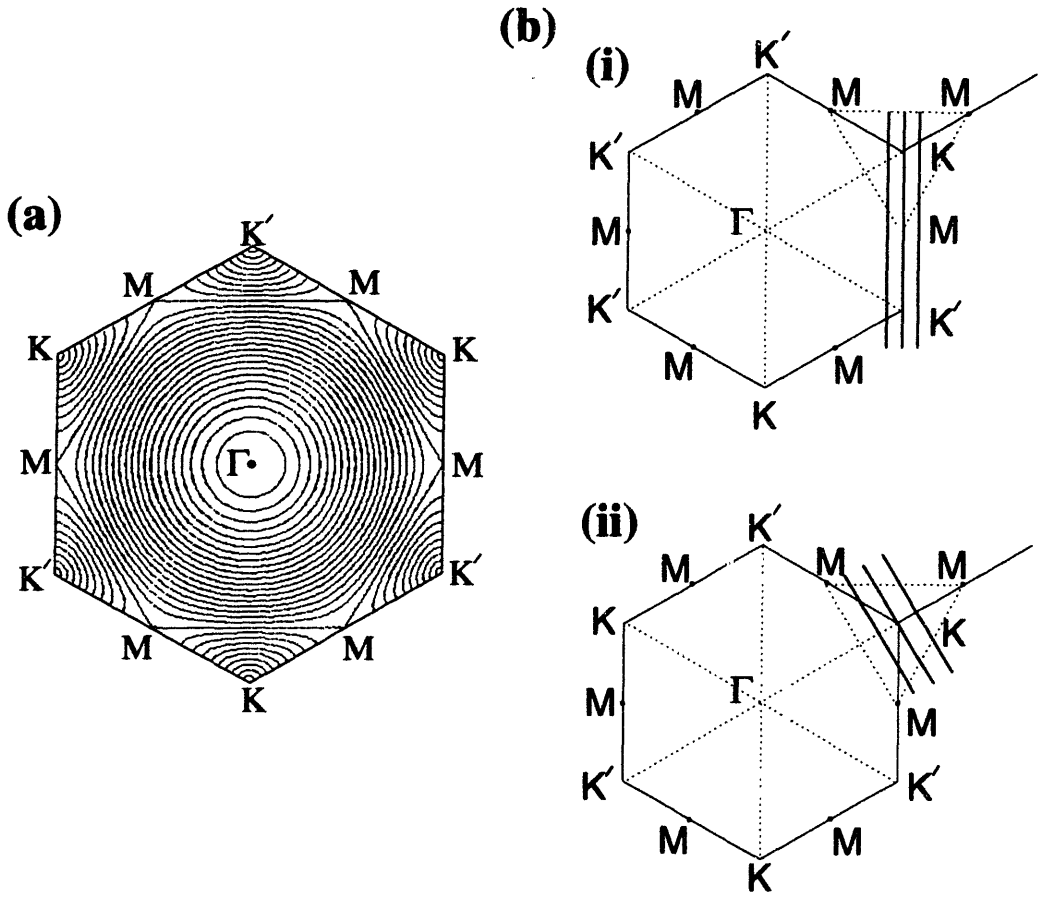

Figure 2-11: (a) The contour plot of 2D energy of graphite. The equi-energy contours are circles near K and near the center of the Brillouin zone, but near the zone boundary the contours are straight lines which connect the nearest M points. (b) The dependence of the trigonal warping effect of the van Hove singularities on the nanotube chirality. The three bold lines near the K point are possible k vectors in the hexagonal Brillouin zone of graphite for metallic (i) armchair and (ii) zigzag carbon nanotubes. All chiral nanotubes with chiral angles $|\theta| \leq \pi/6$ have lines for their k vectors with the directions making a chiral angle θ measured from the bold lines for the zigzag nanotubes. The minimum energy along the neighboring two lines gives the energy positions of the van Hove singularities.

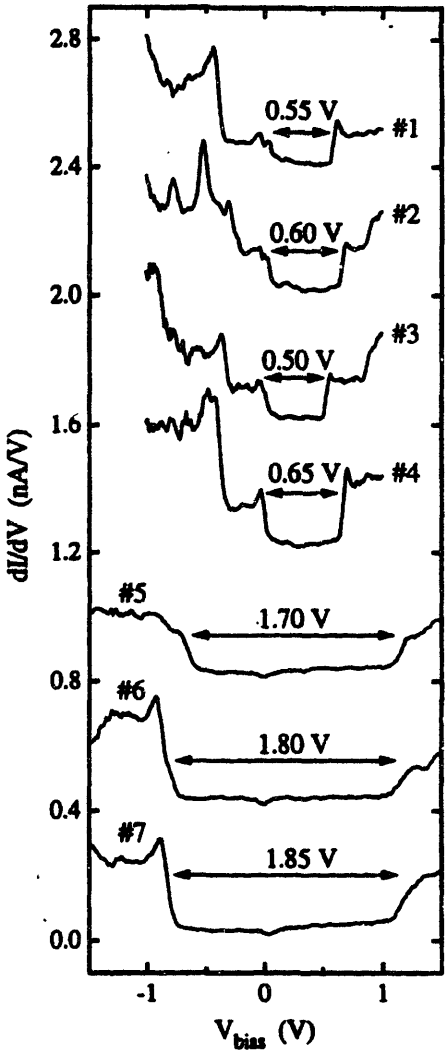

Figure 2-12: Derivative of the current-voltage (dI/dV) curves obtained by scanning tunneling spectroscopy on various isolated single wall carbon nanotubes with diameters near 1.4 nm. Nanotubes #1–4 are semiconducting and #5–7 are metallic [124].

conducting, and 1/3 being metallic; (2) the density of states exhibiting van Hove singularities, characteristic of the expectations for 1D systems; (3) energy gaps for the semiconducting nanotubes that are proportional to $1/d_t$. Using the approximate relation $E_g \simeq 2\gamma_0 a_{C-C}/d_t$ for the band gap of semiconducting single wall nanotubes, the nearest neighbor overlap energy γ_0 (or the transfer integral of a tight binding model) can be found. The STS experiments confirm that the density of electronic states near the Fermi level is zero for semiconducting nanotubes, and non-zero for metallic nanotubes [124]. These electronic density of states curves in Fig. 2-8 and the plot of interband transition energies in Fig. 2-10 are also important for explaining the resonance Raman experiments on carbon nanotubes, discussed in subsequent chapters in this thesis.

2.2 Phonon Modes

The phonon dispersion relations in a carbon nanotube can be obtained from those of the 2D graphene sheet (an isolated graphene sheet) by using the same zone folding approach [42, 97, 107] as was used to find the 1D electronic dispersion relations [41, 102]. Zone folding and symmetry-based force constant models were used by some authors [14, 22, 42, 107], tight binding calculations by other authors [53, 77, 125], and some *ab initio* calculations [61, 110] were also reported. Because of the very weak interplanar interactions, the phonon dispersion relations for graphite in the basal plane (see Fig. 2-13) provide a good first approximation for the 2D phonon dispersion relations of an isolated graphite plane. The calculated phonon dispersion curves of Fig. 2-13 were fit to the experimental points obtained by electron energy loss spectroscopy, inelastic neutron scattering, velocity of sound and other techniques [2, 42, 84]. The inclusion of force constants taking into account fourth-neighbor interaction terms (see Table 2.1) have been sufficient for reproducing the experimental data in Fig. 2-13.

The three phonon dispersion curves (or branches), which originate from the Γ point of the Brillouin zone with $\omega = 0$ (see Fig. 2-13), correspond to acoustic modes:

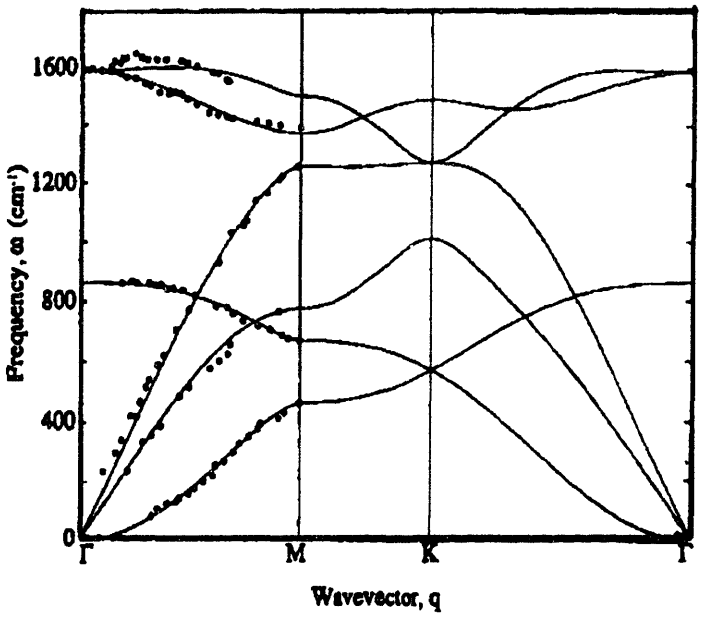

Figure 2-13: The phonon dispersion relations for graphite plotted along high-symmetry in-plane directions. Experimental points from neutron scattering and electron energy loss spectra were used to obtain values for the force constants (see Table 2.1) and to determine the phonon dispersion relations throughout the Brillouin zone [42].

Table 2.1: Force constant parameters for 2D graphite in units of 10^4dyn/cm [42]. Here the subscripts r, ti, and to refer to radial (bond stretching), transverse in-plane and transverse out-of-plane (bond bending) force constants, respectively (see Figs. 2-13).

Radial		Tangential			
$\phi_r^{(1)} =$	36.50	$\phi_{ti}^{(1)} =$	24.50	$\phi_{to}^{(1)} =$	9.82
$\phi_r^{(2)} =$	8.80	$\phi_{ti}^{(2)} =$	−3.23	$\phi_{to}^{(2)} =$	−0.40
$\phi_r^{(3)} =$	3.00	$\phi_{ti}^{(3)} =$	−5.25	$\phi_{to}^{(3)} =$	0.15
$\phi_r^{(4)} =$	−1.92	$\phi_{ti}^{(4)} =$	2.29	$\phi_{to}^{(4)} =$	−0.58

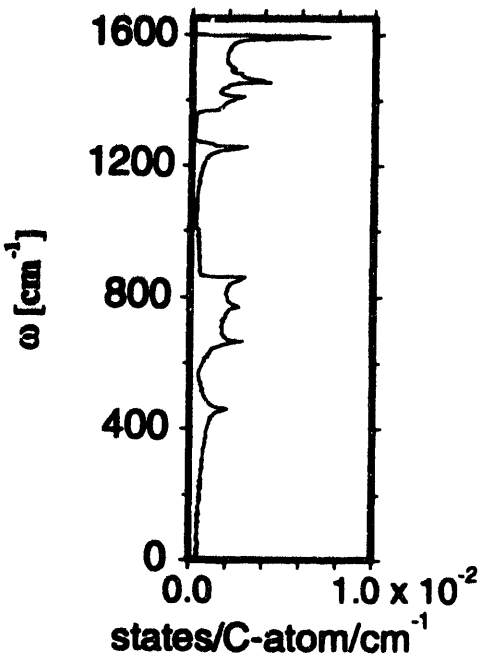

Figure 2-14: The phonon density of states vs phonon energy for a 2D graphene sheet in units of states/C-atom/cm^{-1} $\times$ 10^{-2} [42].

an out-of-plane mode, an in-plane tangential (bond-bending) mode, and an in-plane radial (bond-stretching) mode, listed in order of increasing energy, respectively. The remaining three branches correspond to optical modes: one non-degenerate out-of-plane mode and two in-plane modes that remain degenerate as we move away from $k = 0$.

It is noted that the out-of-plane (transverse) *acoustic* branch for a graphene sheet shows a special k^2 energy dispersion relation around the Γ point, while the other two in-plane acoustic branches show a linear k dependence, as is normally seen for acoustic modes. The *optical* out-of-plane transverse branch (at $\omega \sim 865\,\text{cm}^{-1}$ at the Γ point) also shows a k^2 dependence. Because of this special k^2 dependence of $\omega(k)$ for the out-of-plane acoustic branch near the Γ point, there is neither a phase velocity nor a group velocity for the z component for these acoustic vibrations.

At low frequencies the in-plane acoustic branches for a graphene sheet give rise to a density of states $g(\omega)$ linear in ω, while the out-of-plane k^2 acoustic branch gives rise to a small constant contribution (independent of ω) to the density of states, which is

significant up to $\sim$400 cm^{-1} as shown in Figs. 2-13 and 2-14.

2.2.1 Phonon dispersion relations for nanotubes

As a first approximation, the phonon dispersion relations for an isolated single-wall carbon nanotube are determined by zone folding the phonon dispersion curves $\omega_{2D}^{m}(k)$ of a two-dimensional graphene layer (see Fig. 2-3), where $m = 1, \ldots, 6$ labels the 3 acoustic and 3 optic modes and k is a vector in the layer plane. Since there are $2N$ carbon atoms in this unit cell [see Eq. (2.18)], we will have N pairs of bonding π and anti-bonding π^* electronic energy bands. Similarly the phonon dispersion relations will consist of $6N$ branches resulting from a vector displacement of each carbon atom in the nanotube unit cell.

The phonon dispersion relations of a carbon nanotube depend on the indices (n, m) or equivalently on the diameter and chiral angle of the carbon nanotube, d_t and θ, since the phonon wave vector in the circumferential direction becomes discrete and is described by each of the $\mathbf{K}_1$ vectors [see Eq. (2.20)], in accordance with the periodic boundary conditions of the chiral vector $\mathbf{C}_h$.

In the context of zone folding, the one-dimensional phonon energy dispersion relations for $\omega_{1D}^{m\mu}(k)$ for SWNTs are related to the $\omega_{2D}^{m}(\mathbf{k})$ by:

$$\omega_{1D}^{m\mu}(k) = \omega_{2D}^{m}(k\,\frac{\mathbf{K}_2}{|\mathbf{K}_2|} + \mu\,\mathbf{K}_1)\;, \quad \left(\begin{array}{l} m = 1, \cdots, 6, \\ \mu = 0, \cdots, N-1, \end{array} \text{ and } \; -\frac{\pi}{T} < k \leq \frac{\pi}{T} \right), \quad (2.23)$$

where k is a one-dimensional wave vector, $\mathbf{K}_2$ is the reciprocal lattice vector along the nanotube axis [see Eq. (2.20)], $\mathbf{K}_1$ is the reciprocal lattice vector in the circumferential direction [see Eq. (2.20)] and T is the magnitude of the one-dimensional translation vector $\mathbf{T}$ given in Eq. (2.17).

The zone-folding procedure yields the appropriate one-dimensional $\omega_{1D}^{m\mu}(k)$ for almost all the phonon branches of a carbon nanotube. An example of the phonon branches for an isolated SWNT is shown in Fig. 2-15 for a (10,10) nanotube. In this figure, T denotes the magnitude of the basis vector along the nanotube axis

[see Eq. (2.17)]. For the $2N = 40$ carbon atoms per circumferential strip for the (10,10) nanotube, there are 120 vibrational degrees of freedom, but because of mode degeneracies there are only 66 distinct phonon branches, of which 12 modes are non-degenerate and 54 are doubly degenerate.

In Fig. 2-15(b), we show the corresponding phonon density of states for the (10,10) nanotube in units of states per C atom per cm^{-1}. The phonon density of states for the (10,10) nanotube is close to that for 2D graphite, since the phonon dispersion relations are, in principle, given by the zone-folding of those for 2D graphite. The differences in the nanotube phonon density of states relative to that for 2D graphite pertain to the one-dimensional van Hove singularities for the optical phonon subbands and to the 4 acoustic modes of the nanotubes and their special properties at low ω discussed below.

However, zone-folding of the graphene phonon branches does not always give the correct dispersion relation for a carbon nanotube [42, 102], especially in the low frequency region, and some additional physical concepts must be introduced. There are several mode displacements that are possible in the carbon nanotubes which have no equivalent in graphite. The radial breathing motion ($\omega^0_{\rm RBM}$) of the carbon atoms of the nanotube is an example, where the superscript denotes the mode frequency for an isolated SWNT, leaving $\omega_{\rm RBM}$ to denote the mode frequency in the presence of inter-tube interactions which occur in SWNTs found in nanotube bundles, corresponding to samples used in this thesis.

The effect of the nanotube curvature on the in-plane and out-of-plane radial and tangential force constants has been considered by various authors [24, 64, 102, 110], showing these corrections to be relatively minor, but not negligible for the smallest diameter nanotubes. In rolling the graphene sheet (sp^2 bonding) to form the carbon nanotubes, you need to introduce some amount of sp^3 bonding to create the curvature. This lowers the force constant circumferentially (longer C–C bond), as compared to along the nanotube axis. This effect has *great* importance in the analysis of the peak positions of the Raman bands for the carbon nanotubes, and will be *constantly* referred to throughout the thesis. Since the curvature is not expected to change the

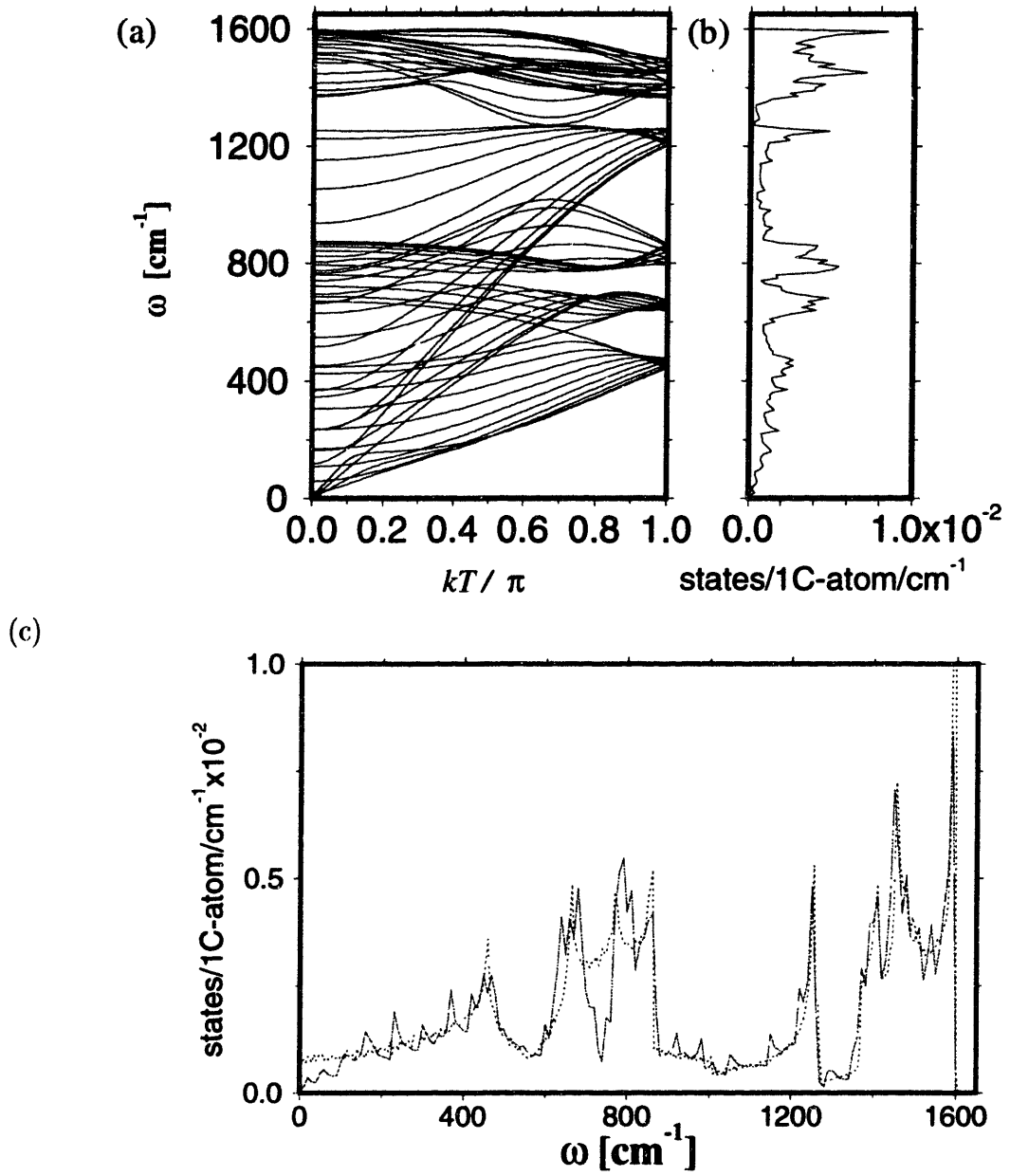

Figure 2-15: (a) The calculated phonon dispersion relations of an armchair carbon nanotube with $\mathbf{C}_h = (10, 10)$. The number of degrees of freedom is 120 and the number of distinct phonon branches is 66. (b) The corresponding phonon density of states for a (10,10) nanotube [102]. (c) A comparison between the phonon density of states $g_{1D}(\omega)$ for a (10,10) nanotube shown as the solid curve and $g_{2D}(\omega)$ for a graphene sheet shown by the points [99].

Table 2.2: Number and symmetries of Raman-active modes for different types of carbon nanotubes.

Nanotube structure	Point group	Raman-active modes	IR-active modes
armchair (n,n) n even	D_{nh}	$4A_{1g} + 4E_{1g} + 8E_{2g}$	$A_{2u} + 7E_{1u}$
armchair (n,n) n odd	D_{nd}	$3A_{1g} + 6E_{1g} + 6E_{2g}$	$2A_{2u} + 5E_{1u}$
zigzag $(n,0)$ n even	D_{nh}	$3A_{1g} + 6E_{1g} + 6E_{2g}$	$2A_{2u} + 5E_{1u}$
zigzag $(n,0)$ n odd	D_{nd}	$3A_{1g} + 6E_{1g} + 6E_{2g}$	$2A_{2u} + 5E_{1u}$
chiral (n,m) $n \neq m \neq 0$	C_N	$4A + 5E_1 + 6E_2$	$4A + 5E_1$

form of $\omega(k)$ for the four acoustic branches very much, no major effect of curvature on the 1D density of phonon states $g_{1D}(\omega)$ is expected.

Interactions between adjacent SWNTs in a nanotube bundle are expected to give rise to a dispersion relation with a finite frequency at $k = 0$ and a k^2 dependence for the twist mode [8]. The contribution of such an inter-tube interaction term would result in a feature with a van Hove-type singularity in the phonon density of states such as is introduced by a phonon subband.

2.2.2 Raman-active modes of carbon nanotubes

Among the $6N$ calculated phonon dispersion relations for carbon nanotubes whose unit cell contains $2N$ carbon atoms, only a few modes are Raman or infrared (IR) active, as specified by the symmetry of the phonon modes. Since only k vectors very close to $k = 0$ are coupled to the incident light because of the energy-momentum conservation requirements for the photons and phonons, we need only consider the symmetry of the nanotube zone-center vibrations at the Γ point ($k = 0$). Point group theory of the unit cell, predicts the number of Raman-active modes and IR-active modes and their symmetry types [102].

The numbers of the Raman-active (A_{1g}, E_{1g}, E_{2g} symmetries) and IR-active (A_{2u}, E_{1u} symmetries) modes for the nanotubes can be predicted by group theory, once the lattice structure and its symmetry are specified. We list the number and symmetries of the Raman-active modes for different types of carbon nanotubes in Table 2.2.

More specifically, we give here the number of modes with their corresponding

symmetry types for all types of nanotubes. For armchair nanotubes (with even $n = 2j$ having D_{nh} symmetry) we write:

$$\begin{aligned}\Gamma_{2j}^{\text{vib}} = \; & 4A_{1g} + 2A_{1u} + 4A_{2g} + 2A_{2u} + 2B_{1g} \\ & +4B_{1u} + 2B_{2g} + 4B_{2u} + 4E_{1g} + 8E_{1u} + 8E_{2g} \\ & +4E_{2u} + \cdots + 4E_{(j-1)g} + 8E_{(j-1)u}.\end{aligned} \tag{2.24}$$

In Eq. (2.24), we assume that j is even. If j is odd [such as for $(n, m) = (6, 6)$], the 4 and 8 are interchanged in the last two terms in Eq. (2.24). For zigzag nanotubes (with even $n = 2j$ having D_{nh} symmetry) we write:

$$\begin{aligned}\Gamma_{2j}^{\text{vib}} = \; & 3A_{1g} + 3A_{1u} + 3A_{2g} + 3A_{2u} \\ & +3B_{1g} + 3B_{1u} + 3B_{2g} + 3B_{2u} \\ & +6E_{1g} + 6E_{1u} + 6E_{2g} + 6E_{2u} \\ & + \cdots + 6E_{(j-1)g} + 6E_{(j-1)u}.\end{aligned} \tag{2.25}$$

For armchair and zigzag nanotubes (with odd $n = 2j + 1$ having D_{nd} symmetry) we write:

$$\begin{aligned}\Gamma_{2j+1}^{\text{vib}} = \; & 3A_{1g} + 3A_{1u} + 3A_{2g} + 3A_{2u} \\ & +6E_{1g} + 6E_{1u} + 6E_{2g} + 6E_{2u} \\ & + \cdots + 6E_{jg} + 6E_{ju}.\end{aligned} \tag{2.26}$$

And finally for chiral nanotubes we write:

$$\Gamma_{N}^{\text{vib}} = 6A + 6B + 6E_1 + 6E_2 + \cdots + 6E_{N/2-1}. \tag{2.27}$$

Using the information in Eqs. (2.24–2.27), we obtain the information summarized in Table 2.2 for the number and symmetry type of the Raman and IR active modes for achiral or symmorphic (i.e., armchair and zigzag) and chiral or non-symmorphic nan-

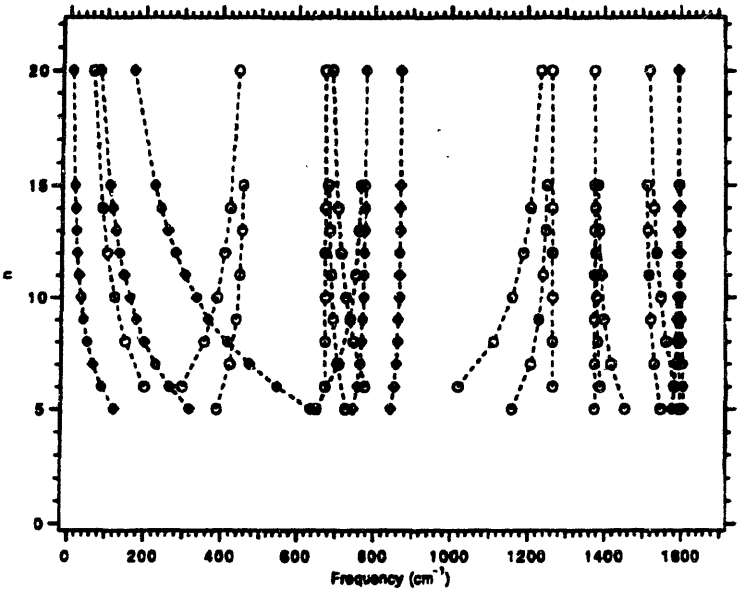

Figure 2-16: The armchair index n vs mode frequency for the Raman-active modes of single-wall armchair (n, n) carbon nanotubes [95]. The nanotube diameter can be found from n using Eq. (2.10).

otubes. Among the achiral nanotubes, only armchair nanotubes with even number indexes $(2j, 2j)$ have a different numbers of Raman and IR modes from the others, such as armchair nanotubes with odd number indexes $(2j + 1, 2j + 1)$ or zigzag nanotubes $(n, 0)$. From Table 2.2 we deduce the *remarkable* Raman and infrared selection rules for SWNTs, that the numbers of Raman and infrared-active modes do not depend on the nanotube diameter and chirality, though the total number of finite frequency phonon modes $(6N - 4)$ is very different for different chiralities and diameters. Group theory selection rules indicate that there are only 15 or 16 Raman-active modes and 6 to 9 IR-active modes for a single-wall carbon nanotube, despite the large number of vibrational modes. Even though group theory may indicate that a particular mode is Raman-active, this mode may nevertheless only have a small Raman cross section. In fact, we have only six or seven intense Raman-active modes for any nanotube chirality.

Since the number of Raman-active and infrared-active modes for a given symmetry category is independent of nanotube diameter, the dependence of a particular

vibrational mode on nanotube diameter can be investigated. Several of the mode frequencies and their Raman cross sections are found to be highly sensitive to the nanotube diameter, while others are not. Figure 2-16 shows the dependence of the frequency of the Raman-active modes on the nanotube diameter for armchair nanotubes, expressed in terms of their (n, n) indices [35]. Here it is seen that the A_{1g} mode, which occurs at about $165\,\mathrm{cm}^{-1}$ for an isolated (10,10) nanotube, is strongly dependent on nanotube diameter, while the modes near $1580\,\mathrm{cm}^{-1}$ are not. A diagram similar to Fig. 2-16 can be constructed for the infrared-active modes for the armchair nanotubes, and also for Raman and infrared-active modes for zigzag and chiral nanotubes [26, 35]. Another factor which simplifies the Raman spectra for SWNTs is the low intensity of many of the Raman-active modes in Fig. 2-16.

The normal mode displacements for the seven Raman modes for a (10,10) nanotube which have a relatively large Raman intensity are shown in Fig. 2-17. The honeycomb lattice shown in Fig. 2-3 can be described in terms of two sublattices consisting A and B atoms. In the higher frequency Raman-active A_{1g} mode ($1587\,\mathrm{cm}^{-1}$ in Fig. 2-17), the A and B atom moves in opposite directions (out-of-phase) in the unit cell, while in the lower frequency Raman-active A_{1g} mode ($165\,\mathrm{cm}^{-1}$ in Fig. 2-17), the A and B atoms move in the same direction (in-phase). It is clear from Fig. 2-17(e) to (g), that the higher-frequency modes are out-of-phase between nearest neighbor carbon atoms, while the lower-frequency modes of Fig. 2-17(a) to (d) show in-phase motion. The out-of-phase motions observed in Fig. 2-17(e) to (g) are similar to the motion of the Raman-active E_{2g} mode of graphite at $1582\,\mathrm{cm}^{-1}$, which corresponds to C=C bond stretching motions for one of the three nearest neighbor bonds in the unit cell.

The basic motions of the atomic displacements of the normal modes shown in Fig. 2-17 are independent of the chirality of the nanotube [102]. The normal mode displacements illustrated in Fig. 2-17 show that the A_{1g}, E_{1g} and E_{2g} modes have zero, two, and four nodes around the nanotube z-axis, respectively [see Fig. 2-17(e), (f), and (g) for out-of-phase motion, and (a), (b), and (c) for in-phase motion]. According to group theory analysis, six peaks can be present in the high frequency region (G band)

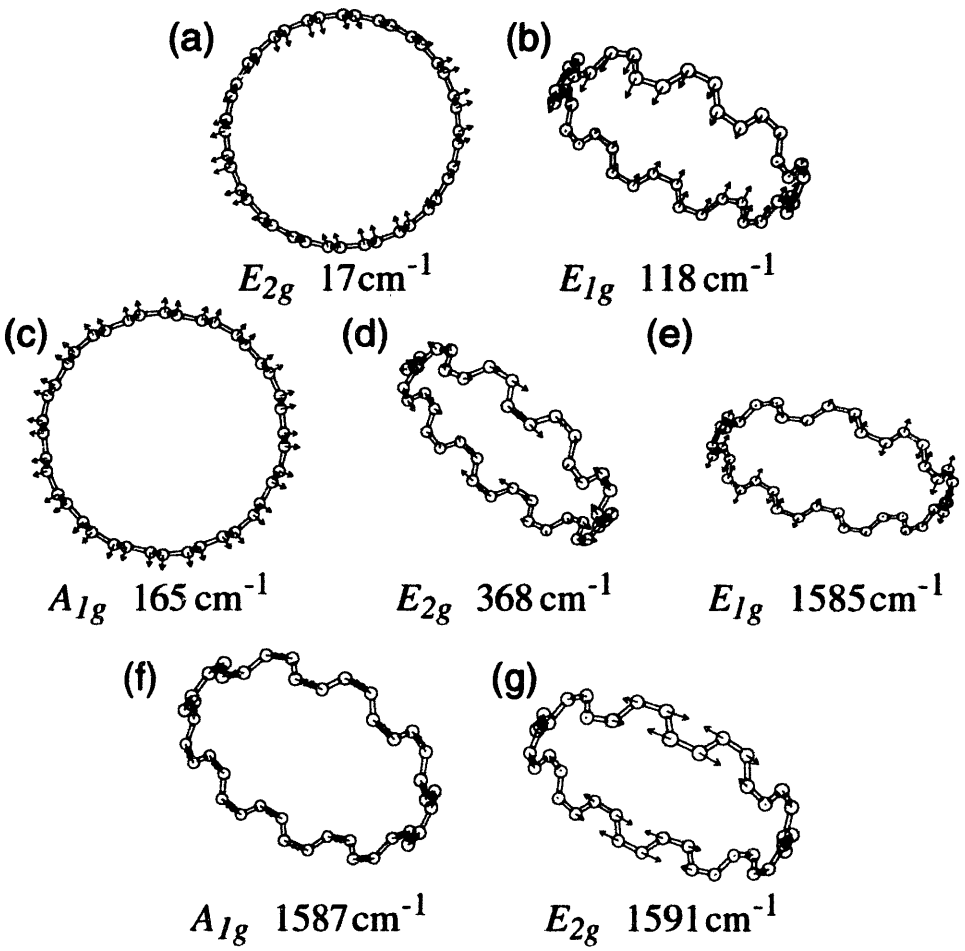

Figure 2-17: The calculated Raman mode atomic displacements, frequencies, and symmetries for selected normal modes for the (10,10) nanotube modes. The symmetry and the frequencies for these modes are not strongly dependent on the chirality of the nanotube. In the figure, we show the displacements for only one of the two modes in the doubly degenerate E_{1g} and E_{2g} modes [102].

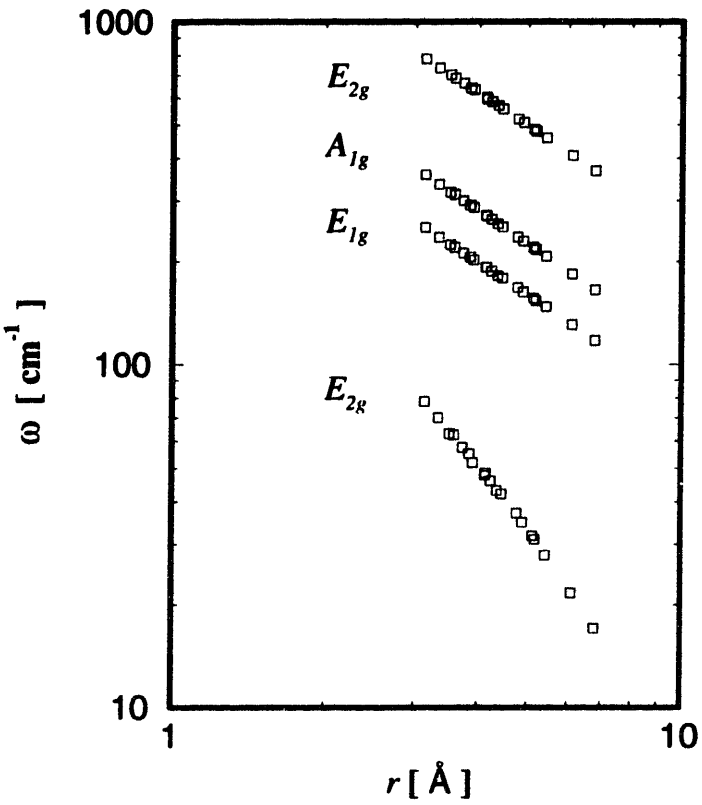

Figure 2-18: Log-log plot of the lower Raman mode frequencies [below 500 cm^{-1} for (10,10) nanotubes], as a function of carbon nanotube radius $r = d_t/2$ [102, 107].

of the SWNT Raman spectrum (~1600cm^{-1}): two $A\,(A_{1g})$, two doubly-degenerate $E_1\,(E_{1g})$, and two doubly-degenerate $E_2\,(E_{2g})$ modes. For each symmetry mode in zigzag and armchair nanotubes (symmorphic groups), the atomic vibrations can be along the tube axis direction, or along the circumferential direction. Because of the high symmetry, only three of the six peaks can be seen in a Raman spectrum. For general chiral tubes (non-symmorphic groups), the direction of the atomic vibrations is no longer parallel or perpendicular to the tube axis, but rather depends on the chiral angle, and six peaks can appear in the Raman spectra. These normal mode patterns can be very useful for the interpretation of the observed Raman spectra, especially with regard to polarization phenomena, as will be discussed in section 4.5.1 for semiconducting nanotubes.

For the lower frequency Raman-active modes [below 500 cm^{-1} for (10,10) nanotubes], the mode frequencies ω shift systematically with increasing diameter, as

shown in the log-log plot of ω in Fig. 2-18 as a function of the carbon nanotube radius $r = d_t/2$ for (n, m) in the range $(8 \leq n \leq 10,\ 0 \leq m \leq n)$. Figure 2-18 clearly shows straight line dependences of $\log\omega$ on $\log d_t$ for all four low frequency Raman modes on this log-log plot, thus indicating a power law dependence of $\omega(d_t)$ on d_t. No significant chirality dependence is found for the mode frequencies for these modes, which is consistent with the fact that the energy gap of a semiconducting nanotube and the strain energy depend primarily on the nanotube radius and are only weakly dependent on the chiral angle θ [81, 98]. From the slopes of $\omega(d_t)$ for this range of d_t (see Fig. 2-18), we conclude that, except for the lowest E_{2g} mode, the frequencies are approximately inversely proportional to d_t. The frequency $\omega_{2g}(d_t)$ of the lowest E_{2g} mode has a predicted dependence of $d_t^{-1.95\pm0.03}$, which is approximately quadratic (in $1/d_t^2$). The power law predicted for the A_{1g} radial breathing mode frequency $\omega^0_{\rm RBM}(d_t)$ for an isolated SWNT valid in the range $0.6\,{\rm nm} \leq d_t \leq 1.4\,{\rm nm}$ is

$$\omega^0_{\rm RBM}(d_t) = \omega^0_{(10,10)} \left[\frac{d_{(10,10)}}{d_t}\right]^{1.0017\pm0.0007}, \tag{2.28}$$

which is very close to linear (in $1/d_t$) and this relation is used by experimentalists as a secondary characterization tool for the diameter distribution in isolated SWNT samples. When the SWNTs are in bundles, inter-tube interactions become important and modifications to Eq. (2.28) are necessary. In Eq. (2.28) $\omega^0_{(10,10)}$ and $d_{(10,10)}$ are, respectively, the mode frequency and diameter of isolated (10,10) armchair nanotubes, which have been given by $\omega^0_{(10,10)}$=169 cm^{-1} and $d_{(10,10)}$= 1.375 nm [102].

More precise use of the radial breathing mode (RBM) frequency to probe the properties, or diameter distribution, of SWNTs embedded in bundles of SWNTs requires that the inter-tube interactions be considered [4, 120]. The expression linking the radial breathing mode $\omega_{\rm RBM}$ to the nanotube diameter d_t has been reported to be well approximated by the expression

$$\omega_{\rm RBM} = \Delta\omega_{\rm RBM} + \omega^0_{\rm RBM} = \Delta\omega_{\rm RBM} + \omega^0_{(10,10)} d_{(10,10)}/d_t \tag{2.29}$$

where ω^0_{RBM} is the radial breathing mode frequency for an isolated SWNT, $\Delta\omega_{\mathrm{RBM}}$ is a frequency upshift which is a constant for nanotube diameters near to that of a (10,10) armchair nanotube $d_{(10,10)}$, and $\omega^0_{(10,10)}$ is the radial breathing mode frequency of an isolated (10,10) nanotube. The calculated values of these parameters vary from one research group to another, but some typical values are: $\Delta\omega_{\mathrm{RBM}} = 14\,\mathrm{cm}^{-1}$ [120], $6.5\,\mathrm{cm}^{-1}$ [4] and $6\,\mathrm{cm}^{-1}$ [46], and $\omega^0_{(10,10)}d_{(10,10)} = 224\,\mathrm{cm}^{-1}\mathrm{nm}$ [120], $232\,\mathrm{cm}^{-1}\mathrm{nm}$ [4], and $214\,\mathrm{cm}^{-1}\mathrm{nm}$ [46]. Since these parameter values were obtained by fits of the measured ω_{RBM} to Eq. (2.29) for a limited range of nanotube diameters (0.7–1.5 nm), the values of these parameters should be considered in pairs. Interestingly, both sets of parameters listed above arrive at about the same RBM frequency [Eq. (2.29)] for a (10,10) nanotube in a bundle, i.e. $176\text{–}177\,\mathrm{cm}^{-1}$.

Chapter 3

Light Scattering under Non-Resonance and Resonance Conditions

3.1 Introduction

In this chapter the general theory of light scattering is discussed. We begin by summarizing the general theory of light scattering in section 3.2 under the usual assumption that the electronic and ionic motions can be decoupled under the so-called *Born – Oppenheimer Approximation*, and we develop an expression for the Raman scattering cross-section. We then go on (in sect. 3.3) to look in detail at the different terms in the polarizability tensor. We study how the assumptions of the energy of the photon being far from resonance, or being in resonance with an allowed electronic transition, affect terms of the polarizability tensor, in particular, their resolution into the A, B, C, and D scattering terms. We then go on to discuss how the symmetry of the lattice vibrations comes into play in these different scattering terms.

In section 3.4, we will briefly discuss resonance Raman intensities, while in the last section of the chapter (3.5) we will look at the two different lineshapes that can be used to analyze Raman spectra, the Lorentzian lineshape and the Breit–Wigner–Fano

lineshape.

3.2 Theory of Light Scattering in Electron-Lattice Coupled Systems

3.2.1 The Born-Oppenheimer Approximation

The spin-independent Hamiltonian for an electron-lattice system, which can be given by [71]

$$H = H_{el} + H_{ion} + H_{el-ion} \tag{3.1}$$

where

$$H_{el} = -\sum_{k} \frac{\hbar^2}{2m}\nabla_k^2 + \frac{1}{8\pi\epsilon_0}\sum_{k,k'}{}' \frac{e^2}{|\mathbf{r_k} - \mathbf{r'_k}|} \tag{3.2}$$

$$H_{ion} = -\sum_{i} \frac{\hbar^2}{2M_i}\nabla_i^2 + \frac{1}{2}\sum_{i,i'}{}' V_{ion}(\mathbf{R_i} - \mathbf{R'_i}) \tag{3.3}$$

$$H_{el-ion} = \sum_{k,i} V_{el-ion}(\mathbf{r_k} - \mathbf{R_i}). \tag{3.4}$$

In the above equations, e is the electronic charge, m is the electron mass, M_i are the masses of the ions, and the no-double counting-restricted($'$) sums are over electron (i) and ion (k) indices; $\mathbf{r_k}$ and $\mathbf{R_i}$ are then the electronic and ionic spatial coordinates. In a dynamic lattice, the difficulty in solving Schroedinger's equation, $H\Psi = E\Psi$, lies primarily in the crystal field term, H_{el-ion}. Born and Oppenheimer developed a method to deal with this problem in which the dynamics of the electronic and ionic subsystems could be decoupled (the so-called *Adiabatic* approximation). As a first approximation, however, we first consider the motion of the electrons in the static lattice:

$$(H_{el} + H_{el-ion})\psi(\{\mathbf{r_k}, \mathbf{R_i}\}) = E_{el}(\{\mathbf{R_i}\})\psi(\{\mathbf{r_k}, \mathbf{R_i}\}). \tag{3.5}$$

In the above Schroedinger equation, $\psi(\{\mathbf{r_k}, \mathbf{R_i}\})$ and $E_{el}(\{\mathbf{R_i}\})$ are the eigenfunction and eigenenergy of the electronic Hamiltonian as a function of all electronic and ionic

positions. It is then assumed that the total solution of the combined electron-lattice problem can be written as $\Psi(\{\mathbf{r_k}, \mathbf{R_i}\}) = \psi(\{\mathbf{r_k}, \mathbf{R_i}\})\phi(\{\mathbf{R_i}\})$ which then gives for the complete Schroedinger equation

$$H\Psi = (H_{el} + H_{ion} + H_{el-ion})\psi\phi \tag{3.6}$$

$$= \psi(H_{ion} + E_{el})\phi - \sum_i \frac{\hbar^2}{2M_i}(\phi\nabla_i^2\psi + 2\nabla_i\phi \cdot \nabla_i\psi). \tag{3.7}$$

We now invoke the afore-mentioned adiabatic approximation in that, since the motion of the electrons is much faster than that of the ions, the last two terms involving ionic spatial derivatives end up being quite small. Omission of these terms essentially amounts to decoupling the electron and ion motion so that the total energy of the system, E, can be given by

$$(H_{ion} + E_{el})\phi(\{\mathbf{R_i}\}) = E\phi(\{\mathbf{R_i}\}). \tag{3.8}$$

The above equation describes the *ionic* eigenfunctions, and can be explicitly written as

$$\left[\sum_i \frac{\hbar^2}{2M_i}\nabla_i^2 + \frac{1}{2}\sum_{ii'}{}' V_{ion}(\mathbf{q_i} - \mathbf{q_i'})\right]\phi(\{\mathbf{q_i}\}) = (E - E_{el})\phi(\{\mathbf{q_i}\}) \tag{3.9}$$

where $\mathbf{q_i} = \mathbf{R_i} - \mathbf{R_i^0}$ are the ionic displacements from the equilibrium positions. A crude approximation to the eigenstates of the electrons could be found by using some mean value of $\mathbf{R_i}$ in the H_{el-ion} term in Eq. 3.5 (this is the so-called Condon approximation). The solution to the above coupled dynamic lattice equation is easily solved using a harmonic oscillator approximation and describing the motion of the ions in terms of normal modes, Q_j, where the ionic eigenstates are now products of harmonic oscillator functions:

$$|\phi\{(Q_j)\}\rangle = \prod_j^{3N-6} |n_j\rangle \tag{3.10}$$

with average eigenenergies given by

$$E - E_{el} = \sum_j \hbar\omega_j(\langle n_j\rangle + \frac{1}{2}), \tag{3.11}$$

where ω_j is the angular frequency of the jth (phonon) mode which has an average occupation number, $\langle n_j\rangle$ given by Bose-Einstein statistics.

3.3 Raman Scattering Cross Section

Kramers and Heisenberg [60] first treated the problem of light scattering involving the summation-over-states, which was later extended by Dirac [23] using radiation field theory. The total scattered power from an electron-lattice transition can be written as [114]

$$P_{f\leftarrow i} = I_0\sigma_{f\leftarrow i}(E_L) \tag{3.12}$$

where the i and f refer to a Raman transition between two states $|i\rangle$ and $|f\rangle$ of a scattering system, where I_0 is the irradiance of the incident radiation (given in W m^{-2}) and $\sigma_{f\leftarrow i}(E_L)$ is the scattering cross section for a photon with energy E_L. When expressed in terms of the transition polarizability tensor

$$P_{fi} \propto (\nu_0 \pm \nu_{fi})^4 I_0 \sum_{\rho,\sigma}[\alpha_{\rho\sigma}]_{fi}[\alpha_{\rho\sigma}]^*_{fi} \tag{3.13}$$

where ν_0 and ν_{fi} are the wavenumbers of the exciting line and of the Raman transition $|f\rangle \leftarrow |i\rangle$, respectively, and $[\alpha_{\rho\sigma}]_{fi}$ is the $\rho\sigma$th element of the transition polarizability tensor:

$$[\alpha_{\rho\sigma}]_{fi} = \frac{1}{hc}\sum_r \frac{[\mu_\rho]_{fr}[\mu_\sigma]_{ri}}{\nu_{ri} - \nu_0 + i\Gamma_r} + \frac{[\mu_\sigma]_{fr}[\mu_\rho]_{ri}}{\nu_{rf} + \nu_0 + i\Gamma_r}. \tag{3.14}$$

In this equation $[\mu_\rho]_{fr}$ is the ρth component of the transition dipole moment associated with the transition $|f\rangle \leftarrow |r\rangle$ and $i\Gamma_r$ is a damping factor, which is related to the lifetime of the state $|r\rangle$. Strictly, the summation is over all states $|r\rangle$ of the system, including $|i\rangle$ and $|f\rangle$, but it has been shown that, for Raman scattering, $|i\rangle$ and $|f\rangle$ may be excluded from the sum. Clearly, the resonant Raman (RRS) effect occurs

when $\mu_0 \sim \mu_{ri}$, resulting in an increase of $[\alpha_{\rho\sigma}]_{fi}$ and consequently an increase in Raman intensity. First we examine normal (i.e. non-resonant) Raman scattering and then we will study Raman scattering under resonant conditions [19].

3.3.1 Normal Raman Scattering

When we invoke the adiabatic Born-Oppenheimer approximation, the vibronic states $|i\rangle$, $|f\rangle$, and $|r\rangle$ are formed by products of the pure vibrational and the pure electronic states. The electronic states are referred to some fixed position of the nuclei and are parametrically dependent on the normal coordinate, Q_k, of the molecule. If we use the labels $|g\rangle$ and $|e\rangle$ for the ground and excited electronic states, respectively, and $|m\rangle$, $|n\rangle$, $|v\rangle$ to represent the vibrational states of the scattering species, we can express the vibronic states as:

$|i\rangle = |gm\rangle = |g\rangle|m\rangle$

$|f\rangle = |gn\rangle = |g\rangle|n\rangle$

$|r\rangle = |ev\rangle = |e\rangle|v\rangle$

The transition polarizability can then be expressed as:

$$[\alpha_{\rho\sigma}]_{gn,gm} = \frac{1}{hc}\sum_{ev}\left(\frac{\langle n|[\mu_\rho]_{ge}|v\rangle\langle v|[\mu_\sigma]_{eg}|m\rangle}{\nu_{ev,gm} - \nu_0 + i\Gamma_{ev}} + \frac{\langle n|[\mu_\sigma]_{ge}|v\rangle\langle v|[\mu_\rho]_{eg}|m\rangle}{\nu_{ev,gn} + \nu_0 + i\Gamma_{ev}}\right) \qquad (3.15)$$

where $[\mu_\rho]_{ge}$ is the pure electronic transition moment associated with the transition $|g\rangle \leftarrow |e\rangle$. Under the adiabatic Born-Oppenheimer condition, the electronic transition moment depends very little on the normal coordinates of the system (Q_k). We can therefore express $[\mu_\rho]_{ge}$ as a rapidly converging Taylor series expanded about the equilibrium position:

$$[\mu_\rho]_{ge} = [\mu_\rho]^0_{ge} + \sum_k [\mu_\rho]'_{ge} Q_k + \ldots\ldots \qquad (3.16)$$

where $[\mu_\rho]'_{ge}=\partial/\partial Q_k$, and the higher order terms are negligibly small. We can now

re-write the matrix elements as:

$$\langle n|[\mu_\rho]_{ge}|v\rangle = [\mu_\rho]^0_{ge}\langle n|v\rangle + \sum_k [\mu_\rho]'_{ge}\langle n|Q_k|v\rangle. \tag{3.17}$$

In the ideal limit of excitations far away from any allowed electronic absorption we can make the approximations that (1) the denominators in the transition polarizability are large and insensitive to the vibrational quantum numbers m, n and v (so the difference $\nu_{ev,gm}$ and $\nu_{ev,gn}$ may be neglected), (2) the states $|m\rangle$ represent a complete orthonormal set and satisfy the closure relation $\sum_v |v\rangle\langle v|=1$, (3) and since $(\nu_{ev,gm} - \nu_0)$ and $(\nu_{eg,gn} + \nu_0)$ are much larger than the damping factor $(i\Gamma_{ev})$, it may be neglected. After we make the approximations, and use the relation

$$(\nu_e - \nu_0)^{-1} + (\nu_e - \nu_0)^{-1} = 2\nu_e(\nu_e^2 - \nu_0^2)^{-1} \tag{3.18}$$

then the transition polarizability will finally be expressed as:

$$\begin{aligned}
[\alpha_{\rho\sigma}]_{gn,gm} &= \frac{1}{hc}\sum_e \frac{2\nu_e}{(\nu_e^2 - \nu_0^2)}[\mu_\rho]^0_{ge}[\mu_\sigma]^0_{eg}\langle n|m\rangle \\
&+ \frac{1}{hc}\sum_e\sum_k \frac{2\nu_e}{(\nu_e^2 - \nu_0^2)}\{[\mu_\rho]'_{ge}[\mu_\sigma]^0_{eg} + [\mu_\rho]^0_{ge}[\mu_\sigma]'_{eg}\}\langle n|Q_k|m\rangle \\
&+ \frac{1}{hc}\sum_e\sum_{k,k'} \frac{2\nu_e}{(\nu_e^2 - \nu_0^2)}[\mu_\rho]'_{ge}[\mu_\sigma]'_{eg}\langle n|Q_kQ_{k'}|m\rangle
\end{aligned} \tag{3.19}$$

The first term describes Rayleigh scattering ($\langle n|m\rangle = \delta_{nm}$), the second term ($\langle n|Q_k|m\rangle$) contains both Stokes and anti-Stokes scattering terms ($n = m\pm1$), and the third term describes the first overtones ($k = k'$) and combination terms ($k \neq k'$).

3.3.2 Resonance Raman Scattering

Although the Born-Oppenheimer approximation is assumed to still be valid, we cannot make the other assumptions as those from normal Raman scattering: (1) we cannot invokes the closure relation ($\sum_v |v\rangle\langle v|=1$), since the denominator is depen-

dent on the quantum number v; (2) the difference $(\nu_{ev,gm} - \nu_0)$ is on the order of the damping factor $(i\Gamma_{ev})$, so it cannot be neglected; and (3) the first-order term $([\mu_\rho]'_{ge}=\partial/\partial Q_k)$ in the Taylor expansion of Eq. 3.16 needs to be defined explicitly.

In the Herzberg-Teller perturbation description of vibronic coupling, the derivative of the transition moment arises because the variation in the Hamiltonian with respect to the normal coordinate Q_k can couple the state $|e\rangle$ with other states $|s\rangle$ of the appropriate symmetry, such as

$$[\mu_\rho]_{ge} = [\mu_\rho]^0_{ge} + \sum_s \sum_k [\mu_\rho]^0_{gs} \frac{h^k_{es}}{\Delta\nu_{es}} Q_k + ... \tag{3.20}$$

where $|s\rangle$ represents another excited state. As before, the higher order terms are generally negligible.

The term h^k_{es}/Δ_{es} is a measure of the strength of vibronic coupling of the states $|e\rangle$ and $|s\rangle$ via the normal coordinate Q_k. The Herzberg-Teller expansion is only valid for weak vibronic coupling, i.e. within the framework of the adiabatic Born-Oppenheimer approximation.

As ν_0 approaches some particular transition wavenumber $\nu_{ev,gm}$, the relevant excited state will dominate the sum over states. The non-resonant part of the transition polarizability may be neglected at resonance. When we apply these considerations to Eq. 3.15, there are four contributions to the transition polarizability:

$$h^k_{es} = \langle e|\delta H/\delta Q_k|s\rangle_{Q_{k=0}} \tag{3.21}$$

$$[\alpha_{\rho\sigma}]_{gn,gm} = A + B + C + D \tag{3.22}$$

where:

$$A = \frac{1}{hc}[\mu_\rho]^0_{ge}[\mu_\sigma]^0_{eg} \sum_v \frac{\langle n_g|v_e\rangle\langle v_e|m_g\rangle}{\nu_{ev,gm} - \nu_0 + i\Gamma_{ev}} \tag{3.23}$$

$$B = \frac{1}{h^2c^2} \sum_{s\neq e} [\mu_\rho]^0_{gs}[\mu_\sigma]^0_{eg} \frac{h^k_{se}}{\Delta\nu_{se}} \sum_v \frac{\langle n_g|Q_k|v_e\rangle\langle v_e|m_g\rangle}{\nu_{ev,gm} - \nu_0 + i\Gamma_{ev}}$$

$$+ \frac{1}{h^2c^2}\sum_{s\neq e}[\mu_\rho]^0_{ge}[\mu_\sigma]^0_{sg}\frac{h^k_{es}}{\Delta\nu_{es}}\sum_v \frac{\langle n_g|v_e\rangle\langle v_e|Q_k|m_g\rangle}{\nu_{ev,gm}-\nu_0+i\Gamma_{ev}} \tag{3.24}$$

$$\begin{aligned} C &= \frac{1}{h^2c^2}\sum_{s\neq g}[\mu_\rho]^0_{se}[\mu_\sigma]^0_{eg}\frac{h^k_{gs}}{\Delta\nu_{gs}}\sum_v \frac{\langle n_g|Q_k|v_e\rangle\langle v_e|m_g\rangle}{\nu_{ev,gm}-\nu_0+i\Gamma_{ev}} \\ &+ \frac{1}{h^2c^2}\sum_{s\neq g}[\mu_\rho]^0_{ge}[\mu_\sigma]^0_{es}\frac{h^k_{sg}}{\Delta\nu_{sg}}\sum_v \frac{\langle n_g|v_e\rangle\langle v_e|Q_k|m_g\rangle}{\nu_{ev,gm}-\nu_0+i\Gamma_{ev}} \end{aligned} \tag{3.25}$$

$$D = \frac{1}{h^3c^3}\sum_{s,s'\neq e}[\mu_\rho]^0_{gs}[\mu_\sigma]^0_{s'g}\frac{h^k_{es}h^{k'}_{es'}}{\Delta\nu_{es}\Delta\nu_{es'}}\sum_v \frac{\langle n_g|Q_k|v_e\rangle\langle v_e|Q'_k|m_g\rangle}{\nu_{ev,gm}-\nu_0+i\Gamma_{ev}} \tag{3.26}$$

3.3.3 A-Term Resonance Raman Scattering

For the A-term contribution (Eq. 3.23) to be non-zero, two conditions must be satisfied: (1) It is necessary that the transition dipole moments $[\mu_\rho]^0_{ge}$ and $[\mu_\sigma]^0_{eg}$ are non-zero (i.e., are electric-dipole-allowed), which requires excitation at an intense absorption band, such as one of the charge transfer (CT) or π-π^* type. (2) The vibrational overlap integrals (Franck-Condon factors), $\langle n_g|v_e\rangle\langle v_e|m_g\rangle$, must be non-zero for some values of v, and so the vibrational wavefunctions χ_n and χ_v must overlap (i.e. be non-orthogonal). For any vibrational mode μ_k of a molecule, the non-orthogonality will occur if there is either (a) a difference of vibrational wavunumber ($\nu^e_k \neq \nu^g_k$) as a result of a change in shape of the potential energy surface, or (b) a displacement of the potential energy minimum along the normal coordinate, ΔQ_k. Symmetry dictates that such a displacement may only occur for totally symmetric modes unless the molecule symmetry is altered in the excited state. Usually a significant change of the vibrational wavenumber occurs only where there is a displacement (Fig. 3-1) of the potential energy minimum ($\Delta Q \neq 0$). Dependent on the magnitude of the ΔQ, the Franck-Condon factors, $\langle n_g|v_e\rangle\langle v_e|m_g\rangle$, may have appreciable size for up to several quanta of n. Thus the A-term can give rise to overtones of intensity comparable to the fundamental. This has particular importance in Chapter 6, where the overtones of Raman features for carbon nanotubes will be analyzed.

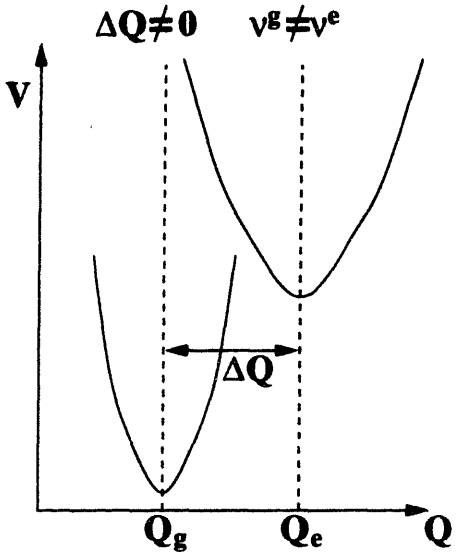

Figure 3-1: Potential energy diagrams for the ground state (g) and the resonant excited state (e).

3.3.4 B-Term Resonance Raman Scattering

The B-term (Eq. 3.24) comes from vibronic coupling of the resonant state (e) to other excited states (s). Its magnitude is dependent on the vibronic coupling integral h^k_{es}, on the products of vibrational transition integrals and overlaps integrals, e.g. $\langle n_g|Q_k|v_e\rangle\langle v_e|m_g\rangle$, on the transition dipole moments $[\mu_\rho]^0_{ge}$ and $[\mu_\sigma]^0_{sg}$ and on the energy difference between the coupled states, $hc(\nu_s - \nu_e)$. For the B-term to be non-zero, both the resonant transition ($|e\rangle \leftarrow |g\rangle$) and the transition $|s\rangle \leftarrow |g\rangle$ should be electric-dipole-allowed. B-term activity may be expected for both totally symmetric and totally non-symmetric vibrations. However, the factor $h^k_{es}(\nu_s - \nu_e)^{-1}$ in the denominator of the equation usually makes the B-term much smaller than the A-term, and it is usually significant only for fundamentals (n=1).

3.3.5 C- and D-Term Resonance Raman Scattering

For the C-term (Eq. 3.25), it is the ground state that vibronically couples to other excited states, as indicated by the vibronic coupling integrals h^k_{gs} and h^k_{sg}. This C-term is assumed to be negligibly small due to the large energy difference between the ground and excited states.

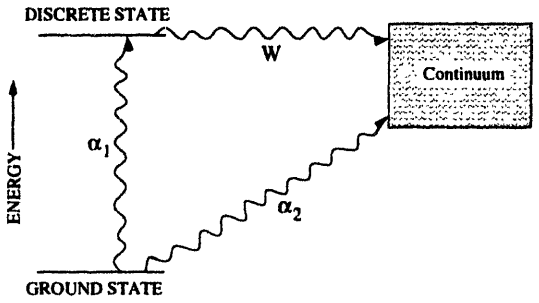

Figure 3-2: Energy level diagram for Breit–Wigner–Fano interference. Here W is the matrix element for a non-radiative decay.

The D-term (Eq. 3.26) is also much smaller than the B-term. It involves vibronic coupling of the resonant state (e) to two other excited states (s and s') through the vibronic integrals h^k_{es} and $h^{k'}_{es'}$, and may give rise to first overtones ($k = k'$) and binary combinations ($k \neq k'$) of both totally symmetric and totally non-symmetric modes.

3.4 Raman Lineshapes

Usually a superposition of Lorentzian phonon lineshapes, which take into account the phonon lifetime (or decay) and some increase in linewidth due to inhomogeneous broadening processes, adequately describes the Raman spectrum. An asymmetric lineshape is observed in the Raman spectrum at times, and in this case the coupling of excitations must be considered. For the carbon nanotubes, a Breit–Wigner–Fano lineshape [36] is at times observed in the Raman spectrum. In this case, there is some coupling of the phonon line to a continuum. We consider this asymmetric lineshape in the next section.

3.4.1 Raman Scattering from Coupled Electron-Phonon Excitations

U. Fano [36] referred to the coupling in the Breit–Wigner–Fano (B–W–F) process as auto-ionization. In the B–W–F process there are two scattering channels [112] into

the same heavily damped final state (see Fig. 3-2), one direct

$$\langle 2|\alpha_2|0\rangle \tag{3.27}$$

and one indirect, via the discrete state

$$\langle 2|W|1\rangle\langle 1|\alpha_1|0\rangle \tag{3.28}$$

where W is a matrix element describing a non-radiative transition from the discrete state to the continuum. The lineshape resulting from this kind of interaction is given by

$$\mathrm{I}(\nu) = \mathrm{I}_o[1 + 2(\nu - \nu_o)/q\Gamma]^2]/[1 + [2(\nu - \nu_o)/\Gamma]^2] \tag{3.29}$$

which is related to a Lorentzian lineshape in the limit that the interaction parameter $(1/\mathrm{q}) \rightarrow 0$, where q a dimensionless constant given by

$$q = \langle 1|\alpha_1|0\rangle/\pi\langle 1|W|2\rangle\langle 2|\alpha_2|0\rangle, \tag{3.30}$$

and the width Γ is related to the strength of the matrix element (coupling) between the discrete line and the continuum

$$\Gamma = \pi[\langle 1|W|2\rangle]^2. \tag{3.31}$$

The width of the resulting B–W–F lineshape is proportional to the square of the matrix element coupling the discrete line and the continuum, and thus a broader B–W–F peak would indicate increased coupling. The interaction parameter (1/q) is related to the coupling matrix element; if q is negative (positive), then the strongest coupling is to a continuum located at a lower (higher) energy than the discrete state. The B–W–F lineshape has been used to fit Raman peaks resulting from the coupling of phonons to interband hole transitions in p-doped silicon [54]. In Chapter 5, I will use this asymmetric Breit–Wigner–Fano lineshape to perform comparative fits to Raman bands attributed to metallic and semiconducting carbon nanotubes.

Chapter 4

First-Order Raman Spectra

4.1 Introduction

Raman spectroscopy has proven to be a very effective tool in the study of not only the vibrational properties of the carbon nanotubes, but also the one-dimensional electronic density of states through the resonant Raman effect. When the incident or Raman scattered photon match the energy of an allowed transition in the carbon nanotubes, then the Raman signal is increased by over six orders of magnitude relative to the non-resonant signal. Due to the very sharp van Hove singularities in the one-dimensional electronic density of states, optical absorption is very high under resonant conditions, and thus the carbon nanotubes are excellent Raman scatterers. In our work we have used several different samples of carbon nanotubes with narrow Gaussian diameter distributions, and we have been able to probe the predicted 1D behaviors in the Raman spectra.

The first-order Raman spectra of single-walled carbon nanotubes are dominated by three features, two of which were introduced in Chapter 2. The radial breathing mode (RBM) feature is located at very low frequency shifts ($\sim$200 cm^{-1}) and involves a radially symmetric motion of the carbon atoms about the axis of the nanotubes. This feature yields structural information about the nanotubes, since the RBM frequency is inversely proportional to the nanotube diameter (see Fig. 2-18). In the intermediate frequency region is a small feature located at $\sim$1300 cm^{-1} (D-band), which has a

completely different and highly dispersive resonant behavior, i.e., it shifts to higher frequencies as the laser excitation energy is increased. This feature is associated with a 2D resonant behavior of the carbon nanotubes. The high frequency tangential mode (TM) region involves motion of the carbon along the nanotube axis, about the circumference, and all tangential directions in between. Study of this mode has yielded a lot of information about the electronic density of states and the nature of the electron-phonon coupling. I will compared the resonant behavior of two samples of carbon nanotubes with different diameter distributions in to point out what important electronic and vibrational information these different regions of the Raman spectra can yield.

4.2 Experimental Details

The carbon nanotube samples used for this study were formulated using the electric arc discharge method. The first sample (S1) was produced using a 1 at.% Ni and 1 at.% Fe catalyst mixture, resulting in d_t=1.35 $\pm$0.20 nm. Carbolex Inc. of Lexington, Kentucky used the Electric arc discharge method with a 4:1 catalyst mixture of Ni:Y to produce SWNTS with a narrow distribution of large diameters, $d_t = 1.49 \pm 0.20$ nm (sample S2). The diameter distribution of samples S1 and S2 were determined through the location of their radial breathing mode frequencies, as will be discussed in section 4.4. The third sample (S3) used a 2.6 at.% Ni, 0.7 at.% Fe and 0.7 at.% Co catalyst mixture along with 0.75 at.% FeS, resulting in SWNTs with a broad distribution of diameters (mean diameter of 1.85 nm) [68]. The diameter distribution of samples S3 was determined from transmission electron microscopy measurements.

Raman spectroscopy experiments were performed under ambient conditions in a backscattering configuration using several laser excitation lines. These lines include the argon lines at 457.9 nm (2.71 eV), 488 nm (2.54 eV) and 514.5 nm (2.41 eV); the krypton lines at 568.2 nm (2.19 eV), 647.1 nm (1.92 eV) and 676.4 nm (1.83 eV); the He-Ne line at 632.8 nm (1.96 eV); and a diode laser at 785 nm (1.58 eV). The spectral resolution of the different Raman systems for phonons was better than 2 cm^{-1}. A

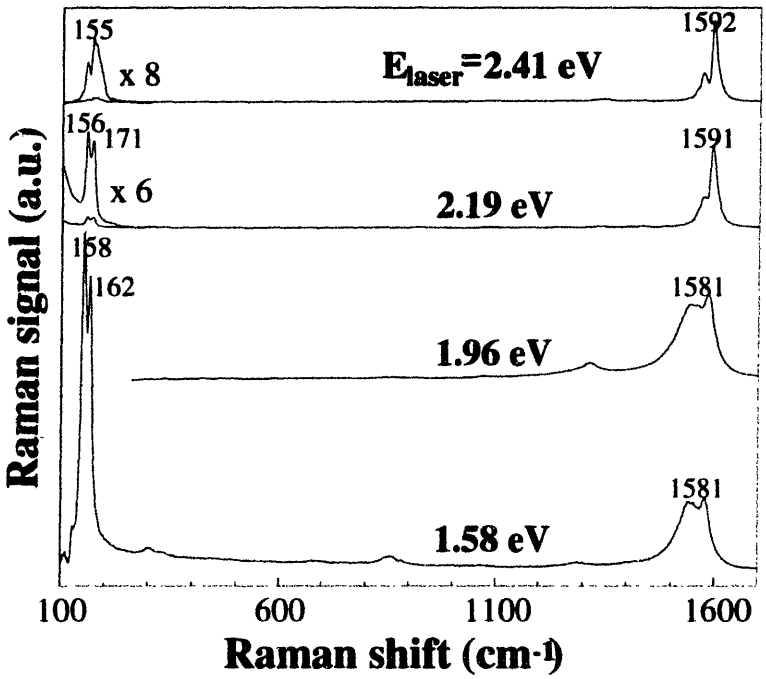

Figure 4-1: First-order Raman spectra for carbon nanotubes with diameter distribution $d_t = 1.49 \pm 0.20\,\text{nm}$ over the phonon frequency range 100–1700 cm^{-1} for $E_{\text{laser}} = 1.58, 1.96, 2.19$, and 2.41 eV. The radial breathing mode feature for $E_{\text{laser}} = 2.19$ and 2.41 eV has been magnified.

Ti:Sapphire laser at 830 nm (1.49 eV) was also used, where the spectral resolution for this system was $\sim 8\,\text{cm}^{-1}$.

4.3 First-order Raman Spectrum

Figure 4-1 shows the entire first-order Raman spectra for sample S2. The two dominant features in the Raman spectra are the radial breathing modes (ω_{RBM}) located in the 150–200 cm^{-1} range, and the tangential modes (ω_{tang}) located in the 1530–1610 cm^{-1} range). All four spectra are plotted so that the tangential G-band features ($\sim$1600 cm^{-1}) have the same intensity, in order to draw attention to the changes in relative intensity of ω_{RBM} vs. ω_{tang} as E_{laser} is varied.

Both of these features in the first-order Raman spectra are resonantly enhanced when the laser excitation energy (E_{laser}) is equal to the energy separation between a singularity in the 1D electron density of states in the valence and conduction bands,

such as the E_{ii} energy separations (between the ith conduction band singularity and the ith valence band singularity), $E_{ii} = E_{11}, E_{22}, \ldots$. A summary of all the E_{ii} energy separations for all (n, m) nanotubes up to a nanotube diameter of 3.0 nm is given in Fig. 2-10. A similar figure was first published by Kataura [52] for $\gamma_0 = 2.75\,\text{eV}$, but the plot presented in this thesis is for $\gamma_0 = 2.90\,\text{eV}$ [99], which provides a better fit to our Raman data. Resonant enhancement occurs not only for the incident photon but also for the scattered photon, so that the conditions for resonant Raman scattering include $E_{\text{laser}} = E_{ii}$ and $E_{\text{laser}} = E_{ii} + \hbar\omega_{\text{phonon}}$ for the Stokes process. However, the resonance behavior of the radial breathing mode feature and the tangential mode feature is quite different, as will be pointed out in the next two sections.

Since the energy separations $E_{ii}(d_t)$ in Fig. 2-10 are strongly dependent on the diameter d_t of the nanotubes, a change in the energy of the incident laser beam E_{laser} results in the resonant Raman excitation of *different* nanotubes. Furthermore, $\hbar\omega_{\text{phonon}}$ can be as large as 0.2 eV for first-order scattering processes for the tangential modes. Therefore, the specific nanotubes in a given sample that are excited in the radial breathing mode Raman scattering process can be different from the nanotubes that participate in the tangential mode scattering process.

4.4 Radial Breathing Mode

The radial breathing mode frequency ω_{RBM} depends on the nanotube diameter d_t in accordance with $\omega_{\text{RBM}} \propto 1/d_t$, independent of the chirality of the nanotube. Therefore, a variation of E_{laser} results in a variation of the observed ω_{RBM} due to selective resonance with *different* nanotubes, as has been studied extensively by many authors [6, 27, 45, 49, 62, 63, 95, 109, 116]. The RBM feature at any given value of E_{laser} is a superposition of the individual RBM mode frequencies for all of the given nanotubes in the sample for which E_{laser} matches an electronic resonance. Thus, from Fig. 4-1, the RBM feature is seen to change both relative intensities and position in the first-order Raman spectrum relative to the tangential band feature with differing laser excitation energies. Figure 4-2 shows how the shape of the RBM feature varies

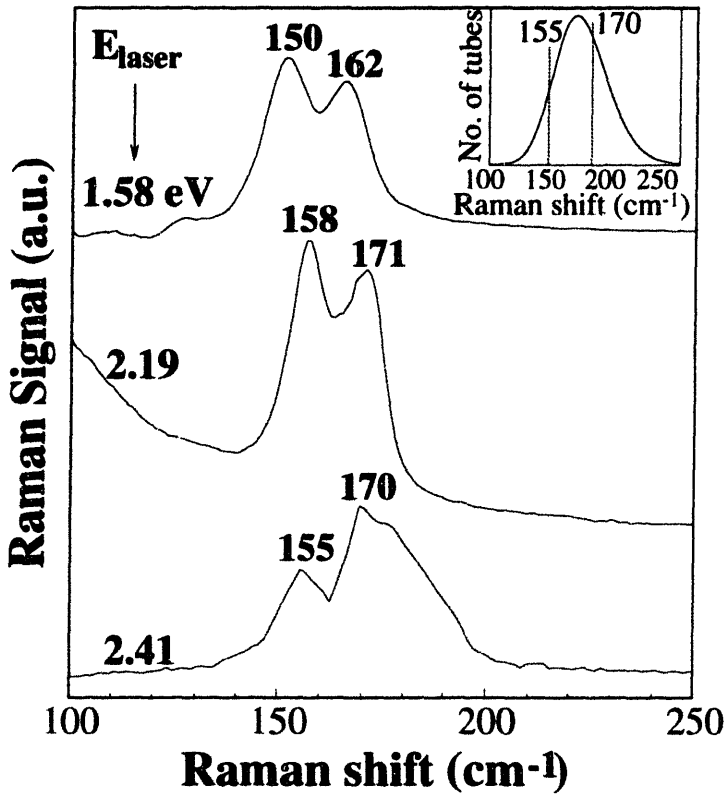

Figure 4-2: The radial breathing mode feature in the Raman spectra for carbon nanotubes with a diameter distribution $d_t = 1.49 \pm 0.20\,\text{nm}$ collected using $E_{\text{laser}} = 1.58, 2.19$, and $2.41\,\text{eV}$. The inset shows a modified Gaussian distribution for the number of nanotubes in the sample expected to have a given radial breathing mode frequency. The distribution is centered at $165\,\text{cm}^{-1}$, and vertical lines show the location of $155\,\text{cm}^{-1}$ and $170\,\text{cm}^{-1}$.

Table 4.1: Summary of the peak frequencies and linewidths (in cm^{-1}) of the Lorentzian components for the radial breathing modes (ω_{RBM}) for the indicated E_{laser} values (see Fig. 4-2) from SWNTs with d_t=1.49±0.2 nm.

	ω_{RBM}							
E_{laser}	1.58 eV		2.19 eV		2.41 eV		2.54 eV	
Line	ω	Γ	ω	Γ	ω	Γ	ω	Γ
#1	—	—	—	—	142	10	—	—
#2	150	14	—	—	155	10	—	—
#3	162	11	158	10	—	—	159	11
#4	—	—	171	10	170	10	—	—
#5	—	—	—	—	178	10	176	9
#6	—	—	—	—	188	10	—	—

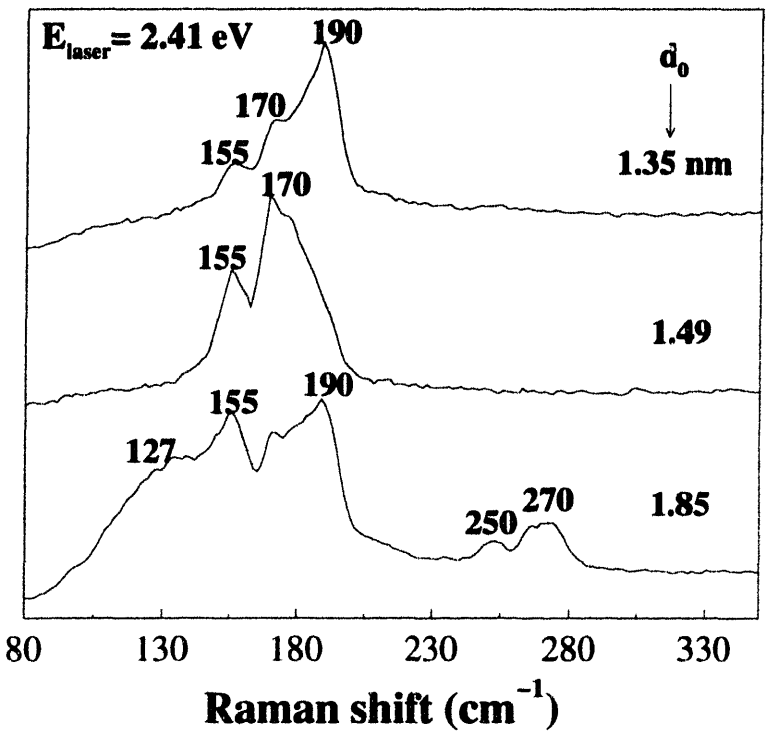

Figure 4-3: Radial breathing mode feature in the Raman spectra for carbon nanotubes with peak diameters d_0=1.35, 1.49 and 1.85 nm for $E_{\text{laser}} = 2.41$ eV, showing different spectra, thereby reflecting the different diameter distributions of the three samples.

with laser excitation energy. Fits to these features using Lorentzian oscillators with similar widths are listed in Table 4.1. The center frequency of the RBM feature for this sample of SWNTs is located at $\sim$165 cm^{-1}.

Once you have the radial breathing mode feature of a sample of SWNTs, collected for several different laser excitation energies, then you can use the proportionality of the RBM peak frequency to the inverse diameter (d_t) to gauge the diameter distribution of the sample using relations like Eq. 2.29, which take into account intertube interactions. Fig. 4-3 displays the RBM feature collected using $E_{\text{laser}} = 2.41$ eV for the three samples of SWNTs denoted by S1, S2, and S3. The center of the feature is seen to shift to lower values of wavenumber shift (cm^{-1}) as the center diameter of the sample d_0 becomes larger, consistent with the relation $\omega_{\text{RBM}} \propto 1/d_t$.

Many groups have tried to predict the resonant intensity changes in the radial breathing mode region as a function of laser excitation energy. However, they have

had mixed success. We, however, have put our efforts into extracting information from the higher frequency Raman features ($\sim$1600 cm^{-1}) of the carbon nanotubes.

4.5 Tangential G-band

The characteristic features of the tangential G-band modes of the first-order spectrum are also due to resonant Raman effects associated with singularities in the 1D electron density of states, but the tangential mode spectra have characteristics that are different from those of the radial breathing modes. Results for the first-order resonant Raman spectra for the tangential modes for the three nanotube samples used in this study are presented in Fig. 4-4 for several different laser excitation energies. The tangential G-band feature ($\sim$1600 cm^{-1}) of single-wall carbon nanotubes, which comes from out-of-phase C=C bond stretching motion of the carbon atoms (as displayed for (10,10) armchair nanotubes in Fig. 2-17) similar to the motion of the Raman active E_{2g_2} mode of graphite located at 1582 cm^{-1}, is expected to exhibit only a very weak dependence on nanotube diameter (see Fig. 2-16) [26, 27]. However, we note that there are differences in the Raman G-band as a function of not only $E_{\rm laser}$ for a given sample, but also as a function of d_t for a given value of $E_{\rm laser}$ as expected from Fig. 4-6. The tangential G-band feature of sample S1 has a narrow lineshape, shown in Fig. 4-4 (a) for $E_{\rm laser} \geq 2.41$ eV and $E_{\rm laser} \leq 1.58$ eV, for a wide range of $E_{\rm laser}$, and is essentially independent of $E_{\rm laser}$[89]. Similarly for sample S2, Raman tangential band features for $E_{\rm laser} = 1.49$ eV and for $E_{\rm laser} \geq 2.19$ eV are also quite similar (Fig. 4-4 (b)). However, in a narrow laser excitation energy range for both samples, the Raman tangential band feature is seen to broaden and the center of the broad feature is downshifted to a lower value of Raman shift. For sample S1, this energy window occurs in the range $1.8 \leq E_{\rm laser} \leq 2.4$ eV, while for sample S2, this window is located at lower laser excitation energies ($1.5 \leq E_{\rm laser} \leq 2.1$ eV). The sample with the broad distribution of larger diameters (S3) is seen to undergo only modest changes in lineshape with differing values of laser excitation energy. These startling differences among the three samples will be shown to be attributable to the

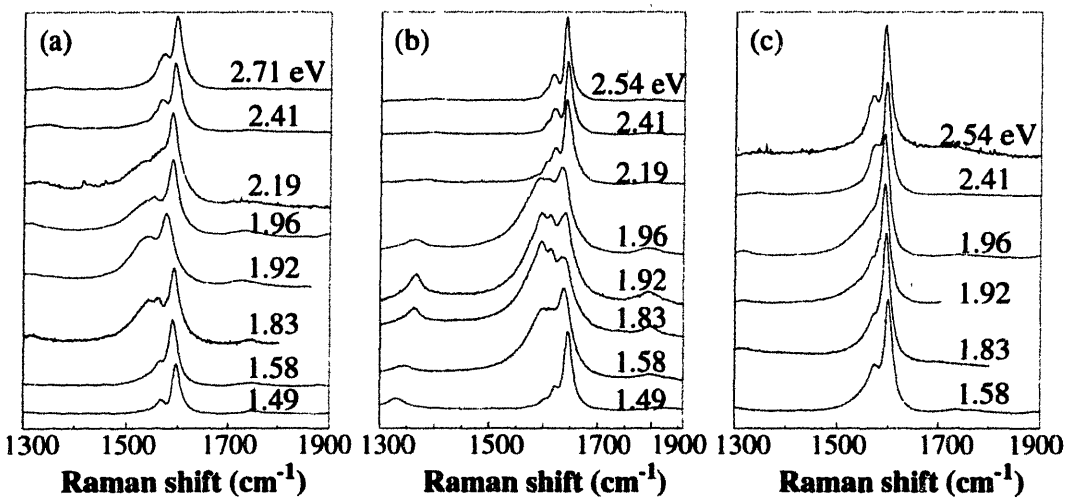

Figure 4-4: Tangential band feature in the Raman spectra for samples of carbon nanotubes with narrow diameter distributions (a) $d_t = 1.35 \pm 0.2\,\text{nm}$ (S1) and (b) $d_t = 1.49 \pm 0.20\,\text{nm}$ (S2), as well as (c) a sample with a broad distribution of diameters peaked at d_t=1.85 nm (S3), collected using the indicated values of laser excitation energy (E_{laser}).

1D nature of the electronic density of states for carbon nanotubes due to transitions between the van Hove singularities in the valence and conduction bands.

In 1998, Pimenta *et al.* [89] performed detailed lineshape analysis of the different Raman G-band features from resonant Raman experiments on a sample of carbon nanotubes synthesized by the group at Rice University using the laser vaporization of a carbon target containing 1 to 2 at.% of Ni/Co in a furnace at 1200°C [95, 118]. The diameter distribution for these SWNTs (obtained from TEM contrast images) is $d_t = 1.37 \pm 0.18\,\text{nm}$, which is quite similar to those of sample S1, and so their resonant Raman spectra should also be similar. Their SWNTs also exhibited a narrow lineshape for $E_{\text{laser}} \geq 2.4\,\text{eV}$ and $E_{\text{laser}} \geq 1.8\,\text{eV}$ and the broad, downshifted G-band feature for $1.8 \leq E_{\text{laser}} \leq 2.4\,\text{eV}$, in good agreement with the data in Fig. 4-4 (a).

Each narrow G-band feature from the different values of E_{laser} was fit with 6 Lorentzian oscillators located at 1522, 1547, 1563, 1570, 1593 and 1601 cm^{-1} [89]. These oscillators had similar positions, widths and relative intensities for the different laser lines, with the 1590 cm^{-1} peak being the most intense [89]. The broader downshifted G-band feature was attributed to the superposition of 4 broader (resonantly enhanced) Lorentzian oscillators located at 1515, 1540, 1558 and 1581 cm^{-1} with the

6 narrower Lorentzian lines in the spectrum. The narrow Raman bands obtained for $E_{\text{laser}} \geq 2.4\,\text{eV}$ and $E_{\text{laser}} \geq 1.8\,\text{eV}$ were attributed to the resonant enhancement of the phonon modes for the semiconducting nanotubes, which are believed to make up approximately 2/3 of the sample. By citing corroborating evidence such as the STS/STM measurements (see Fig. 2-12), Pimenta *et al.* showed that the narrow energy window where the broad downshifted G-band feature appeared is described by the resonant enhancement of the phonon modes for the metallic carbon nanotubes in the sample when either the incident laser photon or the Raman scattered photon matched the first allowed electronic transitions of the metallic nanotubes (see Eq. 4.1) in the sample. They showed this connection explicitly by plotting the expected Raman intensity for the metallic nanotubes within the metallic window for the nanotube samples using the following formula:

$$\begin{aligned} I(E_{\text{laser}}) = & \sum_{d=1.1\text{nm}}^{1.6\text{nm}} A \exp\left[\frac{-(d-d_0)^2}{\Delta d^2/4}\right] \\ & \times \left[(E_{11}^{\text{M}}(d) - E_{\text{laser}})^2 + \Gamma_e^2/4\right]^{-1} \\ & \times \left[(E_{11}^{\text{M}}(d) - E_{\text{laser}} + E_{\text{phonon}})^2 + \Gamma_e^2/4\right]^{-1}, \end{aligned} \tag{4.1}$$

where d_0 and Δd are the center and the width of the Gaussian distribution of nanotube diameters, and E_{phonon} is the average energy (0.197 eV) of the tangential G-band phonons. They approximated $I(E_{\text{laser}})$ by normalizing the intensity of the most intense "metallic" component (the $1540\,\text{cm}^{-1}$ peak) to the most intense "semiconducting" component (the $1593\,\text{cm}^{-1}$ peak), since there were no calibrations available for absolute intensities, and most spectral traces showing contributions from metallic nanotubes (as will be seen in Fig. 4-9) also showed contributions from semiconducting nanotubes. The damping factor Γ_e avoids the divergence of the double resonance expression for the Raman cross-section [97] and accounts for the width of the singularities in the electronic DOS and the lifetime of the excited state. For the diameter dependence of E_{11}^{M}, Pimenta *et al.* used the expression calculated by White and Mint-

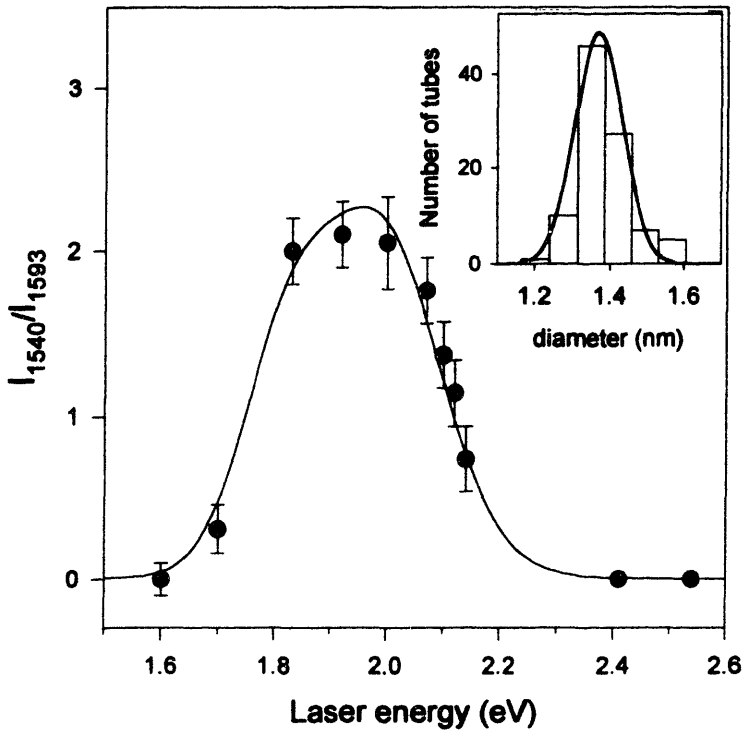

Figure 4-5: The solid circles represent the intensity ratio of the Raman peaks at 1540 and 1593 cm^{-1}, and the solid curve represents the fit to the experimental data using Eqs. (4.1) and (4.2) [89]. The inset shows the distribution of diameters measured by TEM [95] and the Gaussian fit to the diameter distribution data [89].

mire [123], and Charlier and Lambin [16] for armchair nanotubes

$$E_{11}^{\mathrm{M}}(d) = \frac{6a_{\mathrm{C-C}}\gamma_0}{d} \tag{4.2}$$

where $a_{\mathrm{C-C}}$ is the Carbon-Carbon distance and γ_0 is the electronic overlap integral. The best fit of Eqs. (4.1) and (4.2) to the plot of the intensity ratio I_{1540}/I_{1593} vs. E_{laser} measurements in Fig. 4-5 for their SWNT sample ($d_t = 1.37 \pm 0.18\,\mathrm{nm}$), was achieved for $\gamma_0 = 2.95 \pm 0.05\,\mathrm{eV}$, $\Gamma_e = 0.04 \pm 0.02\,\mathrm{eV}$, a full width of the distribution $\Delta E_{11}^{M}(d_t) = 0.24\,\mathrm{eV}$, and a mean value for the energy separation $\langle E_{11}^{M}(d_t)\rangle = 1.84\,\mathrm{eV}$. These values for $\langle E_{11}^{M}(d_t)\rangle$ and $E_{11}^{M}(d_t)$ are in good agreement with the direct measurements of $E_{11}^{M}(d_t)$ by scanning tunneling spectroscopy (STS) (see Fig. 2-12) [124].

In applying this resonant Raman scattering cross-section formula to the three samples from the electric arc discharge method, I found that the energy window for the

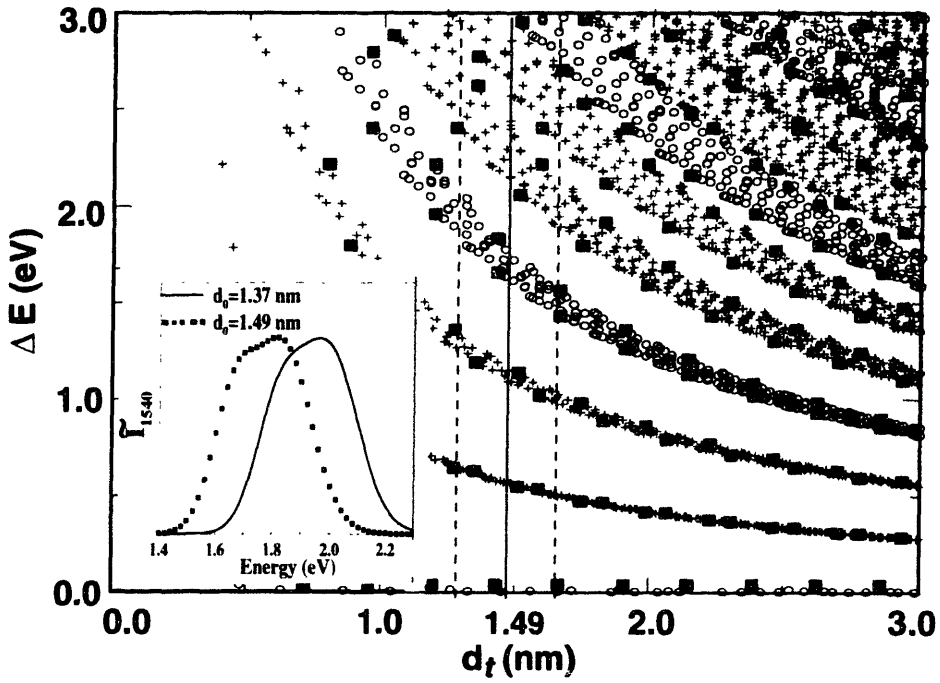

Figure 4-6: Calculation of the energy separations $\Delta E = E_{ii}(d_t)$ for nanotubes with all (n, m) indices [26] as a function of nanotube diameter between $0.7 < d_t < 3.0\,\text{nm}$ (based on prior work of Kataura *et al.* [52]). The calculation of ΔE vs. d_t [103] is based on the tight binding model with $\gamma_0 = 2.90\,\text{eV}$ and $s = 0$, where s is the tight binding overlap integral. The semiconducting and metallic nanotubes are indicated by crosses and open circles, respectively. The filled squares denote the zigzag tubes. The inset shows the experimental range of E_{laser} which is expected to be resonant with metallic nanotubes of diameters $d_t = 1.49 \pm 0.20\,\text{nm}$ (square points) and $d_t = 1.37 \pm 0.18\,\text{nm}$ (solid curve) [89].

resonant enhancement of the phonon modes for the metallic nanotubes in sample S1 corresponded well to that from the laser vaporization nanotubes studied by Pimenta *et al.*, consistent with their similar diameter distributions. In fact, this formula can be applied to sample S2 as well, since it also contains a narrow diameter distribution of nanotubes. The inset to Fig. 4-6 shows a comparison of the calculation of this resonance energy window for the appearance of the broader downshifted Raman feature for the laser vaporization nanotube sample and sample S2. On average, Sample S2 nanotubes are ~9% larger in diameter than sample S1. Consequently, the resonant energies for the metallic window for the 1.49 nm diameter sample (S2) are lowered

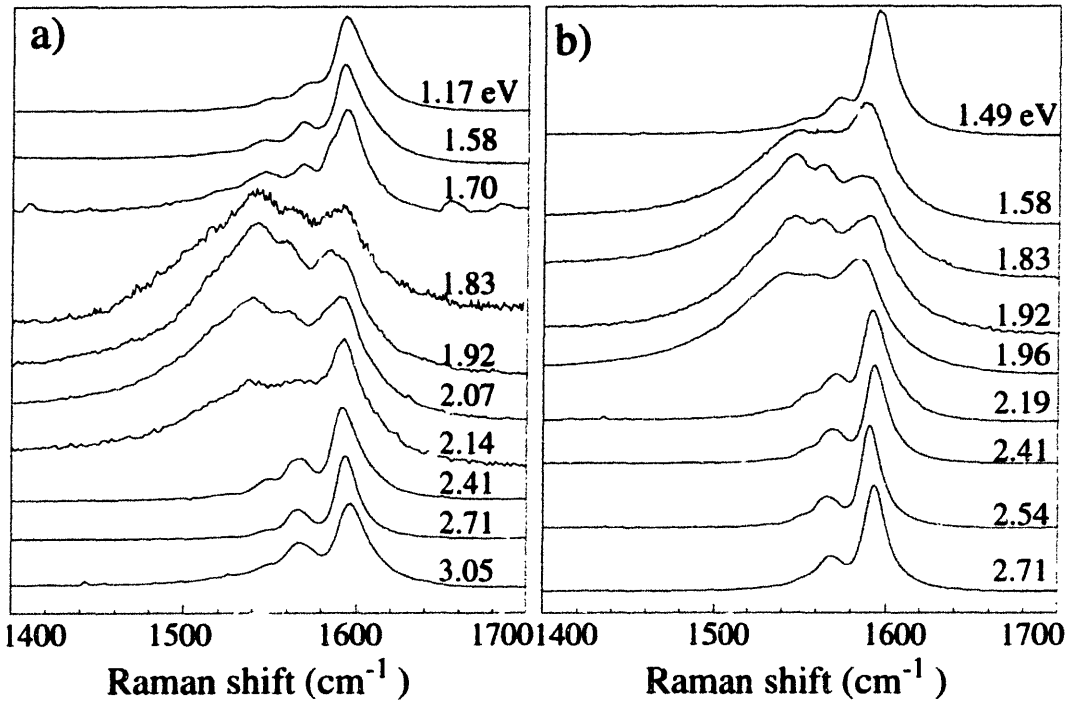

Figure 4-7: Tangential band feature in the Raman spectra for samples of carbon nanotubes with diameter distributions (a) $d_t = 1.37 \pm 0.18$ nm (Ref. [89]) and (b) $d_t = 1.49 \pm 0.20$ nm (sample S2), collected using the indicated values of laser excitation energy (E_{laser}).

with respect to that for the 1.37 nm diameter sample (laser vaporization), as can be seen from the inset to Fig. 4-6 which gives a comparison between the metallic windows calculated for the two samples based on the diameter distribution. In fact, if we compare the resonant Raman spectra of the sample of SWNTs from laser vaporization (d_t = 1.37±0.18 nm) to that from sample S2 (d_t = 1.49±0.18 nm), as shown in Fig. 4-7, we see the remarkable agreement with the calculated metallic resonant enhancement energy window for the two different diameter distributions (inset to Fig. 4-6) and the appearance of the broad tangential band feature.

In order to associate experimental points with the resonant energy window for the metallic nanotubes in the sample, we need to perform detailed lineshape analyses of the tangential G-band from the semiconducting SWNTs. They are also used for normalization in mapping the appearance of the tangential G-band features from the metallic nanotubes, since there are no calibrations available for absolute intensities, and the spectral traces showing contributions from metallic nanotubes for this sample

(shown in Fig. 4-9) also show contributions from semiconducting nanotubes. In the next section I will briefly describe the recent polarized Raman spectroscopy measurements on the tangential G-band from semiconducting SWNTs, which have indicated how to fit these bands.

4.5.1 Polarization Studies of Semiconducting Nanotubes

Polarized Raman spectroscopy measurements were performed by Jorio *et al.* [44] on the narrow Raman G-band feature attributable to semiconducting nanotubes to determine the symmetries of different components of the G-band feature through their behavior for the four different Raman polarization measurement geometries (XX), (XZ), (ZX) and (ZZ), where light is propagating along $\vec{y}$ and the tube axis is along $\vec{z}$. The (ZZ) geometry had the highest Raman intensity, while the intensity from the cross-polarization geometries [(XZ) and (ZX)] was reduced by a factor of 6, where all three were fit using only two Raman bands located at 1567 and 1590 cm^{-1}. The (XX) geometry was fit with four Lorentzian oscillators, with the lowest and highest Lorentzian oscillators located at 1550 and 1607 cm^{-1}.

As was shown in Chapter 2, the tangential G-band feature for carbon nanotubes is a superposition of six phonon modes, two each of A (A_{1g}), E_1 (E_{1g}) and E_2 (E_{2g}) symmetries. The three different symmetries behave differently under these three geometries, where the A (A_{1g}) modes should only appear in the (XX) and (ZZ) geometries, and the E_2 (E_{2g}) in the (XX) geometries (i.e., in the parallel polarization geometries), while the E_1 (E_{1g}) modes should only show up in cross-polarized spectra [(XZ) and (ZX)]. Through solving the dynamic matrix, Saito *et al.* [102] found that, for (10,10) armchair nanotubes, the mode displacements with high intensities are located at 1585 cm^{-1} (E_{1g}), 1587 cm^{-1} (A_{1g}) and 1591 cm^{-1} (E_{2g}). Kahn *et al.* [46] found that the orientation of the hexagon along the nanotube (see Fig. 4-8), i.e., by reducing the chiral angle from θ=30° to θ=0° in going from armchair (θ=30°), through chiral to the other extreme of zigzag nanotubes (θ=0°), in fact, changes the order of the frequencies of these modes, so that for zigzag nanotubes the order is E_{2g}, A_{1g}, then E_{1g} modes (lowest to highest frequencies). Jorio *et al.* [44] attributed the lowest and

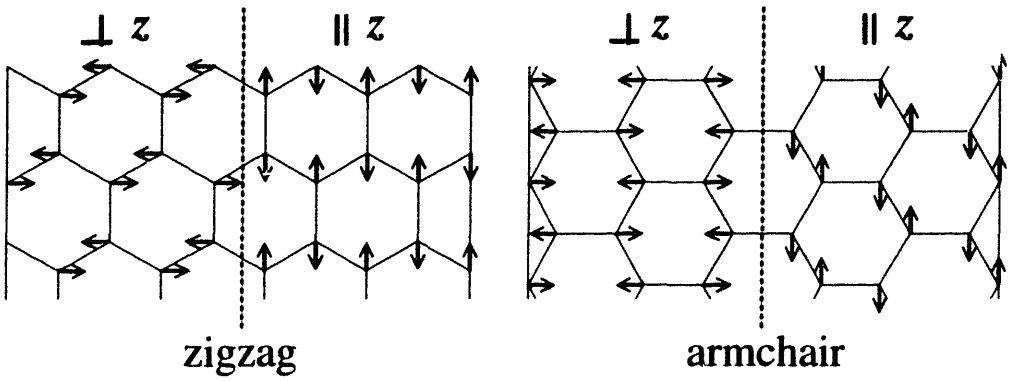

Figure 4-8: The orientation of the hexagons relative to carbon atom displacements perpendicular ($\perp z$) and parallel ($\parallel z$) to the nanotube axis for an armchair and a zigzag nanotube [43].

highest Lorentzian oscillators (1550 and 1607 cm^{-1}) to the E_2 (E_{2g}) mode symmetries, since they only appeared in the (XX) geometry, with the lower frequency coming from zigzag and low chiral angle nanotubes, and the higher frequency coming from high chiral angle nanotubes. The two middle Lorentzian oscillators (1567 and 1591 cm^{-1}) were each attributed to a mixture of an A (A_{1g}) and an E_1 (E_{1g}) mode, which could not be resolved, and where the 1567 cm^{-1} Lorentzian component involves normal mode displacements around the nanotube circumference, and the 1591 cm^{-1} component comes from carbon atom displacements along the axis. All fits to the tangential G-band feature from semiconducting nanotubes in this thesis are therefore made using four Lorentzian oscillators (~1550, 1567, 1591 and 1607 cm^{-1}), in accordance with these polarization studies.

4.5.2 Tangential G-band features of Semiconducting SWNTs

A detailed lineshape analysis of the spectra in Fig. 4-4 (b) is reported here and a summary of the peak frequencies and linewidths of the main components of the first-order tangential band is given in Table 4.2 for four E_{laser} values. The fits to the tangential G-band feature for E_{laser}=1.58 and 2.19 eV are shown in Fig. 4-9. The results show that the same four Lorentzian components are found in the spectra taken at 1.49 (not shown in Table 4.2), 2.19, 2.41, and 2.54 eV, in all cases showing similar

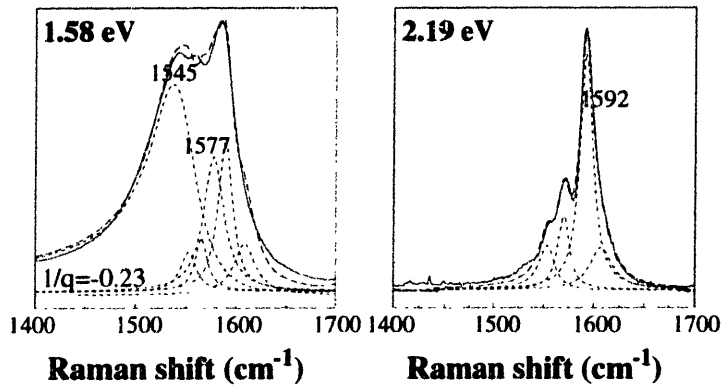

Figure 4-9: Detailed lineshape analysis of the tangential G-band feature from samples of nanotubes with diameters d_0=1.49 nm, collected using E_{laser} = 1.58 eV and 2.19 eV.

peak frequencies, linewidths and relative intensities (Table 4.2). The frequencies, widths and relative intensities used to fit the semiconducting G-band feature are found to vary little for the three different samples used in this study. In the range of E_{laser} where the broader, downshifted tangential G-band feature from metallic nanotubes appear, the features have been fit using either the Breit-Wigner-Fano (interaction) lineshapes or Lorentzian oscillators. Pimenta *et al.* [89] fit the broad features using only Lorentzian oscillators, and noted that the line broadening effects were due to laser-induced electronic resonances involving metallic nanotubes and to the coupling between phonons and conduction electrons in the metallic nanotubes. It is difficult to make a confident determination of the lineshapes best needed to fit the tangential G-band feature from metallic SWNTs because, as can be seen in Fig. 4-9 for $E_{\text{laser}} \sim$ 1.58 eV, whenever the G-band features for metallic nanotubes are resonantly enhanced in the Stokes-scattered photon window, contributions from semiconducting nanotubes are also present. In the next chapter, I will describe how I was able to overcome this obstacle and obtain the Raman bands for *only* metallic nanotubes through performing resonant Raman spectroscopy in the anti-Stokes region of the Raman spectrum.

Without justification at this point, I used a Breit-Wigner-Fano lineshape for the lower frequency metallic component (1545 cm^{-1}) and a Lorentzian oscillator for the higher frequency component (1577 cm^{-1}). The reasoning for this selection of lineshapes will become clear in the next chapter. The normalized intensity of the feature at 1545 cm^{-1} associated with metallic nanotubes is a maximum for $E_{\text{laser}} \sim$ 1.8 eV

Table 4.2: A summary of the peak frequencies and linewidths (in cm^{-1}) of the main components of the tangential band (ω_{tang}) (see Fig. 4-4) of the single-wall carbon nanotubes with $d_t = 1.49 \pm 0.2$ nm, for selected values of E_{laser}. The relative intensity (Rel. Int.) for a given peak is the ratio of that peak intensity to the $\sim$1592 cm^{-1} component for that laser line. The symbols (*) and (†) indicate the Raman bands attributed to metallic and semiconducting nanotubes, respectively.

	1.58 eV			2.19 eV		2.41 eV		2.54 eV	
Rel. Int.	ω	Γ	1/q	ω	Γ	ω	Γ	ω	Γ
3.7	1545*	56	-0.21	—	—	—	—	—	—
0.2	1552†	18	—	1553†	19	1554†	18	1554†	22
0.3	1566†	14	—	1569†	14	1568†	14	1566†	12
0.9	1577*	24	—	—	—	—	—	—	—
1.0	1591†	17	—	1592†	15	1594†	13	1591†	12
0.3	1607†	26	—	1607†	26	1606†	26	1607†	23

(see inset to Fig. 4-6), and here the normalization of $\tilde{I}_{1540}$ is done with respect to the intensity of the 1592 cm^{-1} feature, which is the most intense Lorentzian oscillator associated with semiconducting nanotubes, consistent with Fig. 4-4 (b). The calculated resonance energy window for metallic nanotubes is fit to the experimental data points for sample S1, and the results are compared to the sample prepared by pulsed-laser vaporization (Ref. [89]). In both cases the fit to the metallic window of the nanotubes yielded a value of $\gamma_0 = 2.95 \pm 0.05$ eV, which is consistent with the values of γ_0 used in the calculations by Charlier *et al.* [18] for Fig. 2-9 (3.0 eV) and by Saito *et al.* [99] for Fig. 4-6 (2.9 eV). Equation 4.2 has therefore also been verified for another sample of carbon nanotubes.

4.6 *D*-band Dispersion

One of the interesting features of the Raman spectra in sp^2 carbon materials is the laser energy dependence of the frequency of the disorder-induced *D*-band which is observed between 1250 and 1450 cm^{-1}. The *D*-band is activated in the first-order scattering process by the presence of in-plane substitutional hetero-atoms, vacancies, grain boundaries or other defects and by finite size effects, all of which lower the

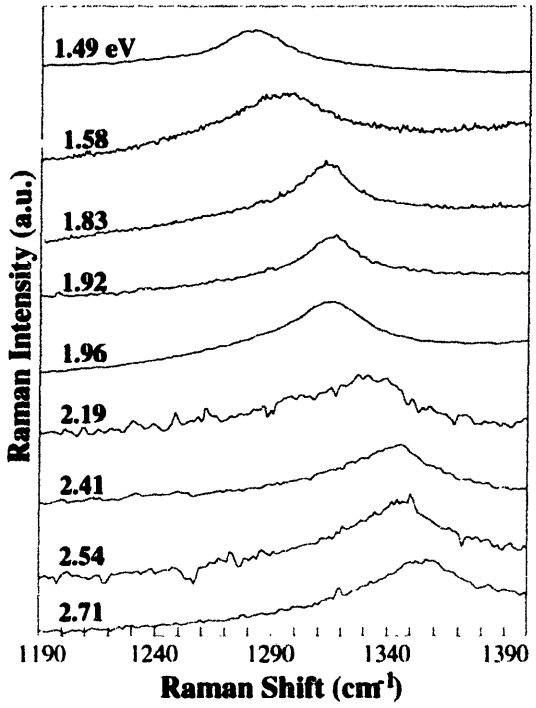

Figure 4-10: Raman spectra in the range 1190–1390 cm^{-1} for SWNTs (d_0=1.49 nm) showing the upshift of the D-band peak frequency with increasing E_{laser}.

crystalline symmetry of the quasi-infinite lattice. The association of the D-band with symmetry-breaking phenomena results in a D-band intensity that is proportional to the phonon density of states shown in Fig. 2-15(c) for graphite and for (10,10) SWNTs. A dominant feature of the second-order Raman spectrum (discussed further in Chapter 6) is the G'-band, which is the overtone of the D-band, and appears in the frequency range 2500–2900 cm^{-1} when the laser excitation energy E_{laser} is varied from 1.0 to 4.5 eV. Furthermore, the second-order G'-band is observed even in the case of crystalline graphite, where the disorder-induced D-band is absent, so that the G'-band is an *intrinsic* property of the 2D graphene lattice. It has been known for about two decades [121], that there is a strong dependence of the peak frequency for the D-band on E_{laser} (see Fig. 4-10), and this phenomenon occurs in a similar way in all kinds of sp^2 carbon materials, such as graphon carbon black [78], hydrogenated amorphous carbon [91], glassy carbon and crystalline graphite [7, 90, 122], and multi-component carbon films [72]. It is believed that the D-band feature observed in bundles of SWNTs has contributions from the SWNTs themselves, perhaps due to a

Table 4.3: Summary of the peak frequencies (ω) and linewidths (Γ) of the D-band feature in the Raman spectrum from sample S2 (see Figs. 4-4 (b) and 4-10). Also listed is the intensity of the D-band feature taken relative to the corresponding tangential G-band feature for each spectrum.

E_{laser}	ω (cm^{-1})	Γ (cm^{-1})	Rel. Int.
1.49	1280	44	0.12
1.58	1287	36	0.05
1.83	1310	40	0.18
1.92	1314	36	0.28
1.96	1314	36	0.20
2.19	1326	66	0.04
2.41	1339	53	0.02
2.54	1344	49	0.02
2.71	1353	55	0.02

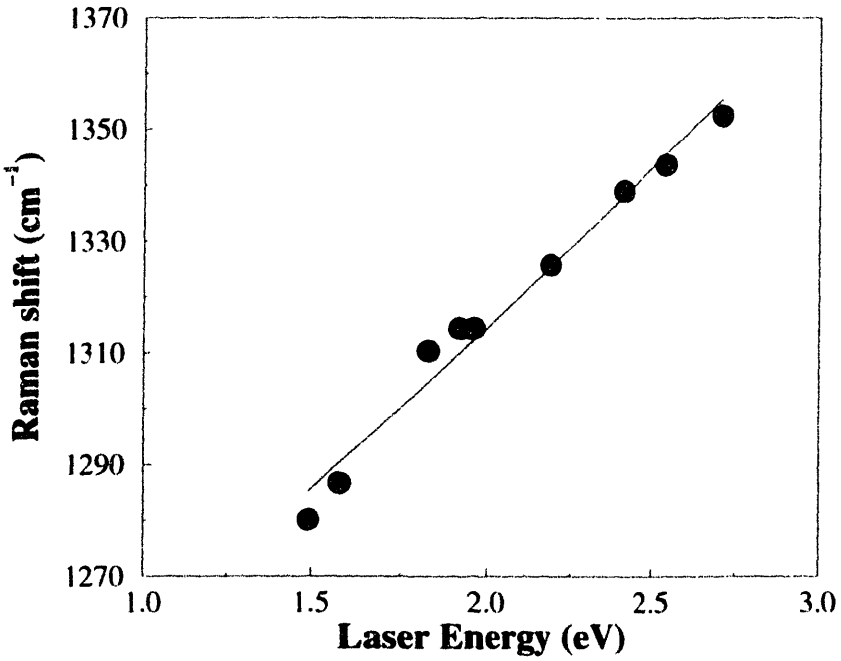

Figure 4-11: Frequency of the 'D-band' for sample S2 (see Fig. 4-10) as a function of laser excitation energy. The line is a least squares fit to the data points. The fit to the data points yields a slope of $57\,\text{cm}^{-1}/\text{eV}$ and an intercept of $1200\,\text{cm}^{-1}$ at $E_{\text{laser}} = 0$ [32].

finite length effect [108], as well as from other carbonaceous materials (e.g. amorphous sp^2 carbon coatings) present in the imperfectly purified SWNT samples that are now available.

Figure 4-12 illustrates the basic mechanism responsible for the laser excitation dependence of the D-band and the G'-band (discussed in Chapter 6) frequencies in sp^2 carbons [7, 74, 90]. In the upper part of Fig. 4-12, we see that electronic transitions between the π and π^* electronic states of 2D graphite with energies corresponding to visible photons only occur in the vicinity of the K point in the Brillouin zone (BZ) through which the Fermi level E_F passes [42, 102]. The phonons associated with the D-band and the G'-band have the same wavevectors Δq as the electronic states Δk which are in resonance with the laser. Moreover, it is argued that these phonons belong to the optic branch that contains the zone center E_{2g_2} graphitic mode, represented by a heavy curve in Fig. 4-12 [42, 102]. The reason why the phonons belonging to this particular optic branch exhibit an especially large Raman cross-section compared to other phonons with the same wavevector Δq is attributed to their breathing-mode displacements (see Fig. 4-13) which would be expected to show strong deformation potential coupling to the electronic states [74]. Referring to Fig. 4-13, we see that for sp^2 carbons all the carbon atoms about the points labeled by $\times$ vibrate through breathing mode atom displacements with respect to point $\times$, while exhibiting typical optical mode displacements with respect to the centers of the other two hexagons in the honeycomb lattice [74]. This symmetric motion of the carbon atoms would then result in the D-band and G'-band features being resonantly enhanced through a Franck-Condon mechanism.

From Fig. 4-4 (b), we see that the D-band increases in intensity relative to the tangential G-band, and becomes narrower as the laser excitation energy is lowered from 2.54 eV. Table 4.3 lists the frequency and linewidth of the D-band feature for each laser excitation energy, and also the intensity of the D-band feature relative to the tangential feature from that spectrum. When E_{laser} >2.1 eV, the D-band is very weak, broad and poorly resolved. However, when 1.6 eV< E_{laser} <2.1 eV, the D-band feature gains in intensity relative to the tangential G-band feature by a factor of 10

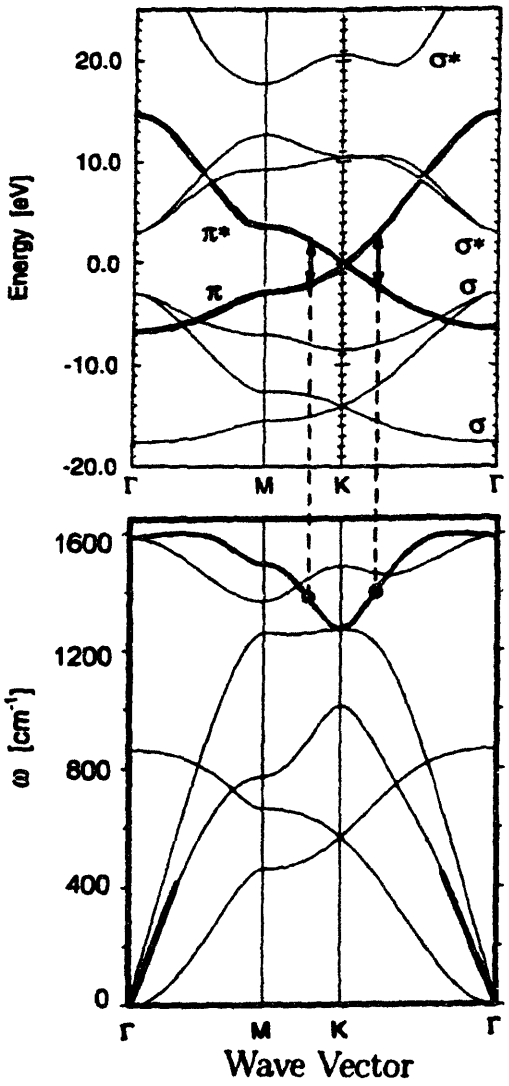

Figure 4-12: Electronic energy bands $E(k)$ (top) and phonon dispersion curves $\omega(q)$ of 2D graphite (bottom) [42, 102]. Both the phonon branch that is strongly coupled to electronic bands in the optical excitation, and the electronic bands near the Fermi level ($E = 0$) that have a dispersion relation that is linear in k are indicated by heavy lines. The initial slope for the low frequency TA phonon branch (which is initially the same along ΓM and along ΓK) is also indicated by heavy lines. The strong coupling between the electrons of wave vector Δk, measured from the K point in the Brillouin zone, to phonons of wave vector $\Delta q = \Delta k$ is responsible for the frequency dependence of the D-band and the G'-band features in the Raman spectra of sp^2 carbons and carbon nanotubes [74].

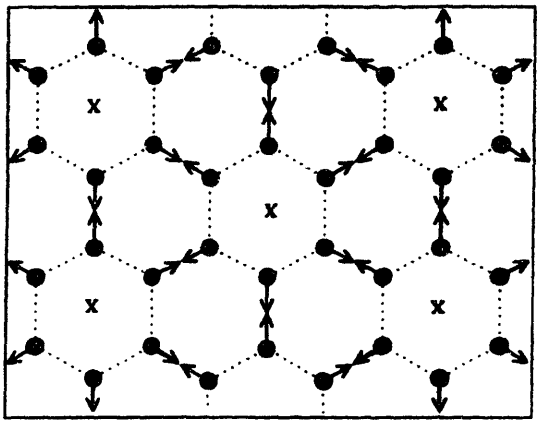

Figure 4-13: Schematic diagram of the atomic displacements (arrows) in the graphene plane for the E_{2g_2} mode at the Γ point, which can be viewed with respect to the unmarked centers of the hexagons. For the atomic motions of the six atoms about the hexagon centers denoted by $\times$, breathing-type displacements are obtained corresponding to normal modes associated with the K point in the Brillouin zone [74].

or more. It then diminishes as the laser excitation energy is lowered further. Thus, the range of energies where this feature D-band is the most prominent coincides with the resonant energy window for the enhancement of the Raman bands attributed to metallic nanotubes. This feature will be found to play a very important role in later chapters of the thesis, particularly in gauging the perturbation of the energy levels of the carbon nanotubes in the surface-enhanced Raman spectroscopy experiments (Chapter 7).

4.7 Conclusions

The resonant Raman spectrum from single-walled carbon nanotubes contains features with completely different types of resonant behavior. The frequency of the radial breathing mode feature is inversely proportional to the nanotube diameter and is used as a measure of the diameter distribution of a given sample of nanotubes. The intermediate region contains the D-band feature, which is associated with disorder-induced 2D dispersion in sp^2 carbons, but may be an intrinsic feature

of the nanotubes. Of particular interest is the high frequency tangential G-band feature which exhibits a narrow lineshape for the semiconducting nanotubes while the resonant enhancement of the Raman bands for metallic carbon nanotubes introduces broader, downshifted features to the Raman band. In Chapter 5, we will study the Raman features attributed to metallic carbon nanotubes in greater detail.

Chapter 5

Anti-Stokes Raman Spectra

5.1 Introduction

The anti-Stokes Raman spectra of single-wall carbon nanotubes (SWNTs) are unique relative to other crystalline systems, especially in exhibiting large asymmetries with regard to their corresponding Stokes spectra [55]. This asymmetry is due to the unique resonant enhancement phenomena arising from their one-dimensional electronic (1D) density of states. The anti-Stokes spectra are therefore selective of specific carbon nanotubes, as previously reported for the Stokes spectra [27, 89, 95], but the anti-Stokes spectra are selective of *different* single wall nanotubes than for the corresponding Stokes spectra at a given laser excitation energy E_{laser}. This Chapter focuses on the unique behavior of the anti-Stokes spectra for the first-order tangential modes of sample S2 (narrow diameter distribution d_t=1.49±0.2 nm), which allows an accurate identification to be made of the range of E_{laser} where only *metallic* nanotubes contribute to the resonant Raman spectra. This will then allow us to perform a detailed lineshape analysis of the Raman bands attributed to metallic nanotubes, devoid of contributions from semiconducting nanotubes.

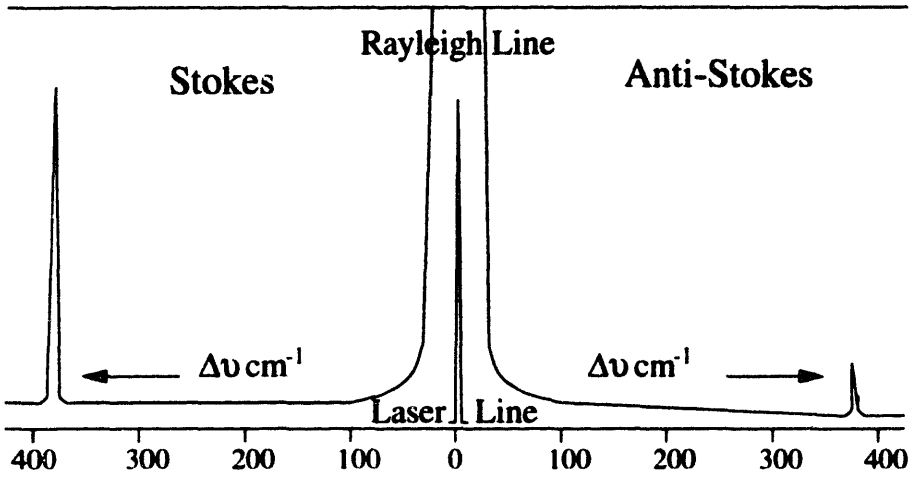

Figure 5-1: Schematic diagram of the Stokes (phonon emission) and anti-Stokes (phonon absorption) scattering regions of the Raman spectrum. Since the anti-Stokes region depends on scattering with existing phonons (determined by thermal population), there is a Boltzmann factor reduction in the intensity of the Raman signal.

5.2 Experimental Details

Raman spectra were collected in both the Stokes and anti-Stokes scattered photon regions (see Fig. 5-1) under ambient conditions in a backscattering configuration using several laser excitation lines, including the krypton lines at 568.2 nm (2.19 eV) and 647.1 nm (1.92 eV); the He-Ne line at 632.8 nm (1.96 eV) and an Al-doped GaAs diode laser at 782 nm (1.58 eV), the last two from a Renishaw Raman microscope system. The spectral resolution of these Raman systems was $\sim 2\,\mathrm{cm}^{-1}$ and the laser power density incident on the sample was always $<40\,\mathrm{W/cm}^2$. We also used a Ti:Sapphire laser at 830 nm (1.49 eV), where the spectral resolution was $\sim 4\,\mathrm{cm}^{-1}$ and the power density was $<1.5\,\mathrm{MW/cm}^2$, using the lowest laser power necessary to observe anti-Stokes spectra with this Raman system.

The sample temperature T_s was measured using the Stokes tangential mode peak frequency as an indicator, where the laser excitation energy (E_{laser}) was chosen so that both the Stokes and anti-Stokes Raman spectra were semiconducting for the given sample of carbon nanotubes. Li *et al.* performed a study comparing the rate of downshift of the tangential G-band feature of semiconducting carbon nanotubes due to laser heating to that from heating using a temperature stage [66], and found that

both followed a linear dependence of

$$\omega_{\text{tang}} \simeq -4.0 \times 10^{-2}\,\text{cm}^{-1}/\text{K} + 1607\,\text{cm}^{-1} \tag{5.1}$$

for the most intense component of the tangential G-band, and so for ω_{tang}=1583 cm^{-1}, the sample temperature is only 600 K.

5.3 Stokes vs. anti-Stokes Asymmetry

Striking differences between the Stokes and anti-Stokes spectra of sample S2 (d_t = 1.49±0.2 nm), from 1200–2800 cm^{-1}, for two different laser excitation energies E_{laser} (1.58 eV and 1.96 eV) are seen in Fig. 5-2, including the first-order tangential G-band (1500–1600 cm^{-1}) and the D-band (1280–1330 cm^{-1}), and also second-order features (combination bands at ~1740 cm^{-1} and 1860–1925 cm^{-1} and the G'-band at 2540–2620 cm^{-1}, an overtone of the D-band). The asymmetries observed between the D-band and the second-order features (combination bands and G'-band) will be discussed in greater detail in Chapter 6. However, the differences in behavior between the Stokes and anti-Stokes tangential G-band spectra for the SWNTs will be discussed in this chapter.

The differences in lineshape between the tangential band for the Stokes and anti-Stokes spectra are shown more clearly in Fig. 5-3, at four different E_{laser} values between 1.49 eV and 2.19 eV. Here we see that the behavior of the Stokes and anti-Stokes spectra for the tangential band each change as a function of E_{laser} and also change relative to one another. The different characteristic lineshapes for the tangential band discussed below allow us to easily distinguish between metallic and semiconducting nanotubes. At E_{laser}=2.19 eV, the Stokes and anti-Stokes spectra are almost the same and both are typical of resonant Raman spectra for semiconducting nanotubes (strongest feature at 1591 cm^{-1}), while at E_{laser}=1.92 eV, the Stokes and anti-Stokes spectra are very different from each other, the Stokes spectrum showing domination by metallic nanotubes (strongest feature at ~1540 cm^{-1}), and the anti-Stokes spectrum

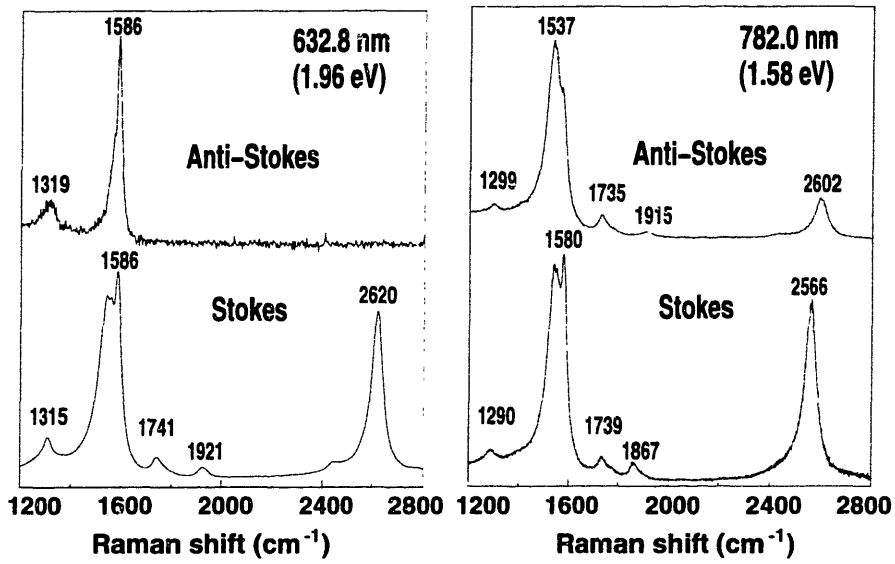

Figure 5-2: Stokes and anti-Stokes Raman spectra for sample S2 (d_t=1.49±0.2 nm) at E_{laser} = 1.58 eV (782 nm) and 1.96 eV (632.8 nm).

showing domination by semiconducting nanotubes. At E_{laser}=1.58 eV both the Stokes and anti-Stokes spectra are characteristic of metallic nanotubes, while at E_{laser}=1.49 eV, the anti-Stokes spectrum is dominated by metallic nanotubes and the Stokes spectrum is typical of semiconducting nanotubes.

5.3.1 Discussion

The unusual Stokes/anti-Stokes asymmetry behavior observed in Fig. 5-3 can be readily explained in terms of the Raman scattering intensity of metallic nanotubes, after some modification to Eq. 4.1:

$$\begin{aligned} I_M = \; & \sum A \exp\left\{\frac{-(d_t-d_0)^2}{\Delta d^2/4}\right\} \\ & \times[(E_{11}^M(d_t) - E_{\text{laser}} \pm E_{\text{ph}})^2 + \Gamma_e^2/4]^{-1} \\ & \times[(E_{11}^M(d_t) - E_{\text{laser}})^2 + \Gamma_e^2/4]^{-1} \end{aligned} \tag{5.2}$$

in which $I_M \equiv I_M(E_{\text{laser}}, d_0)$ is the scattering intensity for the Stokes process (+ sign) and for the anti-Stokes process (− sign) for metallic nanotubes in resonance with the $E_{11}^M(d_t)$ electronic transition between the highest lying valence band van Hove

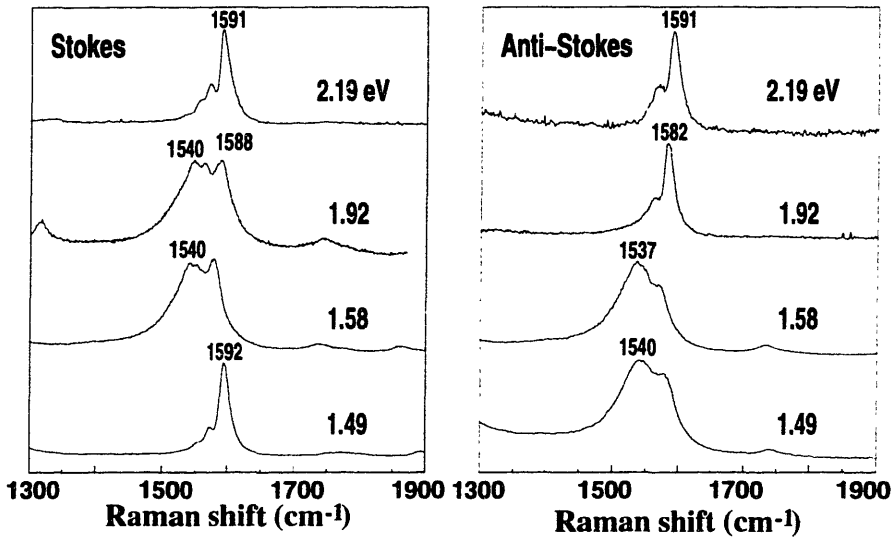

Figure 5-3: Stokes and anti-Stokes Raman spectra for SWNTs of $d_0 = 1.49\,\text{nm}$ taken at four different values of E_{laser}, which show only modest variations in lineshape.

singularity and the lowest lying conduction band singularity in their 1D electronic density of states [26, 89]. The sum in Eq. (5.2) is over all metallic nanotubes having a diameter distribution given by $d_t = d_0 \pm \Delta d$ where d_0 is the average diameter and Δd is the FWHM width of a Gaussian distribution of nanotube diameters. Also E_{ph} denotes the phonon frequency for the tangential band (0.20 eV), Γ_e is a damping parameter determined by fitting experimental data to Eq. (5.2) and A is a dimensionless factor proportional to the Boltzmann factor $\exp(-E_{\text{ph}}/kT)$ for the anti-Stokes process and a constant for the Stokes process [11, 89].

A plot of $I_M(E_{\text{laser}}, d_0)$ for Stokes spectra, based on a fit of Eq. (5.2) to measurements at many laser energies E_{laser} is given in the inset to Fig. 5-4 (solid curve) [11, 89], along with the corresponding predicted $I_M(E_{\text{laser}}, d_0)$ curve for anti-Stokes spectra (dashed curve) using the same Stokes parameters. The central point denoted by an arrow gives the center of the metallic window accurately for nanotubes with diameter d_0, which occurs at 1.69 eV for our nanotube sample ($d_0 = 1.49\,\text{nm}$). Using the formula $E_{11}^M(d_t) = 6a_{\text{C-C}}\gamma_0/d_t$, valid for armchair nanotubes [24], yields a value of $\gamma_0 = 2.95\,\text{eV}$ assuming $a_{\text{C-C}} = 0.142\,\text{nm}$, in agreement with $\gamma_0 = 2.95\,\text{eV}$, obtained from fits of Stokes spectra to Eq. (5.2) for SWNTs with $d_0 = 1.37\,\text{nm}$ (Section 4.5).

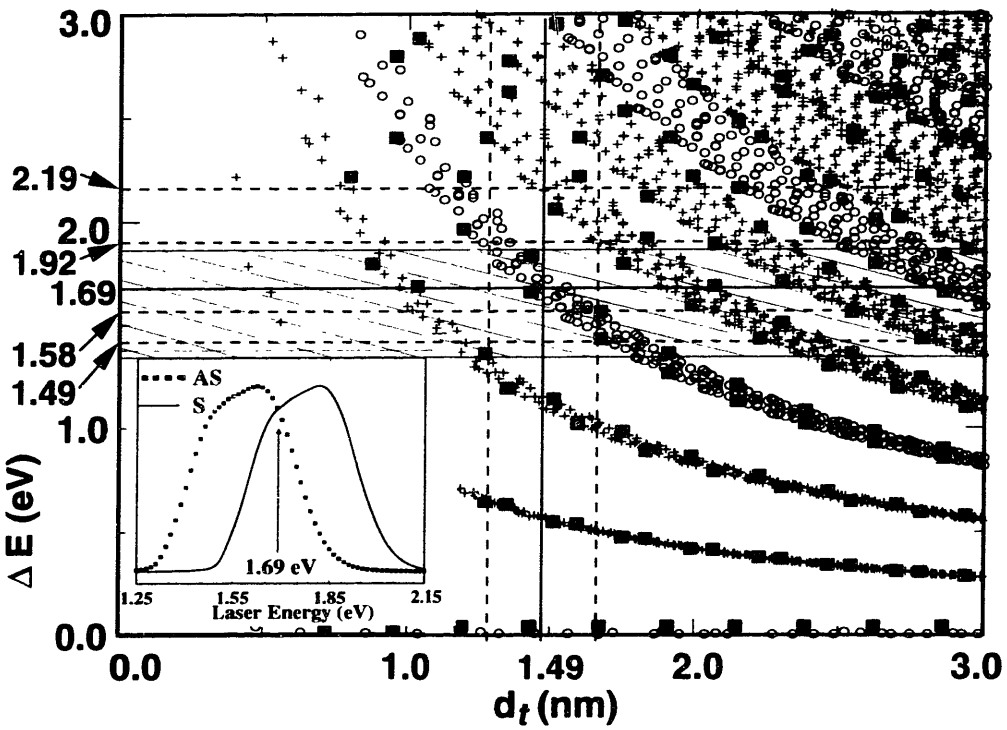

Figure 5-4: Calculation [52] of the energy separations $\Delta E = E_{ii}(d_t)$ for all (n, m) values vs nanotube diameter $0.7 < d_t < 3.0\,\text{nm}$, here re-plotted using a higher value of γ_0 (2.9 eV) [24, 99]. Semiconducting and metallic nanotubes are indicated by crosses and open circles, respectively. Filled squares denote zigzag tubes. The dashed horizontal lines correspond to E_{laser}=1.49, 1.58, 1.92 and 2.19 eV and the vertical lines denote $d_t = 1.49 \pm 0.2\,\text{nm}$ for sample S3. The inset is the calculated $I_M(E_{\text{laser}}, d_0)$ using Eq. (5.2) for the metallic resonance window for Stokes (solid curve) and anti-Stokes (dashed curve) scattering processes, and the arrow at 1.69 eV is at the center of the metallic window (see main figure). The cross-hatch pattern denotes the predicted range of $E_{11}(d_t)$ for metallic nanotubes in the anti-Stokes spectrum.

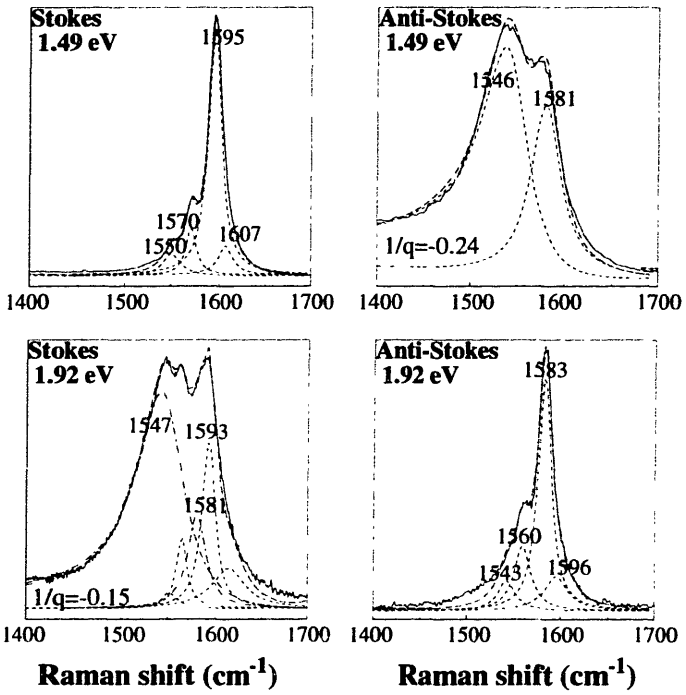

Figure 5-5: Lorentzian fits to the Stokes and anti-Stokes tangential bands for E_{laser} = 1.49 eV and 1.92 eV.

From Fig. 5-4 [52, 99], we predict that for a $d_0 = 1.49$ nm sample, the Stokes and anti-Stokes spectra should both be semiconducting for $E_{\text{laser}} < 1.3$ eV and $E_{\text{laser}} > 2.1$ eV, while for $1.51 < E_{\text{laser}} < 1.87$ eV both the Stokes and anti-Stokes spectra should be dominated by metallic nanotubes, in good agreement with the results of Fig. 5-3. Metallic behavior for the Stokes spectrum and semiconducting behavior for the anti-Stokes spectrum is predicted by Fig. 5-4 at $E_{\text{laser}} = 1.92$ eV, also consistent with the experimental results of Fig. 5-3, as is also the reverse behavior observed for the Stokes and anti-Stokes processes at $E_{\text{laser}} = 1.49$ eV. At each value of E_{laser}, the energy of the scattered beam is at $E_{\text{laser}} - E_{\text{ph}}$ for the Stokes process and at $E_{\text{laser}} + E_{\text{ph}}$ for the anti-Stokes process. Figure 5-4 accounts for the metallic and semiconducting behavior of all traces in Fig. 5-3.

To compare the Stokes and anti-Stokes spectra for semiconducting and metallic nanotubes, we show in Fig. 5-5 lineshape analyses for the tangential band at E_{laser} = 1.49 eV and 1.92 eV. The peak frequencies, FWHM linewidths, and relative intensities of the Lorentzian fits, and additionally the interaction parameter (1/q) for

the Breit–Wigner–Fano lineshapes, are listed in Table 5.1. For semiconducting tubes, the Stokes spectrum at $E_{\text{laser}} = 1.49\,\text{eV}$ shows four peaks, at $1607\,\text{cm}^{-1}$, $1595\,\text{cm}^{-1}$, $1570\,\text{cm}^{-1}$ and $1550\,\text{cm}^{-1}$, consistent with prior results (see Chapter 3). At the same $E_{\text{laser}} = 1.49\,\text{eV}$, the anti-Stokes (metallic) spectrum shows only two components, a broad Lorentzian components at $1581\,\text{cm}^{-1}$ and a Breit–Wigner–Fano lineshape at $1546\,\text{cm}^{-1}$ (with 1/q=-0.24), none of which are present in the Stokes (semiconducting) spectrum (see Table 5.1), consistent with Fig. 5-4. It is interesting that features associated with semiconducting nanotubes are absent from this spectrum. Thus the anti-Stokes metallic band at $E_{\text{laser}} = 1.49\,\text{eV}$ has a narrower overall linewidth than for the Stokes metallic band at 1.92 eV, which is dominated by the Breit–Wigner–Fano lineshape at $1547\,\text{cm}^{-1}$ (characteristic of metallic tubes, as will be discussed in the next section), but also shows Lorentzian oscillators identified with semiconducting nanotubes in resonance with $E_{33}^{S}(d_t)$ at the large d_t end of the nanotube diameter distribution (see Fig. 5-4). Likewise the anti-Stokes (semiconducting) spectrum at $E_{\text{laser}} = 1.92\,\text{eV}$ has a long tail (which could be accounted for by a Breit–Wigner–Fano lineshape [52]) at low ω (below $\sim 1550\,\text{cm}^{-1}$), indicating a significant contribution from metallic $E_{11}^{M}(d_t)$ nanotubes at the low end of the diameter distribution (Fig. 5-4) which are resonant at E_{laser}.

Study of the anti-Stokes spectra (phonon emission) accesses greater contributions from the lower left quadrant of Fig. 5-4, thereby providing more accurate information about lineshapes for metallic and semiconducting tangential bands, because the $E_{ii}(d_t)$ bands in Fig. 5-4 are narrower and more separated in this limit [24, 99]. Since the Stokes and anti-Stokes spectra in Fig. 5-5 taken at 1.49 eV have a common incident E_{laser} value, some explanation is needed for the interpretation of the *Stokes* spectra arising from contributions of resonant *semiconducting* nanotubes and the *anti-Stokes* spectra arising from contributions of resonant *metallic* nanotubes. This interpretation is based on having the incident photons non-resonant with either the metallic, or the semiconducting nanotubes in the SWNT sample (see Fig. 2-10). The special selection of E_{laser} so that the incident photon is essentially non-resonant with any nanotubes, but the scattered photon is strongly resonant with metallic nanotubes

Table 5.1: Peak frequencies (ω) and linewidths (Γ) (in cm^{-1}) of the main components of Stokes (upper) and anti-Stokes (lower) tangential modes in Fig. 5-3 of semiconducting (†) and metallic (*) nanotubes ($d_0 = 1.49\,nm$) for selected values of E_{laser}.

Stokes											
1.49 eV			1.58 eV			1.92 eV			2.19 eV		
ω	Γ	1/q	ω	Γ	1/q	ω	Γ	1/q	ω	Γ	1/q
—	—	—	1545*	56	-0.21	1547*	35	-0.15	—	—	—
1550†	22	—	1552†	18	—	1552†	40	—	1553†	19	—
1570†	13	—	1565†	14	—	1565†	14	—	1569†	14	—
—	—	—	1577*	24	—	1581*	22	—	—	—	—
1595†	16	—	1590†	17	—	1593†	18	—	1592†	15	—
1607†	18	—	1608†	26	—	1610†	40	—	1607†	26	—
anti-Stokes											
1546*	60	-0.24	1546*	61	-0.19	—	—	—	—	—	—
—	—	—	—	—	—	1543†	22	—	1553†	22	—
—	—	—	—	—	—	1560†	20	—	1565†	23	—
1581*	38	—	1575*	38	—	—	—	—	—	—	—
—	—	—	—	—	—	1583†	16	—	1591†	18	—
—	—	—	—	—	—	1595†	30	—	1606†	30	—

in the anti-Stokes process and with semiconducting nanotubes for the Stokes process provides a useful method for determining the resonant Raman lineshapes for semiconducting and metallic nanotubes more accurately. The appearance of anti-Stokes spectra requires population of the first excited phonon state (n_1). The ratio n_1/n_0 where n_0 is the zero phonon ground state for a phonon of energy E_{ph} is $n_1/n_0 = \exp[-E_{ph}/kT]$, so that the intensity ratio of the Stokes to anti-Stokes signals is $I_{AS}/I_S = (\omega + \omega_0)^4/(\omega - \omega_0)^4 \times \exp[-E_{ph}/kT]$, which is commonly used to determine T_s the sample temperature. Here we show that this equation cannot be used for the tangential band to determine T_s in SWNTs when different kinds of nanotubes (semiconducting vs. metallic) are resonant in the anti-Stokes and Stokes spectra at a given E_{laser}. The equation may, however, be used when both Stokes and anti-Stokes Raman spectra come from semiconducting nanotubes, and all the components of the lineshape have the same relative intensity ratios.

Whereas for 2D and 3D sp^2 carbon materials, the Stokes and anti-Stokes tangen-

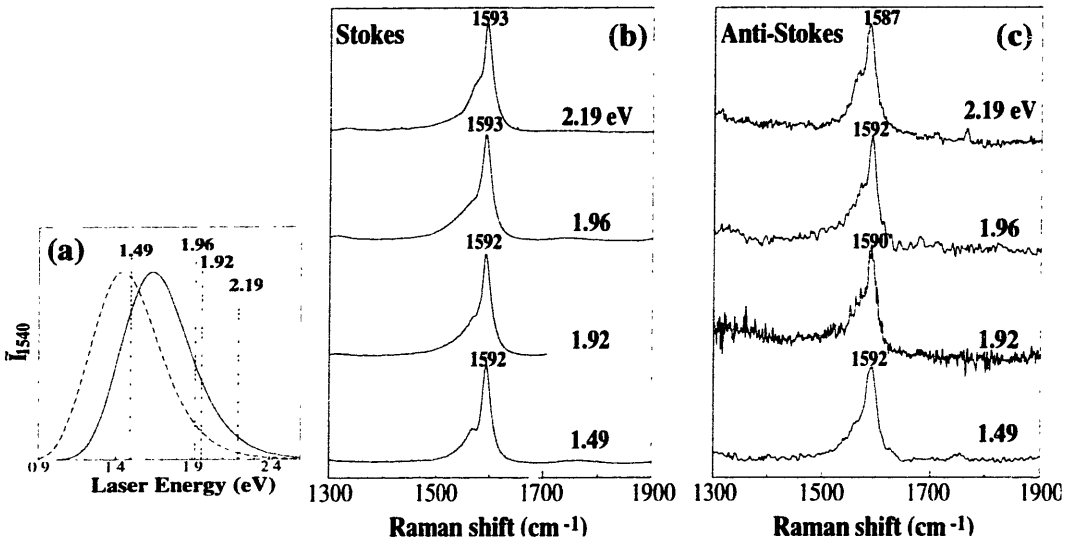

Figure 5-6: (a) A plot of the energy windows where metallic nanotubes are expected to be resonantly enhanced in the anti-Stokes (dashed line) and Stokes (solid line) Raman spectra for the sample of SWNTs with a broad distribution of diameters centered at d_0=1.85 nm (S3). (b) Stokes and (c) anti-Stokes Raman spectra, collected using E_{laser} = 1.49, 1.92, 1.96 and 2.19 eV.

tial bands at a given E_{laser} value are almost identical, the unusual resonant Raman process for carbon nanotubes gives rise to differences in the Stokes and anti-Stokes tangential band spectra when one spectrum is within the window of E_{laser} for metallic nanotubes and the other is not. It should be noted that only samples of with a narrow distribution of small or medium diameter nanotubes ($d_t \leq$1.8 nm) would display this degree of asymmetry, as shown for sample S2 and will be seen for sample S3 in Chapter 7. In Fig. 5-6 (a) is plotted the calculation (using Eq. 5.2) of the energy window for resonant enhancement of the Raman bands of metallic nanotubes in the Stokes and anti-Stokes Raman scattering spectral regions for sample S3 (d_0=1.85 nm). If the diameter distribution of the nanotubes is too broad (as occurs in sample S3), then metallic carbon nanotubes are expected to be in resonance over a wide range of laser excitation energies (see Figure 5-6(a)), and the Stokes and anti-Stokes energy windows are seen to overlap over a wide range of values of laser energy. This should be expected given the center diameter of this sample of SWNTs, since for the laser excitation energies used the Stokes and anti-Stokes spectra would sample the upper right quadrant of Fig. 5-4, where the allowed transition energies are broad and overlapping.

Fig. 5-6 (b) and (c) show the Stokes and anti-Stokes Raman spectra collected from sample S3 (d_0=1.85 nm), collected using several different values of E_{laser}. We see that there is only very modest change in lineshape for the Stokes spectrum (Fig. 5-6 (b)) for the different values of E_{laser}, and in comparing the Stokes and anti-Stokes spectra (panels (b) and (c)) for a given E_{laser} there is also very little difference in lineshape or peak position. The modest changes in lineshape for this sample when metallic nanotubes are resonantly enhanced in the Raman spectra will be discussed in section 5.4 in terms of a curvature dependence for the Raman spectra of metallic nanotubes. As a result of the wide energy window over which the Raman tangential G-band feature for metallic nanotubes is resonantly enhanced for this sample of SWNTs, we see no asymmetry and sample S3 exhibits behavior expected of any other sp^2 or sp^3 carbon.

5.4 Tangential G-band of Metallic Nanotubes

The lineshape of the tangential G-band ($\sim$1600 cm^{-1}) in the Raman spectrum of semiconducting single-walled carbon nanotubes (SWNT) has been extensively studied, and is well accounted for using Lorentzian oscillators [88, 95]. Polarization studies have identified the symmetries of the various components of the lineshape which is used in making lineshape analyses [94]. There is, however, no explanation for the downshift and broadening of the Raman tangential G-band of metallic SWNTs relative to semiconducting SWNTs, and there is still some debate as to whether the Raman lineshape for the metallic SWNTs is best described by a Lorentzian or a Breit–Wigner–Fano (B–W–F) lineshape. The analysis presented here shows that only two Raman components are needed to fit the tangential G-band for metallic SWNTs, with a Lorentzian lineshape for the higher frequency feature and a B–W–F line for the lower frequency feature, and with both components exhibiting predominantly A (A_{1g}) symmetry. The differences in their peak frequencies are attributed to: (1) a difference in force constant for vibrations along the tube axis (higher frequency feature) versus circumferentially (lower frequency feature), and (2) an additional downshifting and broadening of the lower frequency component due to coupling of the discrete

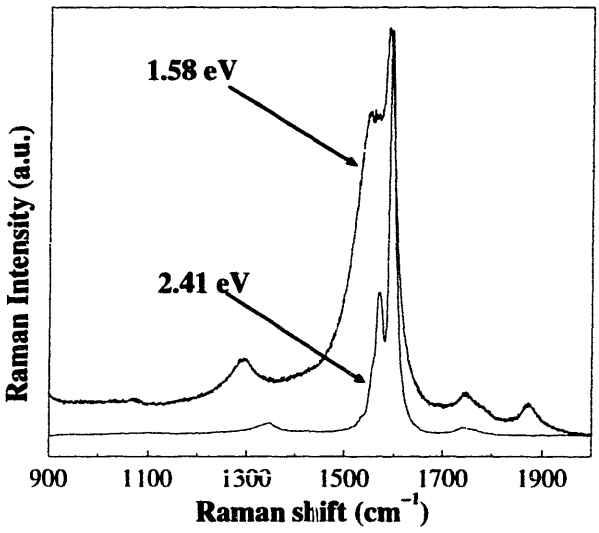

Figure 5-7: Raman spectra in the spectral range from 900 cm^{-1} to 2000 cm^{-1} showing the spectra obtained from sample S2 (d_t = 1.49±0.2 nm) using two different laser excitation energies, 2.41 eV (lower curve) and 1.58 eV (upper curve).

phonon line to a surface-plasmon-based electronic continuum (resulting in the B–W–F lineshape). This coupling does not occur for vibrations along the tube axis. The Breit–Wigner–Fano coupling mechanism will be discussed in more detail in section 7.3.

5.4.1 Breit–Wigner–Fano Lineshape Analysis

The asymmetric Breit–Wigner–Fano (interaction) lineshape described in Chapter 3,

$$I(\nu) = I_o[1 + 2(\nu - \nu_o)/q\Gamma]^2]/[1 + [2(\nu - \nu_o)/\Gamma]^2] \tag{5.3}$$

(where 1/q is a measure of the interaction of the phonon with a continuum of states), has previously been used to fit some of the Raman bands of various sp^2 carbons, such as the ~1540 cm^{-1} feature of metallic SWNTs [5, 51], the tangential G-band feature of alkali-metal doped SWNTs [93], the feature near 1600 cm^{-1} of carbon aerogels [96], and alkali-metal graphite intercalation compounds [34], as well as the ~270 cm^{-1} feature [126] of metallic K_3C_{60}. In contrast, the Raman bands of the *semiconducting* forms (undoped C_{60}, K_6C_{60} [126], and semiconducting SWNTs) ex-

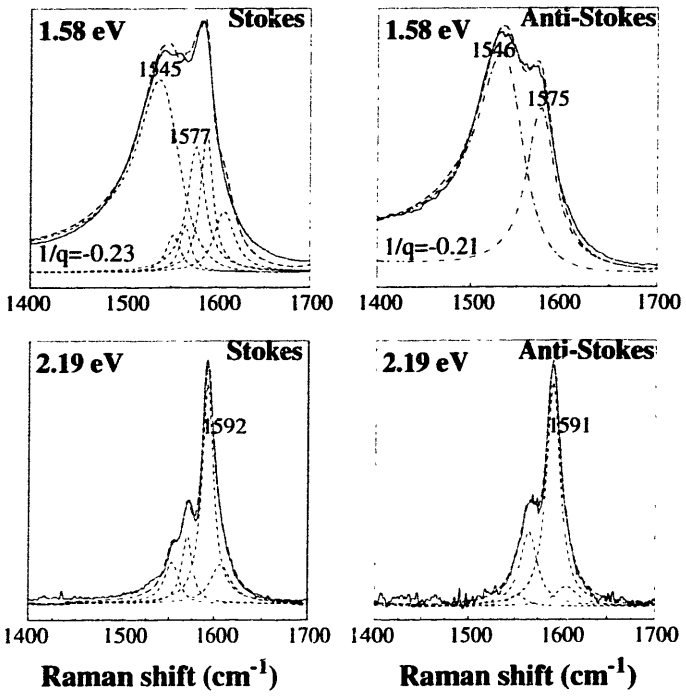

Figure 5-8: Stokes and anti-Stokes Raman spectra for SWNTs of d_t = 1.49±0.2 nm taken at two values of E_{laser}. Fitting parameters are listed in Tables 5.2.

hibit only Lorentzian lineshapes. Figure 5-7 shows the Stokes Raman signal (from 900 cm^{-1} to 2000 cm^{-1}) from sample S2 (d_t=1.49±0.20 nm), for laser excitation energies E_{laser} = 1.58 and 2.41 eV. The lower frequency tail of the broad tangential G-band obtained using E_{laser} = 1.58 eV comes from metallic SWNTs and exhibits a slow decay back to the spectral baseline (suggesting the use of an asymmetric B–W–F lineshape analysis), in contrast to the flat baseline from E_{laser} = 2.41 eV for which the spectrum is associated with semiconducting SWNTs. In this section, I focus on the lineshape analysis of the tangential G-band feature in both the Stokes and anti-Stokes resonant Raman spectra for metallic SWNTs of different diameter distributions, where the important role of the curvature of the SWNT in the coupling process will be described.

Comparison fits to the tangential G-band features (obtained using E_{laser} = 1.58 eV and 2.19 eV) were made to both the Stokes and anti-Stokes spectra of sample S2 (d_t=1.49±0.2 nm), and these fits are shown in Fig. 5-8, using the fitting parameters listed in Table 5.2. Both the Stokes and anti-Stokes Raman spectra obtained for

Table 5.2: Detailed lineshape analysis of the Stokes and anti-Stokes spectra from SWNTs with d_t=1.49±0.2 nm, shown in fig. 5-8. The frequencies (ω) and FWHM (Γ) are shown for the Lorentzian curves, while additionally the (1/q) value is given for the B–W–F curves. The symbols (*) and (†) refer to components associated with metallic and semiconducting SWNTs, respectively.

$\omega(cm^{-1})$	Γ (cm^{-1})	1/q	$\omega(cm^{-1})$	Γ (cm^{-1})	1/q
1.58 eV	**(Stokes)**		2.19 eV	**(Stokes)**	
1545*	56	-0.23	—	—	—
1552†	18	—	1553†	19	—
1565†	14	—	1569†	14	—
1577*	24	—	—	—	—
1590†	17	—	1592†	15	—
1608†	26	—	1607†	26	—
1.58 eV	**(anti-Stokes)**		2.19 eV	**(anti-Stokes)**	
1546*	61	-0.21	—	—	—
—	—	—	1553†	22	—
—	—	—	1565†	23	—
1575*	38	—	—	—	—
—	—	—	1591†	18	—
—	—	—	1606†	30	—

$E_{laser} = 2.19\,eV$ (where only semiconducting nanotubes are resonant in sample S2) show lineshapes that are best fit by four Lorentzian oscillators [94] located at ~1607, 1592, 1569 and $1553\,cm^{-1}$, based on the polarization studies of the lineshape (see Section 4.5) [94], with the anti-Stokes spectra requiring the same Lorentzian oscillator frequencies but larger FWHM (Γ) values. A fit of these spectral features to a B–W–F lineshape yielded only very small values of 1/q (between - 0.04 and - 0.07), indicating that the same set of *Lorentzian* oscillators (with similar relative intensities) are sufficient to fit both the Stokes and anti-Stokes spectra for *semiconducting* SWNTs. In contrast, the anti-Stokes Raman spectrum from $E_{laser} = 1.58\,eV$, which contains resonant contributions from only metallic SWNTs[10], is best fit using a B–W–F lineshape for the $1546\,cm^{-1}$ feature ($1/q = -0.21$) and a Lorentzian line for the $1575\,cm^{-1}$ feature. The Stokes spectrum from $E_{laser} = 1.58\,eV$, requires contributions from both metallic and semiconducting SWNTs[10] to fit the entire tangential G-band (see Table 5.2 and Fig. 5-8). Fits to the tangential G-band for other values of E_{laser}, where metallic SWNTs are resonantly enhanced, gave similar results, with negative values of the interaction parameter ($0.14 \leq |1/q| \leq 0.26$) for the lower frequency feature (1543 - $1546\,cm^{-1}$).

These data indicate that we need only two components to fit the metallic Raman band ($1545\,cm^{-1}$ and $1577\,cm^{-1}$), while Group Theory predicts that there are two modes each of A (A_{1g}), E_1 (E_{1g}) and E_2 (E_{2g}) symmetry in the tangential G-band region of SWNTs [102]. The three different symmetries have distinctly different polarization behaviors. If we consider the light to be propagating along the $\vec{y}$ direction and the nanotube to be oriented along the $\vec{z}$ direction, then A (A_{1g}) modes will appear only in parallel polarizations [(ZZ) and (XX)], while the E_1 (E_{1g}) modes will appear only in cross-polarized measurements [(XZ) and (ZX)]. The E_2 (E_{2g}) modes will also appear in parallel polarizations but only for (XX). The depolarization effect [3] is expected to be strong for metallic SWNTs. This effect occurs for external fields polarized perpendicular to the nanotube axis ($\vec{z}$), where an electric field is induced by the polarization of the nanotubes, resulting in an induced charge density localized on the cylindrical surface, and reduction of the optical absorption perpendicular to

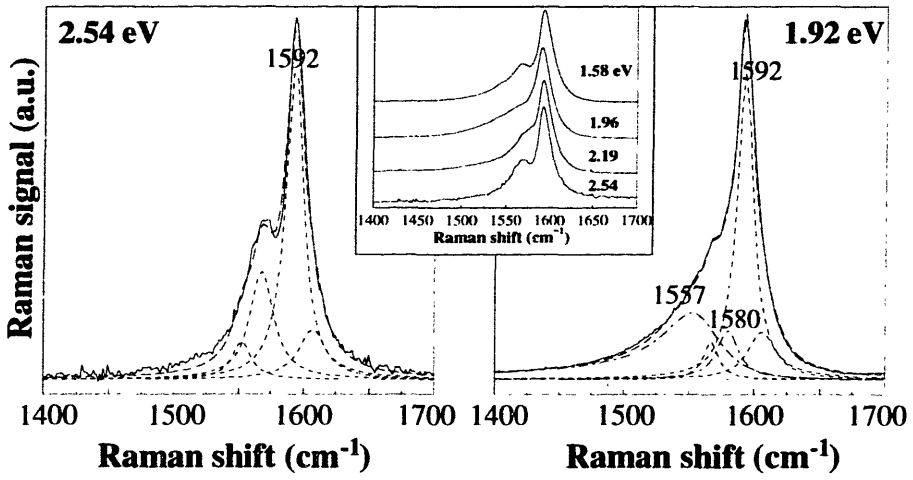

Figure 5-9: Detailed lineshape analysis of the tangential G-band feature in the Stokes spectra from samples of nanotubes with a broad distribution of diameters centered at d_0=1.85 nm, collected using E_{laser} = 1.58 eV and 1.92 eV. The inset shows how the tangential-G-band feature of this sample of SWNTs changes with E_{laser}.

the tube. The preferential absorption of light polarized parallel to the tube axis (by a factor of about 20 compared to perpendicular polarizations) would favor the A (A_{1g}) and E_1 (E_{1g}) modes in the Raman spectra, due to their polarization dependence. Totally symmetric modes are most affected by an RRS process (through a Franck-Condon mechanism) and so the two metallic components are most likely of A (A_{1g}) symmetry. The strong curvature of SWNTs results in differing force constants along the nanotube axis (larger) versus circumferentially (smaller), thus accounting for different mode frequencies for A (A_{1g}) mode displacements along different tangential directions on the carbon nanotube surface. This difference in A (A_{1g}) mode frequencies also occurs for semiconducting SWNTs [94], but there the frequency difference is smaller. The additional downshift of the lower frequency A (A_{1g}) mode for metallic SWNTs comes from the coupling mechanism responsible for the B–W–F lineshape. With this greater downshift and coupling should come broadening (greater FWHM). To test the effect of curvature on the B–W–F lineshape, I also analyzed the tangential G-band spectra for samples of SWNTs with diameters larger (d_0=1.85 nm) and smaller (d_0=1.35 nm) than those of sample S2.

The Stokes tangential G-band of sample S3 (d_0=1.85 nm) exhibits a lineshape basically typical of semiconducting SWNTs for E_{laser} = 2.54 eV (see Fig. 5-9). With

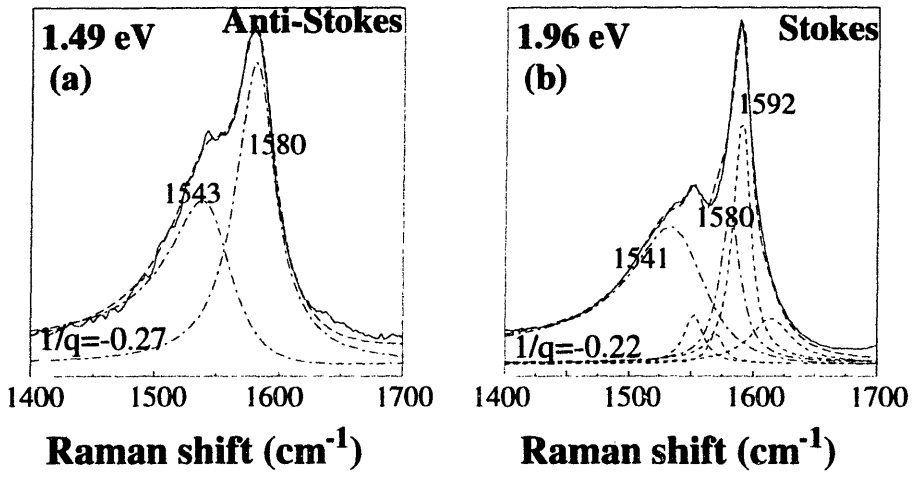

Figure 5-10: Detailed lineshape analysis of the tangential G-band feature from nanotube sample S1 (d_t = 1.35± nm), collected using E_{laser} = 1.49 eV in the anti-Stokes window (exhibiting only G-band components from metallic nanotubes) and E_{laser} = 1.92 eV in the Stokes window (showing components from both metallic and semiconducting SWNTs).

decreasing E_{laser}, a small B–W–F peak at 1557 cm^{-1} develops, with 1/q increasing from - 0.14 to - 0.28 (FWHM $\simeq$ 40 cm^{-1}), as E_{laser} decreases from 2.54 eV to 1.96 eV. At the same time a Lorentzian peak is found at 1580 cm^{-1} (FWHM $\simeq$ 24 cm^{-1}) and this feature persists down to E_{laser} = 1.58 eV with approximately the same frequency and linewidth. The (1/q) value and FWHM linewidth (Γ) vary a lot for this sample of SWNTs for different values of E_{laser}. This is consistent with the large diameter distribution of this sample, where many different diameter metallic nanotubes can contribute to the lower frequency B–W–F feature when they are resonantly enhanced.

Figure 5-10 shows example fits to the tangential G-band feature for (a) the anti-Stokes spectrum using E_{laser} = 1.49 eV and (b) the Stokes spectrum using E_{laser} = 1.96 eV for sample S1 (d_0=1.35 nm). For both the Stokes and anti-Stokes tangential G-band features of sample S1, the Raman peaks from the metallic SWNTs are located at 1580 cm^{-1} (Lorentzian with FWHM $\simeq$ 23 cm^{-1}), while the lower frequency B–W–F component ranges from 1539-1543 cm^{-1} ($0.18 \leq |1/q| \leq 0.27$) and is broader (FWHM $\simeq$ 60-84 cm^{-1}) and slightly downshifted relative to sample S2. On average, the absolute values of the interaction parameter obtained from the fits to this sample

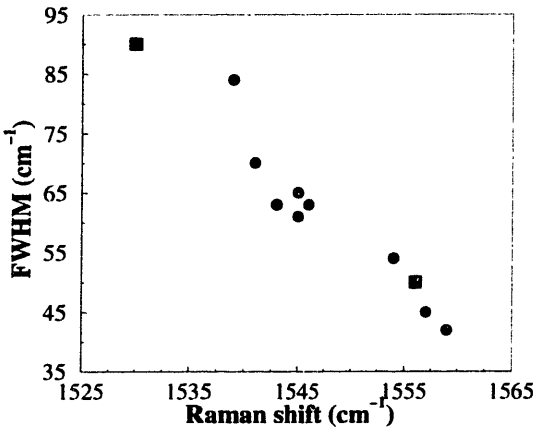

Figure 5-11: The FWHM linewidth (Γ) of the Breit–Wigner–Fano peak plotted vs. the Raman peak frequency for the three samples in this study. The squares data points are values taken from Ref. [51].

(S1) are larger ($\overline{|1/q|} = 0.24$) than those from sample S2 ($\overline{|1/q|} = 0.20$) which contains the larger diameter nanotubes.

Kataura *et al.* [51] showed spectra from SWNTs with a diameter distribution of $0.68\,\mathrm{nm} \leq d_t \leq 1.0\,\mathrm{nm}$, and the lower (B–W–F) component for their sample was located at $1530\,\mathrm{cm}^{-1}$ (FWHM $\simeq 90\,\mathrm{cm}^{-1}$ and 1/q = -0.25). Collecting all these data, the FWHM linewidth (Γ) vs. the Raman peak frequency are plotted in Fig. 5-11, where we see that as the lower frequency B–W–F peak shifts to lower frequency (as the tube diameter d_t decreases), the feature broadens. In section 3.4, we showed that the FWHM linewidth (Γ) of the Breit–Wigner–Fano (B–W–F) lineshape is proportional to the square of the matrix element coupling the discrete phonon line to the continuum, and so a broader B–W–F lineshape would indicate increased coupling. The interaction parameter (1/q), which is proportional to the coupling matrix element, is also larger on average for the B–W–F peak from the smaller diameter nanotubes. Both of these results are consistent with a curvature-induced downshifting of the lower frequency A (A_{1g}) modes, that is accompanied by a broadening due to the coupling responsible for the B–W–F process.

5.5 Conclusions

By introducing the B–W–F lineshape, we have reduced the number of components needed to fit the tangential G-band for metallic nanotubes (now only two versus the six that were used by Pimenta *et al.* [89]) and we gained physical insight into the nature of the electron-phonon coupling of the metallic nanotubes, since (1/q) is a measure of the degree of coupling of the discrete phonon line to a continuum of states, and in the limit that (1/q) goes to zero, the B–W–F lineshape returns to a Lorentzian lineshape.

Our resonant Raman results indicate that the resonance process (electron-phonon coupling) occurs more strongly for metallic nanotubes than for semiconducting nanotubes due to their higher carrier density, as evidenced by the need for the B–W–F (interaction) lineshape to account for one of the components of the band, while only Lorentzian oscillators are necessary to describe the narrow semiconducting lineshape. The B–W–F component shifts to larger frequencies and narrows for larger diameter nanotubes, because the finite density of states at the Fermi level is smaller for larger diameter nanotubes, and so there are fewer carriers to participate in the coupling.

Totally symmetric modes couple most effectively to electronic excitations through a Franck-Condon mechanism, and are most affected by a resonance Raman experiment, and thus the behavior of the lower frequency metallic G-band ($\sim$1540 cm^{-1}) feature is consistent with predominantly A (A_{1g}) symmetry. On the basis of these data, we are unable to identify the nature of the continuum that produces the Breit–Wigner–Fano lineshape. However, this question will be re-examined in connection with the results of the Surface-enhanced Raman spectroscopy (SERS) experiments, to be discussed in Chapter 7, which provide important insights into the B–W–F coupling mechanism. In the next Chapter we will report results for resonant Raman spectroscopy involving the second-order spectrum, which shows unusual resonant behavior due to the 1D nature of the electronic density of states of the carbon nanotubes, and also gives evidence for greater electron-phonon coupling of the metallic nanotubes.

Chapter 6

Second Order Raman spectra

6.1 Introduction

The second-order Raman spectra of single-wall carbon nanotubes are unique relative to other crystalline systems in exhibiting features associated with resonant enhancement phenomena arising from the unique one-dimensional (1D) density of electronic states for carbon nanotubes. These second-order spectra are therefore selective of specific carbon nanotubes, just as occurs for the first-order spectra (Chapter 4) [27, 89, 95]. In this chapter I focus on the unique behavior of overtones and combination modes in the second-order Stokes Raman spectra associated with the dominant features in the first-order spectra, which exhibit strong resonant coupling to the 1D density of electronic states. I also discuss other features in the second-order Stokes Raman spectra, such as the D-band and the G'-band features, not associated with the 1D resonant Raman scattering process. I will then discuss the asymmetry which also occurs for the combination modes and the D- and G'-bands between the second-order Stokes and anti-Stokes Raman spectra of the carbon nanotubes.

Since the energy separations $E_{ii}(d_t)$ in Figs. 2-9 and 2-10 are strongly dependent on the diameter d_t of the nanotubes, a change in the energy of the incident laser beam E_{laser} results in the resonant Raman excitation of *different* nanotubes. Furthermore $\hbar\omega_{\text{phonon}}$ can be as large as 0.4 eV for second-order scattering processes for the tangential modes. Therefore, the specific nanotubes in a given sample that are excited

in the first-order Raman scattering process are very likely to be different from the nanotubes that participate in the second-order scattering process. I also demonstrate the importance of the scattered photon in the second-order Raman spectra. Since the scattered photon propagates in all directions, it is expected to couple resonantly to more of the randomly-oriented carbon nanotubes than the incident photon, which couples most strongly to nanotubes whose axes are aligned along the optical electric field of the incident beam. Thus the probability of an optical resonance with the scattered beam is expected to be higher than for the incident beam.

6.2 Experimental Details

This study focuses on the second-order Raman spectra of sample S2 (1.49 ± 0.20 nm). Raman spectroscopy experiments were performed under ambient conditions in a backscattering configuration using several laser excitation lines. These lines include the argon lines at 457.9 nm (2.71 eV), 488 nm (2.54 eV) and 514.5 nm (2.41 eV); the krypton lines at 568.2 nm (2.19 eV), 647.1 nm (1.92 eV) and 676.4 nm (1.83 eV); the He-Ne line at 632.8 nm (1.96 eV); and a diode laser at 785 nm (1.58 eV). The spectral resolution of the different Raman systems for phonons was better than $2\,\mathrm{cm}^{-1}$. A Ti:sapphire laser at 830 nm (1.49 eV) was also used, where the spectral resolution for this system was $\sim 8\,\mathrm{cm}^{-1}$.

6.3 Second-order Raman spectra

Figure 6-1 shows the first-order and second-order features in the Raman spectra for the single-wall carbon nanotubes over a broad range of phonon frequencies for three laser excitation energies E_{laser}. The two dominant features in the first-order Raman spectra for single-wall carbon nanotubes (see Fig. 6-1) are the radial breathing modes (located in the 150–200 cm^{-1} range) and the tangential modes (located in the 1530–1610 cm^{-1} range). Both of these features in the first-order Raman spectra are resonantly enhanced when the laser excitation energy (E_{laser}) is equal to the energy

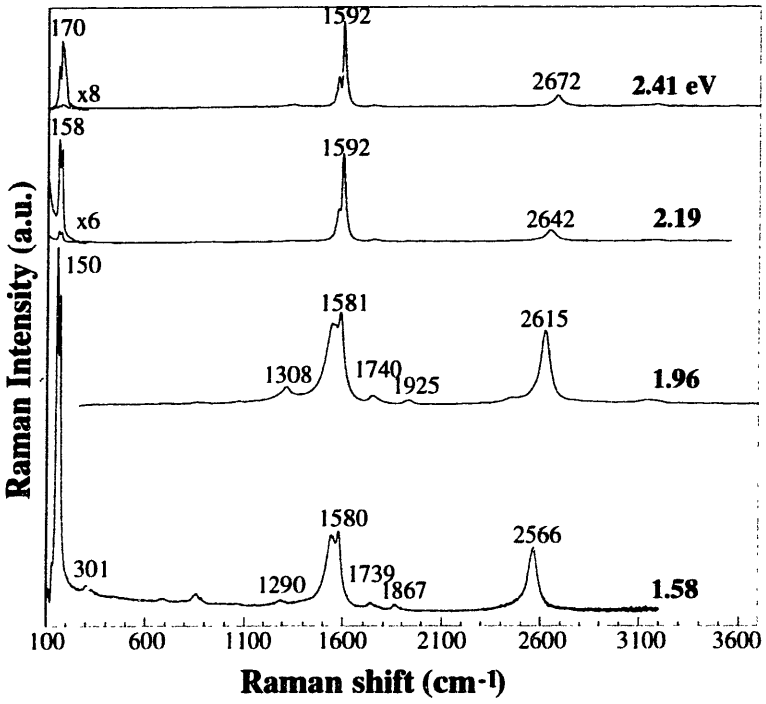

Figure 6-1: First and second-order Raman spectra for carbon nanotubes with d_t = 1.49 ± 0.20 mn over the broad phonon frequency range 100–3700 cm^{-1} for E_{laser} = 1.58, 1.96, 2.19, and 2.41 eV. The radial breathing mode feature for $E_{\text{laser}} = 2.19$ and 2.41 eV has been magnified.

separation between a singularity in the 1D electron density of states in the valence and conduction bands, such as the E_{ii} energy separations (between the ith conduction band singularity and the ith valence band singularity), $E_{ii} = E_{11}, E_{22}, \ldots$, shown in Figs. 2-9 and 4-6. Resonant enhancement occurs not only for the incident photon but also for the scattered photon, so that the conditions for resonant Raman scattering include $E_{\text{laser}} = E_{ii}$ and $E_{\text{laser}} = E_{ii} + \hbar\omega_{\text{phonon}}$ for the Stokes process. The window for resonance Raman scattering for the incident and scattered light is shown in Fig. 4-6 for the $d_t = 1.49 \pm 0.20$ nm diameter nanotube sample (S2). Since the relative intensities of the various features in Fig. 6-1 are dependent on the laser excitation energy, resonant Raman effects are as important in the analysis of the second-order spectra, as they are for interpreting the first-order spectra. I discuss below the various features in the second-order spectrum associated with the harmonics (overtones) and combination modes of the two dominant features of the first-order spectrum.

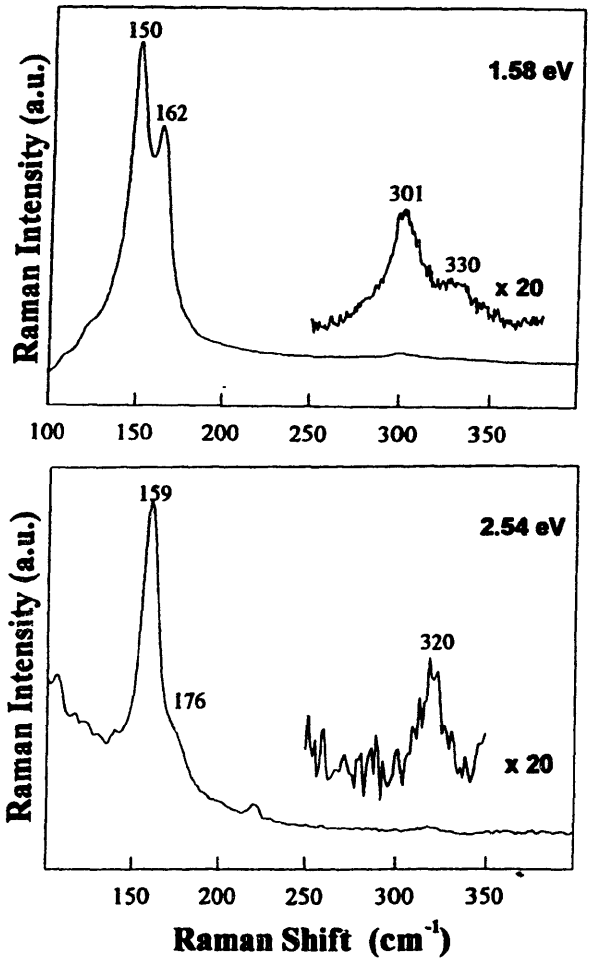

Figure 6-2: The Raman spectra for the radial breathing mode band and its second-harmonic at two laser excitation energies 1.58 eV (785 nm) and 2.54 eV (488 nm).

6.3.1 Overtones

In Fig. 6-2, we see spectral features identified with the second harmonic (overtone) of the radial breathing mode $2\omega_{\mathrm{RBM}}$ at two different laser excitation energies. For example, at $E_{\mathrm{laser}} = 1.58\,\mathrm{eV}$ (785 nm), the first-order spectrum gives resonantly enhanced radial breathing modes at $150\,\mathrm{cm}^{-1}$ and $162\,\mathrm{cm}^{-1}$, with linewidths (FWHM) of $14\,\mathrm{cm}^{-1}$ and $11\,\mathrm{cm}^{-1}$, respectively, to be compared with the second-order lines which occur at $301\,\mathrm{cm}^{-1}$ and $330\,\mathrm{cm}^{-1}$ and have relatively narrow linewidths ($21\,\mathrm{cm}^{-1}$). A change in E_{laser} excites different nanotubes, so that for $E_{\mathrm{laser}} = 2.54\,\mathrm{eV}$ (488 nm), the first-order Raman spectrum shows a radial breathing mode at $159\,\mathrm{cm}^{-1}$ and a small shoulder at $176\,\mathrm{cm}^{-1}$. The second harmonic of this first-order band shows a weak

Table 6.1: Summary of the peak frequencies and linewidths (in cm^{-1}) of the Lorentzian components for the radial breathing modes (ω_{RBM}) and their overtones ($2\omega_{RBM}$) for the indicated E_{laser} values (see Fig. 6-2).

	ω_{RBM}							
E_{laser}	1.58 eV		2.19 eV		2.41 eV		2.54 eV	
Line	ω	Γ	ω	Γ	ω	Γ	ω	Γ
#1	—	—	—	—	142	10	—	—
#2	150	14	—	—	155	10	—	—
#3	162	11	158	10	—	—	159	11
#4	—	—	171	10	170	10	—	—
#5	—	—	—	—	178	10	176	9
#6	—	—	—	—	188	10	—	—
	$2\omega_{RBM}$							
#1	301	20	—	—	—	—	—	—
#2	—	—	311	30	—	—	—	—
#3	—	—	—	—	—	—	320	15
#4	330	20	—	—	—	—	—	—

second-order feature at 320 cm^{-1} (see Fig. 6-2). Similar trends are observed at other values of E_{laser}, and a summary of our observations of the overtones of the radial breathing mode is given in Table 6.1.

The energy of the radial breathing mode feature is about 0.02 eV, on the order of the width of the van Hove singularities ($\Gamma_e = 0.04 \pm 0.02$ eV from section 4.5) in the electronic density of states. From Figs. 5-4 we see that, for $E_{laser} = 1.58$ eV, the incident photon is in resonance with metallic carbon nanotubes, while for $E_{laser} = 2.41$ eV, the incident photon is in resonance with semiconducting nanotubes. From section 3.3.3 we see that, for the A-term resonant Raman scattering process from totally symmetric modes, greater amount of electron-phonon coupling would result in higher intensity of the overtones. The overtone of the radial breathing mode, which in Chapter 2 was shown to possess $A\,(A_{1g})$ symmetry, is very well resolved for E_{laser} values where contributions from metallic nanotubes dominate the spectra for the tangential band (see Figs. 6-1 and 6-3).

In contrast, the second harmonic of the tangential G-band $2\omega_{tang}$ which occurs in the range 3100–3250 cm^{-1} (see Fig. 6-4) has very different characteristics from the

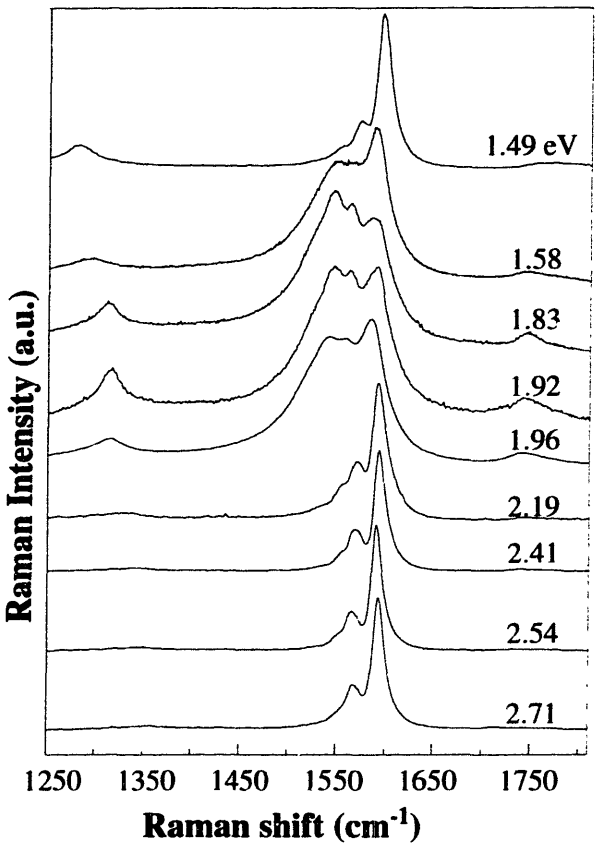

Figure 6-3: First-order Raman spectra for the tangential mode (1500–1650 cm^{-1}) taken for nine laser excitation energies. At lower frequencies (1300–1350 cm^{-1}) the D-band feature is observed, and at higher frequencies near 1740 cm^{-1} a combination mode is seen for some values of E_{laser}, both of which have higher intensities relative to the tangential G-band when the Raman bands from metallic nanotubes are resonantly enhanced.

second harmonic of the radial breathing mode $2\omega_{RBM}$ shown in Fig. 6-2. We see in Fig. 6-4 the evolution with E_{laser} of the second harmonic of the tangential band for five laser energies in the range 1.96–2.71 eV. The central frequency and linewidth of this second-order band is relatively weakly dependent on E_{laser} for $2.19 < E_{laser} \leq 2.71$ eV, where the semiconducting nanotubes dominate the first-order spectra for this sample.

However, for $E_{laser} = 1.96$ eV, where the dominant contribution to the first-order spectrum in Fig. 6-3 comes from metallic nanotubes, the second-order spectrum is downshifted and much broader than for the higher E_{laser} values, consistent with the behavior of the first-order tangential band shown in Fig. 6-3. It is interesting to note

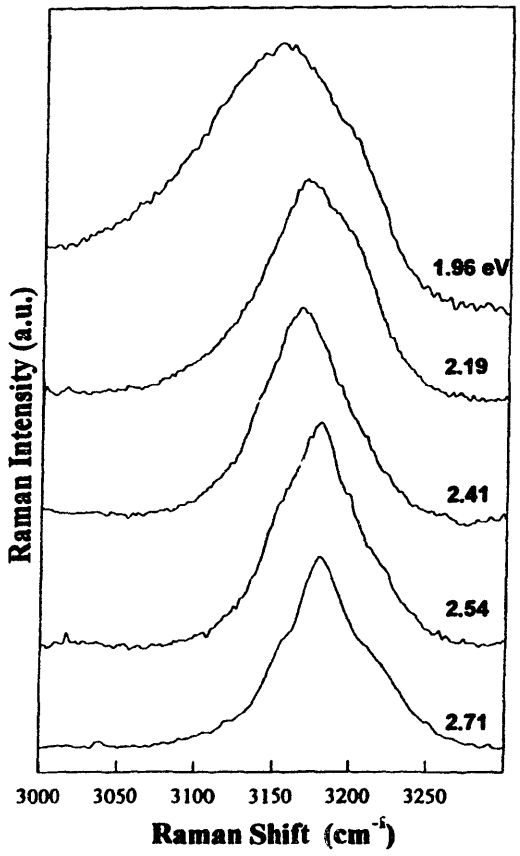

Figure 6-4: Raman spectra for the second harmonic of the tangential mode, collected at five laser excitation energies. The corresponding first-order spectra are displayed in Fig. 6-3.

Table 6.2: A summary of the peak frequencies and linewidths (in cm^{-1}) of the main components of the tangential modes (ω_{tang}) (see Fig. 6-3) and their overtones ($2\omega_{tang}$) (see Fig. 6-4) of the single-wall carbon nanotubes, for selected values of E_{laser}. The symbols (*) and (†) refer to Raman bands attributed to metallic and semiconducting nanotubes, respectively, in the first-order spectrum.

	ω_{tang}								
E_{laser}	1.96 eV			2.19 eV		2.41 eV		2.71 eV	
Line	ω	Γ	1/q	ω	Γ	ω	Γ	ω	Γ
#1	1542*	65	-0.15	—	—	—	—	—	—
#2	1552†	18	—	1553†	19	1554†	18	1552†	22
#3	1565†	14	—	1569†	14	1568†	14	1568†	14
#4	1581*	22	—	—	—	—	—	—	--
#5	1592†	16	—	1592†	15	1594†	13	1593†	14
#6	1610†	40	—	1607†	26	1606†	26	1608†	26
	$2\omega_{tang}$								
#1	3083	71	—	—	--	—	—	—	—
#2	3123	55	—	3119	55	—	—	—	—
#3	3153	42	—	3150	49	3141	32	3153	31
#4	3178	35	—	3172	45	3166	47	3180	38
#5	3203	31	—	3201	38	3195	54	3215	46

that D-band feature located at 1300–1350 cm^{-1} and the small feature near 1750 cm^{-1} have higher intensities relative to the tangential G-band when the broad Raman bands attributed to metallic nanotubes are resonantly enhanced.

The feature in the second-order Raman spectrum for graphite near 3240 cm^{-1} is strongly affected by the mode frequency dispersion of the phonon dispersion curves [31, 35]. This mode frequency dispersion in graphite gives rise to a peak in the phonon density of states near 1620 cm^{-1}, associated with non-zone center phonons. This peak in the phonon density of states is responsible for the feature in the second-order spectrum of graphite near 3240 cm^{-1}. This frequency is upshifted by 76 cm^{-1} from twice the zone-center phonon mode in graphite at 1582 cm^{-1}. Since there is no corresponding peak in the density of states away from the Brillouin zone center in carbon nanotubes, we expect the mode frequency of the second-order tangential band to be close to twice that for the first-order tangential band, consistent with experiment.

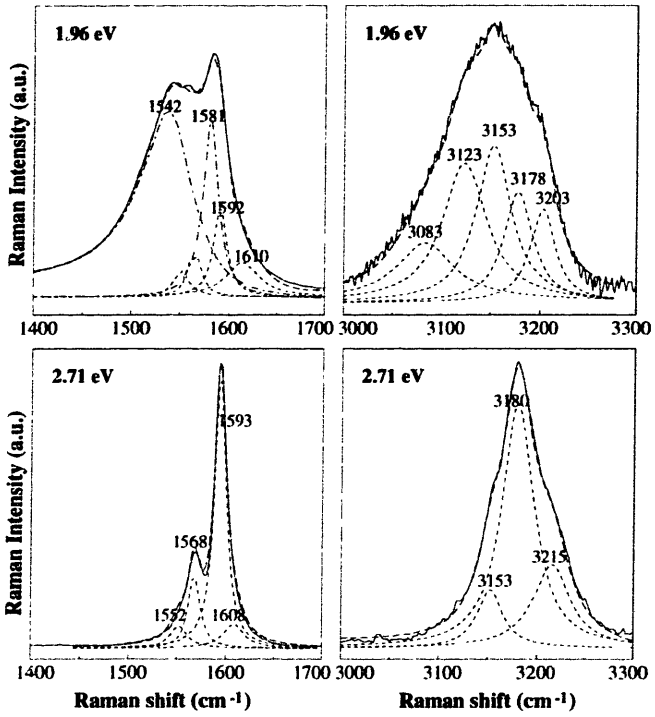

Figure 6-5: A line shape analysis of the spectral features in the first-order spectra (left) and in the second-order spectra (right) for the tangential bands taken for $E_{\text{laser}} =$ 1.96 eV (632.8 nm) and 2.71 eV (457.9 nm).

Even though the tangential band for carbon nanotubes contains modes with different symmetry types, the second harmonic of any irreducible representation always contains the completely symmetric irreducible representation A_g in the direct product of $\Gamma_i \otimes \Gamma_i$. Thus second harmonics of modes that are not Raman-active in the first-order spectrum could become Raman-active in the second-order spectrum through this direct product argument. However, the intensity of such new modes in the second-order spectra is expected to be low. Our resolution was not good enough to see this effect, largely because of the large linewidths of second-order features.

A Lorentzian lineshape analysis of the second-order spectrum associated with the second harmonic of the tangential band has been carried out for the spectra shown in Fig. 6-4, and the results are presented in Table 6.2. Two examples of this lineshape analysis are shown in Fig. 6-5. Here we present the lineshape analysis for the first-order and second-order features taken for E_{laser} at 2.71 eV where the semiconducting nanotubes mainly contribute, and at 1.96 eV where the metallic

nanotubes mainly contribute [89]. The dominant feature in the 2.71 eV second-order spectrum at 3181 cm^{-1} is close to twice the frequency of the dominant mode in the first-order spectrum $2(1592) = 3184\,cm^{-1}$, and the second-order feature is only slightly broader than twice the FWHM linewidth of the first-order feature. The frequencies of the two weaker features in the second-order spectrum at 2.71 eV correspond approximately to twice the frequencies of the first–order features: $3153\,cm^{-1} = 2(1568)$ and $3215\,cm^{-1} = 2(1608)$, although the feature at $3153\,cm^{-1}$ could also be accounted for by the combination $3153\,cm^{-1} = (1592+1568)$. It is interesting to note that the $3215\,cm^{-1}$ component [$2(1608) = 3216\,cm^{-1}$] is the double of the first-order tangential G-band feature (shown to possess E_2 (E_{2g}) symmetry), which comes from high chiral angle semiconducting nanotubes which show the least amount of trigonal warping (see Figs. 2-9 and 2-11), and should thus have higher optical absorption between the sharp van Hove singularities in the electronic density of states than their low chiral angle counterparts. As E_{laser} decreases from 2.71 eV, the peak frequency of the entire second-order band (see Fig. 6-4) downshifts, especially for the lowest value of E_{laser}, because new tangential peaks associated with metallic nanotubes are resonantly enhanced. For example, the second-order peaks in the 2.19 eV and 2.41 eV spectra are at 3171 cm^{-1} and 3166 cm^{-1} (see Table 6.2), both downshifted relative to $2 \times 1592 = 3184\,cm^{-1}$. The second-order spectrum at $E_{laser} = 1.96$ eV in Fig. 6-4 shows a broad, asymmetric band with more scattering intensity at low phonon frequencies. Analysis of the lineshape of this Raman band in Fig. 6-5 shows a feature at $3082\,cm^{-1}$, which is close to $2 \times 1540\,cm^{-1}$, thereby providing support for the interpretation that metallic nanotubes are contributing to this second-order Raman band at $E_{laser} = 1.96$ eV.

Shown in Fig. 6-6 is an increase in linewidth, measured as the full width at half maximum intensity, of the entire second-order band with decreasing E_{laser}. In this figure, the increase in linewidth for the entire second-order band is compared with that for the first-order band as a function of E_{laser}. The large linewidth below ~2.0 eV in the first-order spectra in Fig. 6-6(a) is associated with the large contribution to the spectral intensity from metallic nanotubes (see Fig. 6-3) [89]. We note in Fig. 6-6(b) that the onset of the broadening of the second-order features extends to much higher

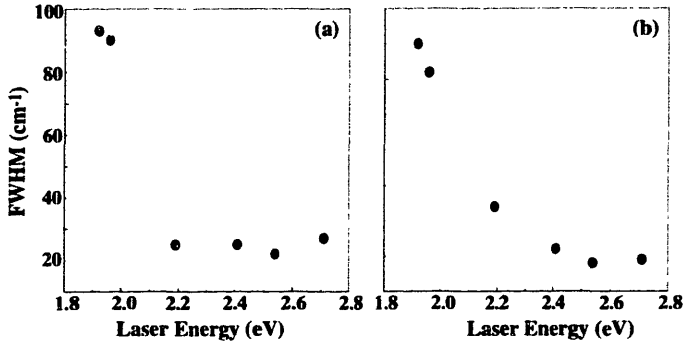

Figure 6-6: Linewidth (FWHM) as a function of E_{laser} (a) for the entire first-order tangential G-band and (b) for the corresponding entire second harmonic of the tangential G-band.

values of E_{laser}, so that at $E_{\text{laser}} = 2.2\,\text{eV}$ (where the scattered photons are still within the metallic window for the second-order spectrum) the linewidth is $\sim 17\,\text{cm}^{-1}$ broader than at $E_{\text{laser}} = 2.71\,\text{eV}$.

The resonant enhancement in the phonon modes for metallic nanotubes occurs when the energy of either the incident or the scattered photon is in resonance with the first electronic transition E_{11}^{M} for the metallic nanotubes in the sample (see Figs. 2-9, 2-10 and 6-3). When $E_{\text{laser}} = 1.92\,\text{eV}$ and $1.96\,\text{eV}$, both the incident and scattered photons are in the resonance window for metallic nanotubes, so that the overtone band is expected to broaden considerably, and this is observed experimentally in Fig. 6-6(b). For $2.19\,\text{eV} \leq E_{\text{laser}} \leq 2.41\,\text{eV}$, even though the incident photon is higher than the resonance energy window E_{laser} for metallic nanotubes in the first-order spectrum (see Fig. 6-3), the energy of the scattered photon falls within the interval of resonant enhancement for metallic nanotubes, because the phonon frequency of $3200\,\text{cm}^{-1}$ in the Stokes process corresponds to a large energy upshift ($\sim 0.4\,\text{eV}$). This is evident by a broadening (Fig. 6-6(b)) and a downshift of the $3200\,\text{cm}^{-1}$ band for $E_{\text{laser}} = 2.19\,\text{eV}$ and $2.41\,\text{eV}$ (see Fig. 6-4 and Table 6.2). Because of the large value for $\hbar\omega_{\text{phonon}}$, the specific nanotubes contributing to the first-order spectrum may be different from the nanotubes contributing to the second-order spectra at $E_{\text{laser}} = 2.19\,\text{eV}$ and $2.41\,\text{eV}$.

6.3.2 Combination Modes

Resonant Raman effects associated with the 1D electron density of states singularities also give rise to resonant effects in the combination modes. One clear example of a combination mode occurs at the sum frequency between a tangential and a radial breathing mode $\omega_{\text{tang}} + \omega_{\text{RBM}}$, as shown in the spectra in Fig. 6-7 taken at $E_{\text{laser}} = 1.58\,\text{eV}$, 1.96 eV, 2.14 eV and 2.71 eV. Since the radial breathing mode ω_{RBM} spectra at $E_{\text{laser}} = 1.58\,\text{eV}$ consist of two lines at $150\,\text{cm}^{-1}$ and $162\,\text{cm}^{-1}$ (see Fig. 6-2), then using the most intense line at $1591\,\text{cm}^{-1}$ for the tangential band ω_{tang} yields a sum of $1741\,\text{cm}^{-1}$ and $1753\,\text{cm}^{-1}$, in good agreement with the dominant peak at $1742\,\text{cm}^{-1}$ and in fair agreement with the weak feature at $1761\,\text{cm}^{-1}$, obtained from a lineshape analysis of the combination mode feature shown in Fig. 6-7.

In Table 6.3 the mode frequencies and linewidths of the combination modes for the $1740\,\text{cm}^{-1}$ band associated with the combination mode $\omega_{\text{tang}} + \omega_{\text{RBM}}$ are listed. The relative intensities of this combination mode at various values of E_{laser} are displayed in Fig. 6-3 where it is seen that this feature is most prominent near $\sim$1.8 eV where the metallic tube contribution is dominant for single wall nanotubes for which $d_t \sim 1.49\,\text{nm}$. Since the tangential mode frequency ω_{tang} is expected to be almost independent of E_{laser}, while the radial breathing mode frequency varies as $\omega_{\text{RBM}} \propto 1/d_t$, the shifts in the peaks of the $1740\,\text{cm}^{-1}$ band for various E_{laser} lines are expected to reflect the variation in ω_{RBM} as E_{laser} is varied, since different nanotubes are resonantly excited at each value of E_{laser}. Since $\hbar\omega_{\text{phonon}} \sim 0.2\,\text{eV}$ for this combination mode, it is also possible that, at a given value of E_{laser}, different nanotubes within the sample are resonantly enhanced in the first-order spectrum as compared with the second-order spectrum.

The spectra in Fig. 6-7 show that the feature, which we tentatively assign to the combination mode $\omega_{\text{tang}} + \omega_{\text{RBM}}$, has a similar peak position and linewidth for $E_{\text{laser}} = 1.58\,\text{eV}$ and 1.96 eV in the metallic regime. We note that the linewidth of this mode increases with increasing E_{laser} above 2.4 eV. The broad line observed for $E_{\text{laser}} = 2.41\,\text{eV}$ could in part be attributed to the excitation of many nanotubes for

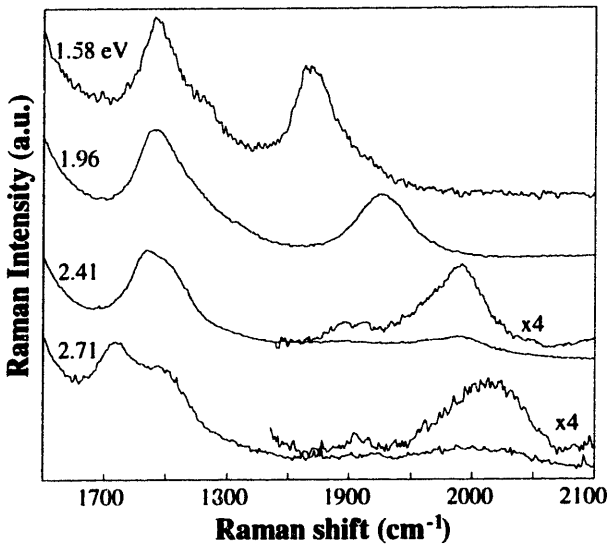

Figure 6-7: Spectral features tentatively associated with combination bands for $\omega_{\text{tang}} + \omega_{\text{RBM}}$ and $\omega_{\text{tang}} + 2\omega_{\text{RBM}}$ in the second-order Raman spectra of carbon nanotubes at $E_{\text{laser}} = 1.58\,\text{eV}$ (785 nm), 1.96 eV (632.8 nm), 2.41 eV (514.5 nm) and 2.71 eV (457.9 nm).

Table 6.3: Summary of the peak frequencies and linewidths (in cm^{-1}) of the Lorentzian components for the combination modes tentatively identified with $\omega_{\text{tang}} + \omega_{\text{RBM}}$ and $\omega_{\text{tang}} + 2\omega_{\text{RBM}}$ for the combination bands in the range 1700–2000 cm^{-1} near 1900 cm^{-1} in Fig. 6-8 for five values of E_{laser}.

	$\omega_{\text{tang}} + \omega_{\text{RBM}}$									
E_{laser}	1.58 eV		1.96 eV		2.41 eV		2.54 eV		2.71 eV	
Line	ω	Γ	ω	Γ	ω	Γ	ω	Γ	ω	Γ
#1	1737	32	1740	31	1733	30	1722	46	1710	39
#2	1762	50	1761	57	1756	34	1753	45	1750	37
	$\omega_{\text{tang}} + 2\omega_{\text{RBM}}$									
#1	1871	31	1925	47	1990	52	2000	60	2011	62

this value of E_{laser}, as suggested by the radial breathing mode spectrum at 2.41 eV (see Table 6.1). However, the Raman spectra taken at 2.54 eV (not shown) and at 2.71 eV (see Fig. 6-7) show further broadening of this combination mode, a decrease in mode intensity, and the development of a doublet structure. For $E_{\text{laser}} = 2.54\,\text{eV}$, there are relatively few radial breathing mode peaks in the first-order spectrum. The analysis in Table 6.3 shows that the frequency of the two components of the $\omega_{\text{tang}} + \omega_{\text{RBM}}$ feature both downshift as E_{laser} increases, though the downshift is larger for the lower frequency component than it is for the upper frequency component. At this time, we have no good explanation for the mode splitting or for the downshifts in the mode frequencies of the $\omega_{\text{tang}} + \omega_{\text{RBM}}$ feature for $E_{\text{laser}} \geq 2.41\,\text{eV}$. It should, however, be noted that a combination of ω_{RBM}=160 cm^{-1} and ω_{tang} 1590 cm^{-1} would account for this feature. Kasuya *et al.* [48] have surmised that this 1740^{-1} feature could be due to phonon-plasmon coupling since it is so pronounced for laser excitation energies in the metallic resonance window (see Fig. 6-3). We find that our present set of experimental results cannot settle this debate, and this issue should be addressed in the future.

In Fig. 6-7 we see another feature at higher frequencies which we tentatively assign to a second combination band, this one associated with $\omega_{\text{tang}} + 2\omega_{\text{RBM}}$. As shown in Fig. 6-7, this feature has a curious dependence on E_{laser}. While the combination band is located near 1870 cm^{-1} for $E_{\text{laser}} \sim 1.58\,\text{eV}$ (785 nm), the feature upshifts to $\sim$1925 cm^{-1} for $1.83 < E_{\text{laser}} < 2.19\,\text{eV}$, and then upshifts again to $\sim$2000 cm^{-1} for $2.41 < E_{\text{laser}} < 2.71\,\text{eV}$ (see Fig. 6-7 and Table 6.1). If we assume $\omega_{\text{tang}} = 1590\,\text{cm}^{-1}$ and $\omega_{\text{RBM}} = 165\,\text{cm}^{-1}$, then we get $\omega_{\text{tang}} + 2\omega_{\text{RBM}} = 1920\,\text{cm}^{-1}$, which accounts for the frequency of the observed features for $1.83 \leq E_{\text{laser}} < 2.19\,\text{eV}$. Weak features in the range 1900–1920 cm^{-1} can be observed also in the spectra at 2.41 eV and 2.71 eV (see also Fig. 6-11). If we now assume that mostly metallic nanotubes dominate the spectrum for $E_{\text{laser}} = 1.58\,\text{eV}$, then $\omega_{\text{tang}} = 1540\,\text{cm}^{-1}$ becomes a dominant feature in the first-order spectrum (see Fig. 6-5), leading to $\omega_{\text{tang}} + 2\omega_{\text{RBM}} = 1870\,\text{cm}^{-1}$, which accounts nicely for the observations at $E_{\text{laser}} = 1.58\,\text{eV}$. For $E_{\text{laser}} > 2.4\,\text{eV}$ where the intensity of this spectral feature becomes low, a new feature in the frequency range 1990–2010 cm^{-1} appears, as shown in Fig. 6-7. We have no further explanation for

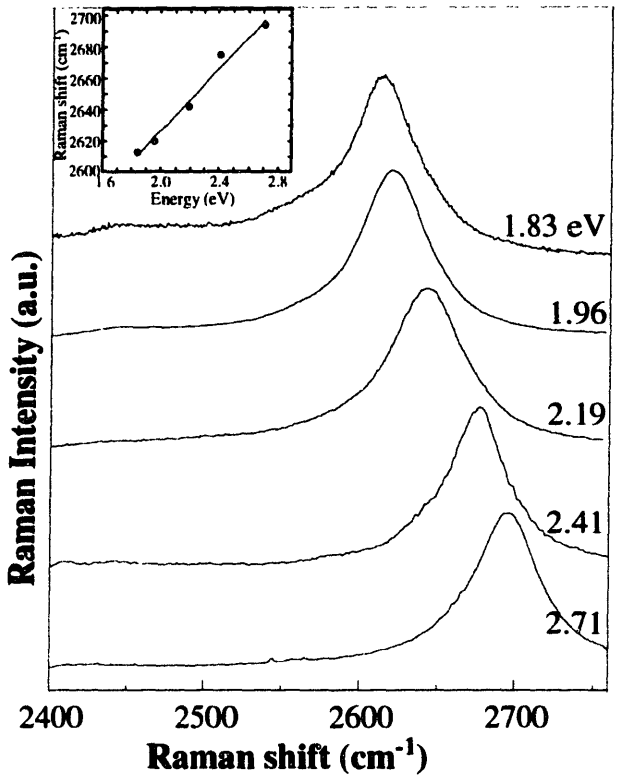

Figure 6-8: The Raman spectra for the intense G' band for five values of E_{laser}. The inset shows a plot of the peak Raman frequency for the G' band features vs laser excitation energy E_{laser}.

the dispersive effect which occurs for this feature with increasing E_{laser} above 2.41 eV.

6.3.3 2D Resonance Phenomena

The most intense feature in the second-order spectrum (see Fig. 6-1) is the peak located at $\sim$2680 cm^{-1} (twice the frequency of the D-band, as discussed in section 4.6) and this feature has an especially strong intensity near $E_{\text{laser}} = 1.96$ eV. This feature, which is closely related to the G' feature in sp^2 carbons, shows a strong upshift in frequency as E_{laser} increases (see Fig. 6-8), which is more explicitly demonstrated in the plot of the peak frequencies vs E_{laser} given in the inset to Fig. 6-8. The slope of the dispersion of G'-band versus E_{laser} is 99 cm^{-1}/eV, which is approximately twice the value of the slope found for the dispersion of the D-band feature (57 cm^{-1}/eV), as shown in Fig. 4-11. Recent published work has actually set the slope of the G' band dispersion at a higher value of 106 cm^{-1}/eV [87], which is closer to 2 $\times$ 57 cm^{-1}/eV.

Since both features arise from a similar process, where the D-band involves only one phonon about the K-point while the G'-band involves two, then this relationship in the slope of their dispersions with E_{laser} should be expected. The large dispersion for sp^2 carbons is explained by resonance with electronic interband transitions near the K-point in the 2D Brillouin zone, but for carbon nanotubes we have only a few allowed wave-vectors in the circumferential direction of the nanotube.

The second-order G'-band in the Raman spectra of various sp^2 carbon materials is generally much more intense than the disorder-induced D-band. This is due to the fact that the second-order G'-band is symmetry-allowed by momentum conservation requirements, whereas the disorder-induced D band only appears when there is a breakdown in the in-plane translational symmetry [74]. For a given sp^2 sample, the intensity of the D band for sp^2 carbons increases smoothly as E_{laser} decreases due to structural defects or to finite size effects [47, 122]. In contrast, the G' band is symmetry-allowed and is an intrinsic feature of all sp^2 carbons. Therefore, a Raman investigation of the second-order G'-band by varying E_{laser} for the incident photon provides an experimental way to probe the particular optical phonon branch represented by the heavy curve in Fig. 4-12.

For all frequencies shown in Fig. 6-8, the lineshape is fit by a single Lorentzian component, with a linewidth that has a very weak dependence on E_{laser}. Assuming that the frequency of the G' band depends linearly on E_{laser}, consistent with the behavior of the G' band in other sp^2 carbons, the experimental G' band frequencies for the sample in the present work extrapolate to $2429\,\text{cm}^{-1}$ at $E_{\text{laser}} = 0$, and this phonon frequency is approximately twice the K-point phonon frequency in the 2D Brillouin zone of sp^2 carbons. This extrapolation agrees quite well with the direct measurement of this same phonon frequency (2440–$2445\,\text{cm}^{-1}$), shown in Fig. 6-9.

The weak feature that appears at $2440\,\text{cm}^{-1}$ in the second-order Raman spectrum of 2D graphite and other disordered carbons has been attributed to the sum of two K-point phonons, which each have a frequency of $\sim 1220\,\text{cm}^{-1}$ based on analysis of the 2D resonant Raman effect for the D-band in sp^2 carbons [74]. The phonon density of states in graphite shows a weak peak associated with these K-point phonons

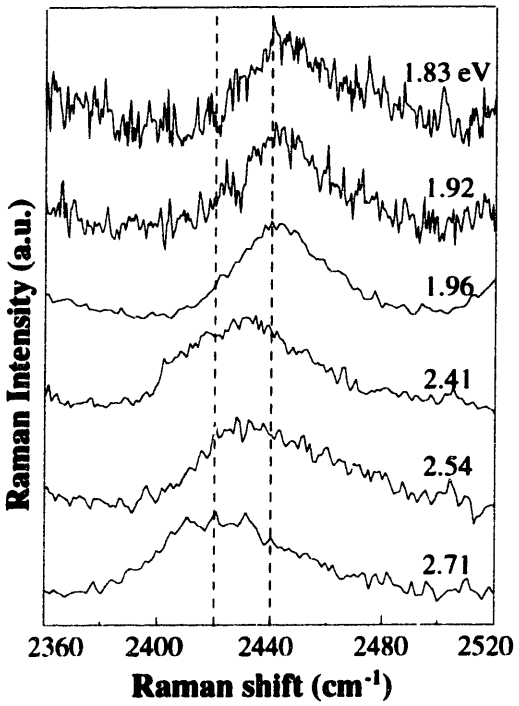

Figure 6-9: The weak non-resonant feature associated with the second harmonic (overtone) of the K-point phonon in the 2D Brillouin zone for six values of E_{laser}.

where an optical and an acoustic branch of the phonon spectrum for 2D graphite are degenerate at the zone edge K-point. The K-point feature which appears in the phonon spectrum of graphite and disordered carbons is non-resonant, because the valence and conduction bands in the electronic structure are degenerate at the K-point in the Brillouin zone and the photon that would be necessary to be in resonance with this phonon therefore has $E_{\text{laser}} \simeq 0$.

For $E_{\text{laser}} = 1.83\,\text{eV}$, $1.92\,\text{eV}$, and $1.96\,\text{eV}$, the spectra in Fig. 6-9 show that the peak frequency and linewidth of the second harmonic (overtone) of the K-point phonon band are independent of E_{laser}, though at higher values of $E_{\text{laser}} = 2.41, 2.54$ and $2.71\,\text{eV}$, the peak downshifts, broadens and becomes more asymmetric. Further insight into these observations is provided by looking at the energies of the *scattered* light. For $1.83 < E_{\text{laser}} < 1.96\,\text{eV}$, the energy of the scattered photon is between $1.50\,\text{eV}$ and $1.66\,\text{eV}$, using a value of $2444/2 = 1222\,\text{cm}^{-1}$ for the K-point phonon in Fig. 6-9. For scattered photons in the range $1.53\,\text{eV}$ to $1.66\,\text{eV}$, Fig. 2-10 shows that

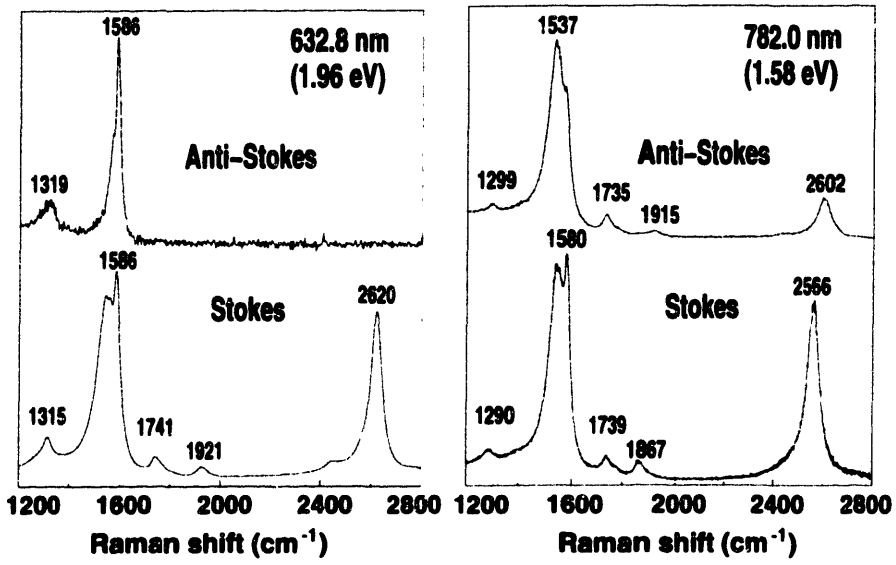

Figure 6-10: Stokes and anti-Stokes Raman spectra for sample S2 (d_t=1.49±0.2 nm) at $E_{\text{laser}} = 1.58\,\text{eV}$ (782 nm) and 1.96 eV (632.8 nm).

resonance with metallic nanotubes occurs. However, when $E_{\text{laser}} \geq 2.41\,\text{eV}$, the scattered phonons have energy $> 2.11\,\text{eV}$ which Fig. 2-10 shows to be outside the metallic window, so that only semiconducting nanotubes are excited. Figure 6-9 shows that the anomalous downshift in the K-point frequency occurs for laser energies that excite semiconducting nanotube phonons resonantly. It should be mentioned that the downshift of the $\omega_{\text{tang}}+\omega_{\text{RBM}}$ combination band, the upshift of the $\omega_{\text{tang}}+2\omega_{\text{RBM}}$ combination band and the downshift of the $2\omega_{K-\text{point}}$ band all occur for $E_{\text{laser}} > 2.4\,\text{eV}$, suggesting a possible coupling between the combination bands and the overtone mode of the K-point phonons.

6.3.4 Stokes vs. anti-Stokes Asymmetry

Differences between the Stokes and anti-Stokes spectra are also found (see Fig. 6-10) for the D- and G'-band features, and the combination feature ($\omega_{\text{tang}} + 2\omega_{\text{RBM}}$) with regard to frequency and relative intensity, while the Stokes and anti-Stokes spectra for the $\omega_{\text{tang}} + \omega_{\text{RBM}}$ band at $E_{\text{laser}} = 1.58\,\text{eV}$ excitation are almost the same. No second-order features are observed in the anti-Stokes spectra above $1700\,\text{cm}^{-1}$ for $E_{\text{laser}} = 1.96\,\text{eV}$, and this observation is explained by a Boltzmann factor reduction

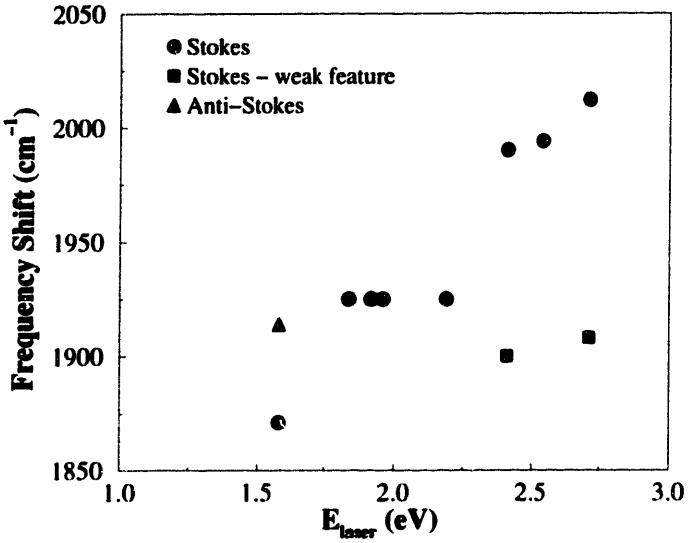

Figure 6-11: The changes in the position of the combination feature $\omega_{\text{tang}} + 2\omega_{\text{RBM}}$ for different values of E_{laser} in both the Stokes (circle and square) and anti-Stokes (triangle) Raman spectra. The squares represent the weak feature located in the range 1900–1920 cm^{-1}, observed for some laser lines (see Fig. 6-7).

in relative intensity, where it is noted that the anti-Stokes spectrum at 1.96 eV laser excitation is dominated by semiconducting nanotubes.

The different frequency shifts of the G'-band features in Fig. 6-10 can be explained by the differing energies of the *scattered* photons which are involved with the 2D resonance Raman enhancement effects associated with the K point in the Brillouin zone [74]. For example, since the energies of the scattered photon in this region of the Raman spectrum are on the order of $\hbar\omega \simeq 0.32$ eV, an expected frequency difference of 34 cm^{-1} between the anti-Stokes and Stokes G'-band frequencies is predicted from the measured $(\partial\omega/\partial E_{\text{laser}})$ slope of 106 cm^{-1}/eV for the G' band dispersion [87], which is to be compared with the observed frequency difference of 36 cm^{-1} shown in Fig. 6-10. The relative intensities of the G' features in the Stokes and anti-Stokes spectra at $E_{\text{laser}} = 1.58$ eV can only, in part, be accounted for by the Boltzmann factor $\exp(-E_{\text{ph}}/kT)$, which affects the anti-Stokes intensity strongly, but not the Stokes intensity. The experiments [10] show that the G' band intensity at $E_{\text{laser}} = 1.58$ eV, where the metallic nanotubes dominate the anti-Stokes spectrum, is much greater than one would expect from the Boltzmann factor argument in relation to the Stokes

intensity at $E_{\text{laser}} = 1.58\,\text{eV}$, where the spectrum is mostly dominated by metallic nanotubes, but some semiconducting nanotubes might also contribute to the spectra (see Fig. 5-4). This additional enhancement of the intensity of the G' band for the metallic nanotubes relative to semiconducting SWNTs implies a stronger electron-phonon coupling for metallic nanotubes.

The second-order features identified with $\omega_{\text{tang}} + 2\omega_{\text{RBM}}$ are observed at $1915\,\text{cm}^{-1}$ and at $1921\,\text{cm}^{-1}$ in the anti-Stokes (Stokes) spectrum at $E_{\text{laser}} = 1.58\,\text{eV}$ ($1.96\,\text{eV}$), respectively, and have Raman scattered photons at $1.78\,\text{eV}$ and $1.76\,\text{eV}$, thereby accounting for the similar phonon frequencies that are observed in the two spectra [10]. In Fig. 6-11 we plot the changes in position of this feature as a function of the laser excitation energy, where it is seen to shift positions discretely; this behavior is not completely understood.

In Chapter 3 we saw that the intensities of the overtone and combination features (due to the A-term and D-term scattering processes) depended on the strength of the vibronic coupling between the ground state and the excited state or among different excited states. In all cases in the Raman spectra of the carbon nanotubes, the second-order (overtones and combination) features are all much better resolved in both the anti-Stokes and Stokes spectra where the metallic nanotubes are contributing to the Raman spectra either by being in resonance with the energy of the incident and/or the scattered photon.

6.4 Conclusions

Overtones and combination modes have been identified in the second-order spectra for the two dominant features in the first-order spectra (the radial breathing mode and the tangential mode) that are associated with the resonant Raman enhancement process arising from the 1D electronic density of states. Just as for the case of the first-order spectra, the resonant contributions to the second-order spectra also involve a different set of (n, m) nanotubes at each laser excitation energy E_{laser}. A second-order analog is observed for the broad spectral band identified with contri-

butions from metallic nanotubes to the first-order tangential mode spectra. The unique feature of the second-order tangential overtone band shows a larger E_{laser} range over which the metallic nanotubes contribute. This effect is attributed to the large ($\hbar\omega_{\text{phonon}} \sim 0.4\,\text{eV}$) energy of these phonons and can be explained within the framework of the energy dependence of the electron 1D density of states. Combination modes associated with $(\omega_{\text{tang}} + \omega_{\text{RBM}})$ and $(\omega_{\text{tang}} + 2\omega_{\text{RBM}})$ have been tentatively identified, and show behaviors as a function of E_{laser} that are consistent with the behavior of their first-order constituents, namely that different nanotubes contribute to the spectra at each value of E_{laser}. Our results indicate that the resonance process (electron-phonon coupling) occurs more strongly for metallic nanotubes than for semiconducting nanotubes, as evidenced by the presence of the G' band and the second-order features at $\omega^{M}_{\text{tang}} + \omega_{\text{RBM}}$ and at $\omega^{M}_{\text{tang}} + 2\omega_{\text{RBM}}$ in the metallic anti-Stokes spectrum at 1.58 eV, but their absence in the 1.96 eV semiconducting anti-Stokes spectrum.

Chapter 7

Surface-enhanced Raman Spectroscopy

7.1 Introduction

Resonance Raman spectroscopy provides a sensitive probe of both the vibrational and electronic properties of carbon nanotubes [26, 89, 95, 102]. Furthermore, surface-enhanced Raman spectroscopy (SERS) can enhance the Raman scattering intensity of species adsorbed on specially prepared metal surfaces by many orders of magnitude, thereby providing a means for observing Raman spectra for single molecules [58, 59]. Surface-enhanced resonance Raman spectroscopy (SERRS) would further increase the enhancement factors, by taking advantage of the orders of magnitude increase in the Raman signal of the scattering species when the laser excitation energy matches and allowed electronic transition. Single wall carbon nanotubes (SWNTs) can show a strong surface-enhanced Raman effect when they are in contact with metallic structures with nanometer sized roughness [33, 55]. The strong enhancement of the Raman signal by SERS opens up exciting opportunities for studying the Raman spectrum of a small number of nanotubes, and, maybe, even a single nanotube, to retrieve the intrinsic properties of SWNTs, which in conventional Raman experiments are hidden under the inhomogeneous broadening coming from ensemble averaging.

The dominant contribution to the enhancement of the Raman signal comes from

strongly enhanced optical fields in the vicinity of the metallic nanostructures (electromagnetic SERS enhancement) [82, 85]. In general, the SERS enhancement can also have a contribution from a so-called "chemical" SERS enhancement mechanism [12, 13, 82, 85], which is based on the specific interaction between the target molecule and the metal substrate, in our case, the interaction between the nanotube and the "SERS-active" metal, which takes place in the extremely strong optical fields around the metallic nanostructure. This enhancement effect is based on changes or improvements in the resonance Raman scattering (RRS) conditions in the "new system", the SERS system, consisting of nanotube, metal substrate and photon, compared to the usual RRS "system" consisting of nanotube and photon, which is studied in "normal" RRS [10, 89, 95].

Previous work has concentrated on the estimate of the total SERS enhancement factor when the carbon nanotubes are adsorbed on silver colloidal clusters [55]. In this Chapter, I focus on the nature of the so-called "chemical contribution" to the SERS enhancement, which is based on the electronic interaction between the nanotubes and the metallic substrate. In particular, the dependence of this interaction on the metal species, and on the laser excitation energy, is studied in the present work.

In the case of carbon nanotubes, which show a strong resonance Raman effect associated with the singularities in the 1D electronic density of states, the sensitivity of the SERS probe can be especially high, since the enhancement effects from both the resonance Raman and SERS effects can be combined multiplicatively for laser excitation wavelengths in the visible/near infrared spectral region.

Surface-enhanced Raman scattering studies under resonance Raman scattering conditions, denoted here by SERRS, applied to SWNTs open up very interesting opportunities to study the "chemical" SERS effect, since a nanotube sample provides "target molecules", which have well defined, and even different [semiconducting (S) and metallic (M)] electronic structures, as illustrated in Fig. 7-1, where interband transitions between van Hove singularities in the 1D density of states of the valence and conduction bands are shown for semiconducting (S) and metallic (M) nanotubes. In this Chapter we investigate the chemical contribution to the SERRS

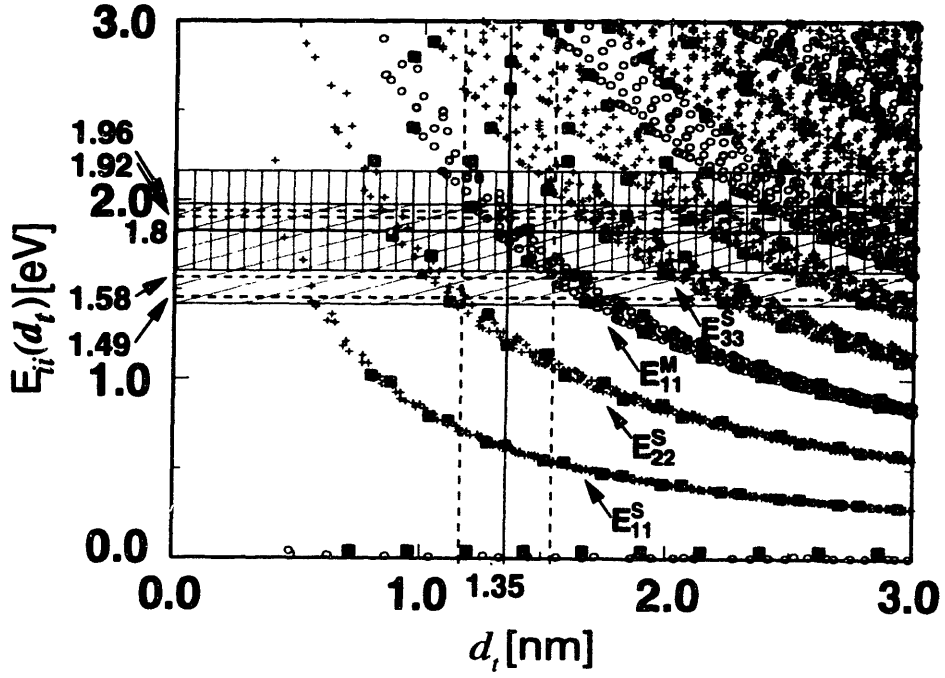

Figure 7-1: Calculation [24, 52, 99] for $\gamma_0 = 2.9\,\text{eV}$ of the energy separations $E_{ii}(d_t)$ for all (n, m) nanotube values vs nanotube diameter $0.7 < d_t < 3.0\,\text{nm}$. Semiconducting and metallic nanotubes are indicated by crosses and open circles, respectively. The filled squares denote zigzag tubes. The vertical lines denote $d_t = 1.35 \pm 0.20\,\text{nm}$ for our single wall carbon nanotube sample. The cross-hatch pattern denotes the range in E_{laser} where metallic nanotubes are expected to contribute resonantly to the anti-Stokes spectrum and the vertical lines pattern indicates the window for the Stokes spectrum.

effect of SWNTs. We apply different excitation wavelengths in order to probe the electronic density of states for metallic and semiconducting nanotubes by measuring the excitation profiles (Raman scattering vs excitation energy) of the tangential modes. Moreover, frequency shifts of the G' band (see Section 6.3.3), which appears at $\approx 2600\,\mathrm{cm}^{-1}$ in the second order spectra of the nanotubes, provide us with an independent probe of the nanotube-metal interaction.

We investigate a number of issues relevant to surface-enhanced Raman scattering (SERS) of single wall nanotubes under resonance Raman conditions. Resonant Raman scattering (RRS) spectra are compared with the corresponding SERRS spectra for six laser excitation energies E_{laser} for Au and Ag film and nanostructured Ag cluster substrates for several distinct spectral features in the Raman spectra. A plot of the interband transitions between van Hove singularities in the 1D density of states in the valence and conduction bands for semiconducting and metallic nanotubes (Fig. 7-1) is used to interpret and compare the detailed features in the RRS and SERS spectra. The selective enhancement of specific features in the Raman spectra is investigated for both semiconducting and metallic nanotubes for various E_{laser} values, by carrying out a detailed lineshape analysis of these spectra. Additional understanding of the resonant SERS enhancement processes is achieved through comparison of the RRS and SERRS anti-Stokes spectra. To extract information about the interaction mechanism between the nanotubes and metal substrates, we have studied the mode frequencies and intensities of the G' band, which is associated with a resonant second-order process for phonons near the K point in the 2D Brillouin zone. From these studies we obtain detailed information about the comparative roles of the electromagnetic and charge transfer SERS enhancement mechanisms for metallic and semiconducting nanotubes.

7.2 Experimental Details

This study was performed on the sample S1 ($d_t = 1.35 \pm 0.20\,\mathrm{nm}$). The Raman and SERS experiments were performed under ambient conditions using a back-scattering

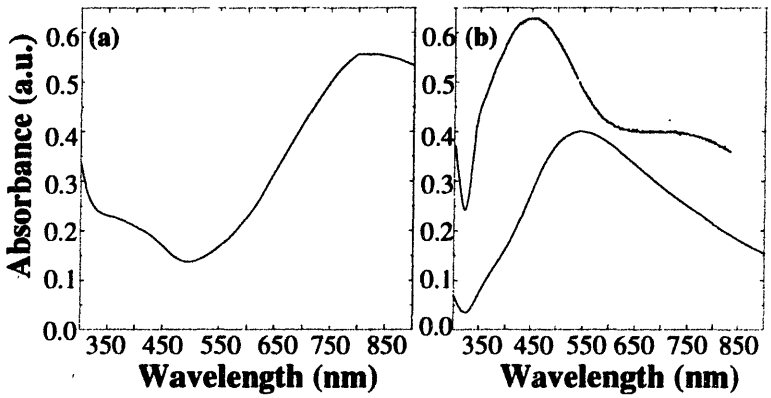

Figure 7-2: Absorbance spectra of (a) a 50 Å gold film and (b) a 100 Å silver film deposited on a glass substrate (lower curve), and fractal colloidal silver clusters in aqueous solution (upper curve).

configuration. For laser excitation radiation we used the 514.5 nm (2.41 eV) line from an Ar^+ laser; the 632.8 nm (1.96 eV) line from an air cooled He-Ne laser; the 647.1 nm (1.92 eV) and 676.4 nm (1.83 eV) lines from a Kr^+ laser; the 782.0 nm (1.58 eV) line of a solid state Al-doped GaAs laser; and the 830 nm (1.49 eV) line of a Ti:sapphire laser.

The SERS substrates were prepared by two methods. One method employed vacuum evaporation of silver (film thicknesses of 50 and 100 Å) or gold (film thickness of 50 Å) on to glass slides. The nanotubes were deposited on the rough metal surface from a dispersion prepared by sonication of the nanotubes in isopropanol. SERS experiments were also carried out using silver colloidal solutions, prepared by either laser ablation of a silver target or by electrochemical reduction of a silver salt [55, 65]. A solution of nanotubes in isopropanol at extremely low nanotube concentrations was added to the silver aqueous colloidal solution. For the measurements a droplet of this sample solution was evaporated on a glass slide, resulting in the placement of fractal colloidal silver structures, with particles ranging in size between 10 and 70 nm, in close contact with some of the single wall nanotubes.

The extinction (absorbance) spectra for the prepared SERS substrates in the absence of the nanotubes are shown in Fig. 7-2. For the silver film, the surface plasmon absorption gives rise to a broad band between 400 and 900 nm, while the absorption

band for the gold island film starts at ~500 nm, and extends to the near infrared region. The very broad extinction (absorption) bands observed for both the Ag and Au substrates are characteristic of the presence of clusters of metal particles, since the single metal particle absorption for silver and gold is known to give rise to much narrower bands at about 400 nm and 520 nm, respectively [79]. The differences in the spectra between colloidal silver particles and evaporated silver film substrates arise from the different distributions of particle sizes within the clusters in the two kinds of silver substrates.

7.3 Results and Discussion

Figure 7-3 shows a comparison, over a broad frequency range from 500–3500 cm^{-1}, between the normal [Fig. 7-3(a)] and surface-enhanced resonant Raman spectra observed from single wall carbon nanotubes (SWNTs) on a silver film [Fig. 7-3(b)] and on a gold film [Fig. 7-3(c)]. These spectra were measured at 632.8 nm (1.96 eV) excitation using 40 W/cm^2 incident laser intensity and have all been corrected for the spectral response of the system.

As shown in Fig. 7-1, a strong contribution to the Stokes Raman scattering process at a laser excitation energy E_{laser}=1.96 eV for nanotube diameters $d_t = 1.35 \pm 0.20$ nm comes from resonance with electronic transitions between the highest energy singularity in the 1D density of electronic states in the valence band to the corresponding lowest energy singularity in the conduction band for *metallic* nanotubes, denoted by $E_{11}^M(d_t)$. Figure 7-1 indicates that a strong resonant contribution for the Stokes process also occurs from *semiconducting* nanotubes within the SWNT sample, with diameters d_t in the upper range of the d_t distribution, mainly through resonance of the scattered photons with the $E_{33}^S(d_t)$ electronic transition (see Fig. 7-1) [11, 32, 89]. The superscripts M and S in $E_{ii}(d_t)$ refer to metallic and semiconducting nanotubes, respectively.

The dominant feature in the spectra in Fig. 7-3 is associated with the first-order tangential G-band occurring in the phonon frequency range 1500–1600 cm^{-1}. From

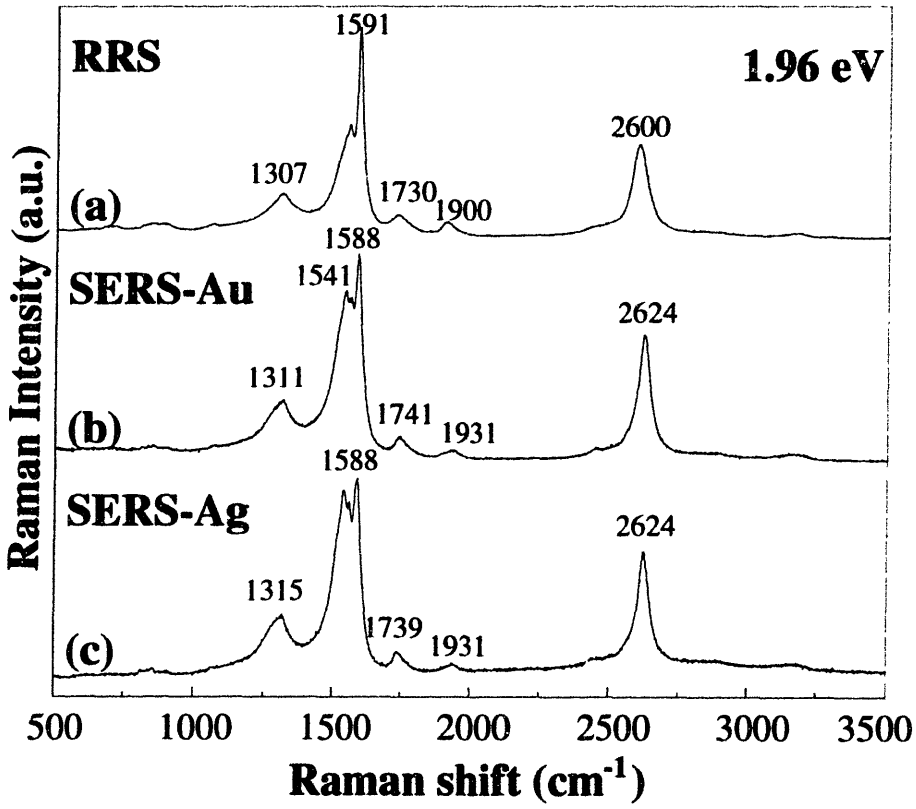

Figure 7-3: Normal resonant Raman scattering (RRS) Stokes spectrum (a), and surface-enhanced resonant (Stokes) Raman Scattering (SERRS) spectra of single-wall nanotubes (SWNTs) adsorbed on (b) gold and (c) silver island films in the 500–3500 cm^{-1} range using laser excitation at E_{laser} = 632.8 nm (1.96 eV).

the lineshape of this broad Raman band [89, 95], we infer that the dominant contribution to the spectrum comes from metallic nanotubes. The features of lower intensity near 1310 cm^{-1} are identified with the D-band [74]. The feature in the 1730–1740 cm^{-1} range is tentatively associated with a combination mode [11] between the tangential mode and the radial breathing mode phonons ($\omega_{tang} + \omega_{RBM}$), while the feature in the 1900–1930 cm^{-1} range is tentatively attributed to a combination mode [11] ($\omega_{tang} + 2\omega_{RBM}$). The weak feature near 2440 cm^{-1} (only observed at higher magnification) is identified with a non-resonant overtone in the second-order spectrum of the K-point vibration at about 1220 cm^{-1} [11], and finally the strong feature in the 2600–2624 cm^{-1} range is due to the G'-band (the overtone of the D-band feature). At a given value of E_{laser}, all nanotubes contribute to the G'-band, while only those nanotubes with electronic transitions (see Fig. 7-1) that are in resonance with the incident and/or scattered photon contribute significantly to the tangential band spectrum.

Figure 7-3 shows that qualitatively similar spectral features are observed for the Stokes process for normal resonant Raman scattering and for SERRS, though there are differences in the detailed lineshape, peak frequencies, and relative intensities between the RRS and SERRS spectra for either of the two metal substrates, as discussed below. The SERRS spectra for the Ag and Au films are almost identical. Generally speaking, the features which show little dispersion (dependence of the Raman frequency on E_{laser}) in the RRS spectra show very small frequency shifts between features in the RRS spectra and in the corresponding SERRS spectra. In contrast, features, such as those associated with the D-band, the $\omega_{tang} + 2\omega_{RBM}$ combination mode, and the G' band, which all show large dispersion in their RRS spectra, also show large differences between their RRS and SERRS spectra at a fixed E_{laser}. These differences in the spectral features between the RRS and SERRS spectra are a main focus of this Chapter, as discussed in more detail in the next section.

7.3.1 Tangential Raman Band

To provide a more detailed comparison between the RRS and SERRS spectra, we show in Fig. 7-4 the tangential band in the Stokes spectra as observed by RRS for five different E_{laser} values (a), by SERRS with a 50 Å Au film for five different E_{laser} values (b), and by SERRS with a 100 Å Ag film for four different E_{laser} values (c). Figure 7-5 shows a plot of the Stokes (solid curve) and anti-Stokes (dashed curve) energy windows where the tangential G-band features of metallic carbon nanotubes (1540 cm^{-1} B–W–F feature and 1580 cm^{-1} Lorentzian oscillator) are expected to be resonantly enhanced for this sample of SWNTs. The vertical lines indicate where the laser excitation energies used in this study fall relative to the metallic resonance energy windows. Regarding the tangential band between 1500–1630 cm^{-1}, semiconducting nanotubes dominate the Stokes spectra at $E_{\text{laser}} = 1.58\,\text{eV}$ and 2.41 eV, metallic nanotubes dominate the spectra at $E_{\text{laser}} = 1.83\,\text{eV}$ and 1.92 eV, while the spectra at 1.96 eV are in an interesting regime, where both metallic and semiconducting tubes contribute strongly. Comparison of the Raman spectra for a given E_{laser} value shows that the SERRS spectra for the two different metal film substrates are more similar to one another, than are the RRS and SERRS spectra at the same E_{laser} value. To make a comparison among the three spectra more quantitative, we carried out detailed lineshape analysis for some of the spectra in Fig. 7-4. The results of this analysis are summarized in Table 7.1, and are shown for illustration in Fig. 7-6 for $E_{\text{laser}} = 1.96\,\text{eV}$. We now discuss these results in more detail.

For the two laser excitation energies where only semiconducting nanotubes contribute to the resonant Stokes spectra, $E_{\text{laser}} = 1.58\,\text{eV}$ [resonant with the $E_{22}^{S}(d_t)$ electronic transition for semiconducting nanotubes (see Fig. 7-1)] and 2.41 eV [resonant with $E_{33}^{S}(d_t)$] [11, 50, 52], the tangential G-band phonon mode region shows Lorentzian components at 1552 cm^{-1}, 1565 cm^{-1}, 1591 cm^{-1} and 1610 cm^{-1} (see Table 7.1), which are associated with normal resonant Raman spectra from semiconducting nanotubes (consistent with polarization measurements) [44], as shown in Fig. 7-1. The SERRS spectra at $E_{\text{laser}} = 1.58\,\text{eV}$ and 2.41 eV for both Ag and Au

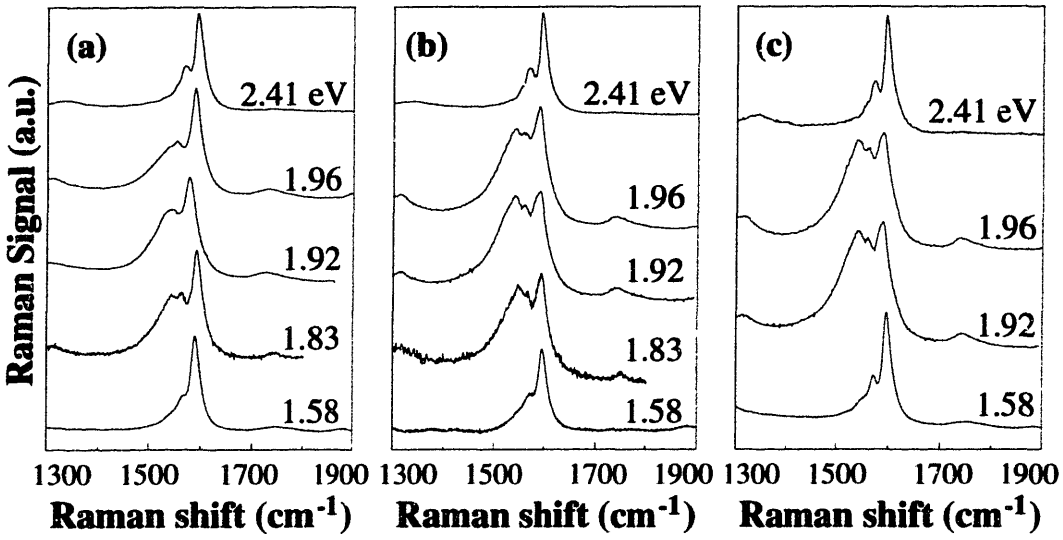

Figure 7-4: The spectral region between 1300–1900 cm^{-1} in more detail showing the RRS Stokes spectrum (a), and the SERRS Stokes spectra for SWNTs adsorbed on (b) a 50 Å gold film and (c) a 100 Å silver film for several laser excitation energies E_{laser}.

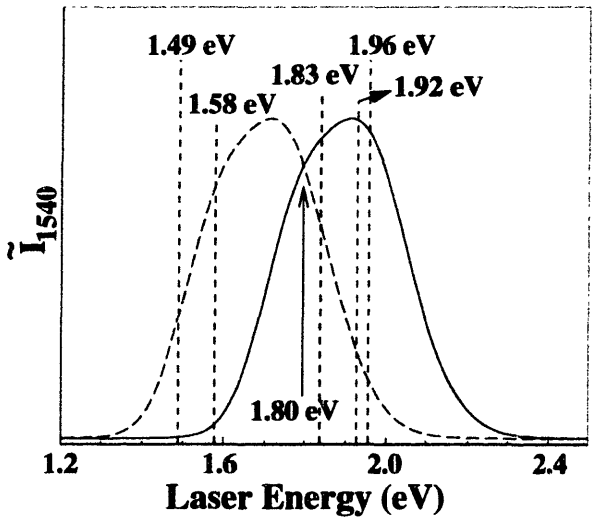

Figure 7-5: Metallic window for carbon nanotubes with diameter of $d_t = 1.35 \pm 0.2$ nm for the Stokes (solid line) and anti-Stokes (dashed line) processes, which cross at E_{laser} = 1.80 eV [10]. Also indicated on the figure by vertical dashed lines are E_{laser} values used in this study.

film substrates are closely similar to each other and to the normal Raman spectra, and basically the same frequencies and relative intensities can be observed for the four constituent Lorentzian components, as indicated in Table 7.1. Below we describe SERRS and RRS spectra taken at $E_{\text{laser}} = 1.49\,\text{eV}$ under different experimental conditions, and using a fractal colloidal silver substrate, again yielding the same Stokes spectra for semiconducting SWNTs (see Fig. 7-8), namely that the relative intensities of the four dominant Lorentzian components are very *similar* for the SERRS and RRS Stokes spectra for *semiconducting* SWNTs.

For the three values of E_{laser} in Fig. 7-4 within the $1.8 < E_{\text{laser}} < 2.0\,\text{eV}$ range, the RRS spectra show the appearance of new components at $1540\,\text{cm}^{-1}$ (B–W–F) and $1581\,\text{cm}^{-1}$, which are identified (see Fig. 7-1) with resonantly enhanced features from metallic nanotubes in resonance with the $E_{11}^{M}(d_t)$ transition [89]. In this laser excitation energy range, significant changes can be seen when comparing the RRS spectra to the two corresponding SERRS spectra, whereas the SERRS spectra for nanotubes on Au and Ag are similar to one another. In particular, the lineshape analysis in Fig. 7-6 at $E_{\text{laser}} = 1.96\,\text{eV}$ shows that the contribution of the lower frequency Breit–Wigner–Fano component for the metallic nanotubes is much more pronounced for the SERRS spectra than for the RRS spectrum, though the peak frequencies for both of these metallic components appear to be the same. The SERRS enhancement of the nanotubes adsorbed on the silver island films (at $E_{\text{laser}} = 1.96\,\text{eV}$) is particularly strong for the $1540\,\text{cm}^{-1}$ (B–W–F) metallic component (110% increase in integrated intensity compared to the $1540\,\text{cm}^{-1}$ B–W–F component in the RRS spectrum), while the $1581\,\text{cm}^{-1}$ component shows less difference (only ~20% increase) between the RRS and SERRS spectra. For $E_{\text{laser}} = 1.83\,\text{eV}$ and $1.92\,\text{eV}$, which are both within the metallic window for this sample, the SERRS and RRS spectra can be fit with the same Raman lineshapes as for the spectra at $E_{\text{laser}} = 1.96\,\text{eV}$, discussed above, and once again the Breit-Wigner-Fano component at $1540\,\text{cm}^{-1}$ associated with the metallic nanotubes is more strongly enhanced in the SERRS spectra. The experimental intensity ratios are given explicitly in Table 7.1 for various laser excitation energies and for the relevant Lorentzian oscillators and B–W–F lineshape at

Table 7.1: Frequencies (ω), full width at half maximum intensity (Γ) of the curves, and the relative intensity (the ratio of the integrated intensity of each component of the tangential G-band to that of the 1592 cm^{-1} peak, denoted by Rel. Int.) as a function of E_{laser} for the Stokes spectra. The 1540^{-1} curve is a Breit–Wigner–Fano lineshape with 1/q (shown in parentheses beside Rel. Int. for the B–W–F curves) varying from -0.15 to -0.24. The symbols (*) and (†) refer to components associated with metallic and semiconducting nanotubes, respectively.

		RRS	SERS-Au	SERS-Ag
$\omega(cm^{-1})$	Γ (cm^{-1})	Rel. Int. (1/q)	Rel. Int. (1/q)	Rel. Int. (1/q)
		$E_{laser} = 1.83\,eV$		
1540*	70	5.0 (-0.20)	7.2 (-0.19)	—
1552†	18	0.2	0.2	—
1565†	14	0.3	0.4	—
1581*	22	1.2	1.3	—
1592†	16	1.0	1.0	—
1610†	40	0.4	0.5	—
		$E_{laser} = 1.92\,eV$		
1540*	70	5.3 (-0.19)	6.0 (-0.20)	7.1 (-0.24)
1552†	18	0.2	0.2	0.2
1565†	14	0.3	0.4	0.4
1581*	22	1.1	1.3	1.2
1592†	16	1.0	1.0	1.0
1610†	40	0.4	0.4	0.4
		$E_{laser} = 1.96\,eV$		
1540*	70	3.5 (-0.22)	5.9 (-0.17)	7.2 (-0.15)
1552†	18	0.2	0.2	0.1
1565†	14	0.3	0.3	0.3
1581*	22	0.9	1.1	1.1
1592†	16	1.0	1.0	1.0
1610†	40	0.5	0.5	0.6
		$E_{laser} = 2.41\,eV,\ 1.58\,eV$		
1552†	18	0.2	0.2	0.2
1565†	14	0.4	0.4	0.4
1591†	15	1.0	1.0	1.0
1610†	26	0.5	0.5	0.5

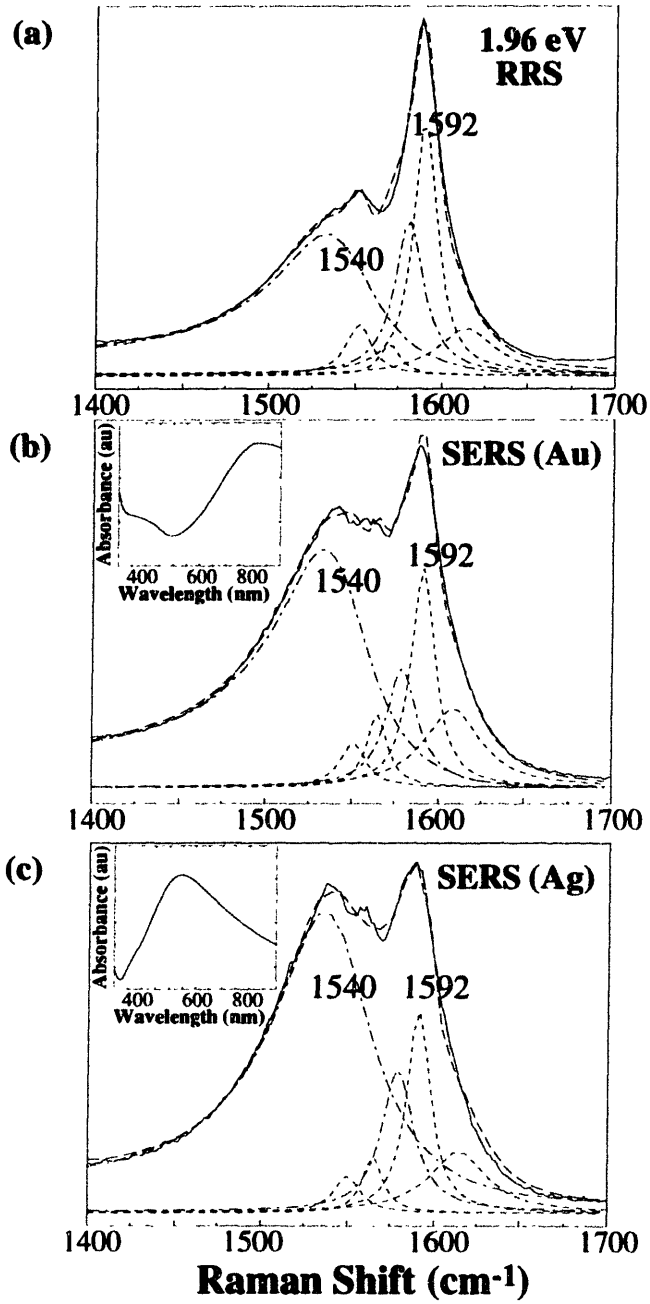

Figure 7-6: Deconvolved spectra of the tangential vibrational band obtained with laser excitation (E_{laser}) at 632.8 nm (1.96 eV) for (a) normal resonant Raman spectroscopy, (b) SERRS on an Au substrate, (c) SERRS on an Ag substrate. The insets to (b) and (c) are the absorbance vs. photon wavelength for each metal substrate. A detailed lineshape analysis of the spectra is made with the same Lorentzian oscillators at 1552 cm^{-1}, 1565 cm^{-1}, 1592 cm^{-1} and 1610 cm^{-1} for the semiconducting nanotubes, a Lorentzian oscillator at 1581 cm^{-1} and a Breit–Wigner–Fano lineshape at 1540 cm^{-1} are used for the metallic nanotubes (see Table 7.1). The dominant component in the metallic nanotube regime (1540 cm^{-1}) and the strongest component in the semiconducting nanotube regime (at 1592 cm^{-1}) are labelled.

$1540\,\mathrm{cm}^{-1}$ at that value of E_{laser}. Table 7.1 shows that the Raman B–W–F features at $1540\,\mathrm{cm}^{-1}$ are strongly enhanced in the SERRS spectra relative to the RRS spectra, while the intensity of the $1581\,\mathrm{cm}^{-1}$ component is only slightly changed. In the spectra at $E_{\mathrm{laser}} = 1.96\,\mathrm{eV}$, $1.92\,\mathrm{eV}$ and $1.83\,\mathrm{eV}$, the relative intensities of the weaker components at 1552, 1565, 1591 and $1610\,\mathrm{cm}^{-1}$, that are associated with the semiconducting nanotubes, are almost the same for the RRS and SERRS spectra. At a given value of E_{laser}, all components of the the SERRS spectra for the metallic nanotubes are about equally enhanced (within experimental error) for the silver and gold substrates, as shown in Table 7.1. On the other hand, the contributions to the spectra from the semiconducting nanotubes (at $1552\,\mathrm{cm}^{-1}$, $1565\,\mathrm{cm}^{-1}$, $1592\,\mathrm{cm}^{-1}$ and $1610\,\mathrm{cm}^{-1}$) are essentially the same for SERRS as compared to RRS, and are also the same for the Ag and Au substrates for all values of E_{laser} shown in Table 7.1.

Further information is obtained by comparison of the *anti-Stokes* RRS and SERRS spectra of the SWNTs. To obtain sufficient intensity to observe the SERRS anti-Stokes spectra, fractal colloidal silver clusters were used for the "SERS-active" substrate, exploiting the very high effective enhancement factors (on the order of 10^{10} - 10^{12}) recently reported for nanotubes adsorbed on such silver surface when excited at 830 nm ($E_{\mathrm{laser}} = 1.49\,\mathrm{eV}$) [55]. Figure 7-7 shows the Raman spectra obtained from a bundle of SWNTs associated with the silver colloids. Position #1 is located far away from the colloids and shows no Raman signal. Position #2 is just below the colloid and shows a weak Raman signal, while at position #3 we are directly hitting the colloids with the excitation laser, and the large enhancement in Raman signal intensity is clearly seen. In general, due to Boltzmann population considerations, the intensity of the anti-Stokes signal of the tangential modes is expected to be very weak. In normal RRS spectroscopy on SWNTs, an increase in the temperature results in a higher population of these vibrational levels and makes it possible to obtain measurable anti-Stokes spectra [10]. However, in SERRS, the strong thermal coupling of the nanotubes to the metal substrate prevents the occurrence of such an increase in the temperature. But at extremely strong SERRS enhancement levels, the Raman Stokes process measurably populates the first excited vibrational level in excess of the

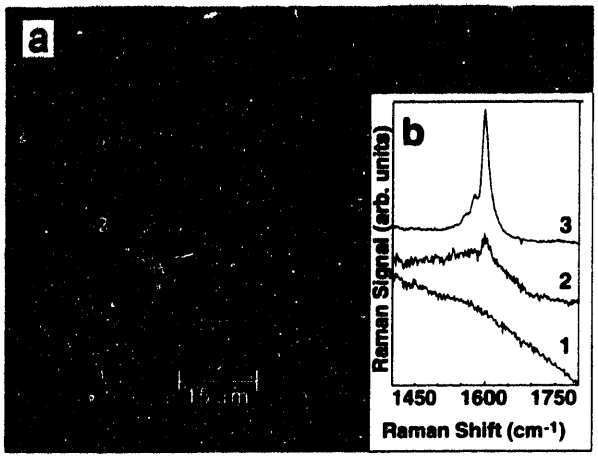

Figure 7-7: A long bundle of SWNTs is shown associated with colloidal silver particles (such as near position #3). The square at the top of the figure is a NaCl crystal, which is used to cause the silver particles to form the clusters. The inset shows the Raman spectra obtained with laser excitation at $E_{\text{laser}} = 1.49\,\text{eV}$, taken at three points along the bundle [55].

Boltzmann population. This results in a strong anti-Stokes SERRS spectrum measured at 830 nm (1.49 eV) excitation [55]. Figure 7-8(b) shows a lineshape analysis of RRS and SERRS Stokes and anti-Stokes spectra of the tangential band measured at this excitation wavelength. In contrast to the Stokes spectra at 1.49 eV discussed above, where RRS and SERRS spectra show similar lineshapes characteristic of semiconducting nanotubes, changes in relative intensities are seen in the anti-Stokes side of the Raman spectra, where so-called pre-resonance effects involving the *scattered* photon can occur [55]. Although the energy of the incident photon (1.49 eV) is lower than the energy of the $E_{11}^{M}(d_t)$ electronic transition associated with the metallic nanotubes (thus preventing any resonant Raman enhancement for metallic nanotubes in the Stokes spectra), the upshifted *scattered* anti-Stokes photon gives rise to a resonant Raman effect for metallic nanotubes through the $E_{11}^{M}(d_t)$ electronic transition, as shown in Fig. 7-5, where the Raman bands of the metallic nanotubes ($1540\,\text{cm}^{-1}$ B–W–F feature and $1580\,\text{cm}^{-1}$ Lorentzian oscillator) are expected to be resonantly enhanced [10].

It is very interesting to note that while the Stokes spectra at $E_{\text{laser}} = 1.49\,\text{eV}$ show only vibrational modes associated with the semiconducting nanotubes (with no dif-

(a)

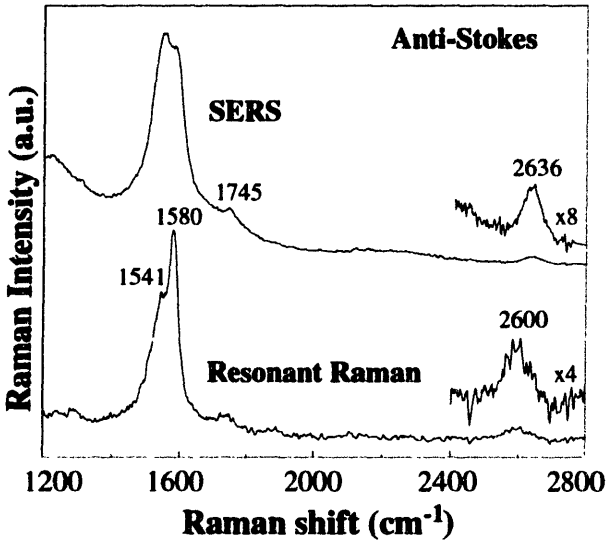

(b)

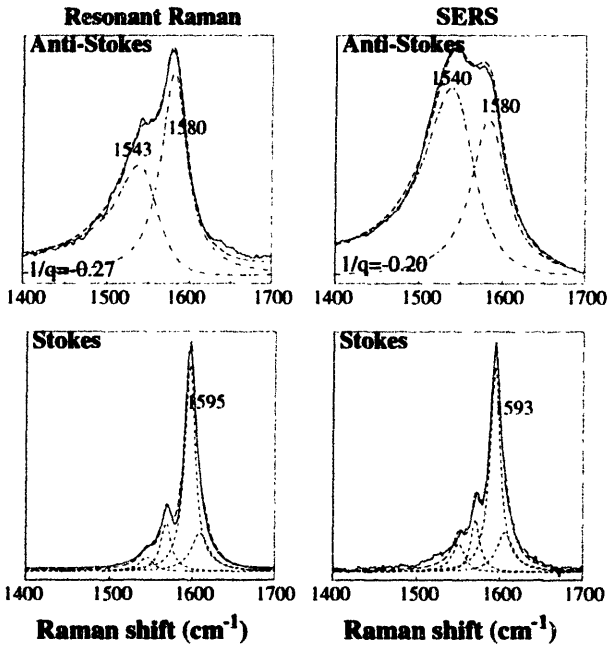

Figure 7-8: (a) Anti-Stokes Resonant Raman and SERS spectra of SWNTs adsorbed on colloidal silver particles taken with laser excitation at $E_{\text{laser}} = 1.49\,\text{eV}$. (b) Detailed lineshape analysis of the anti-Stokes tangential vibrational band. The Stokes spectra at $E_{\text{laser}} = 1.49\,\text{eV}$ are also shown for comparison.

Table 7.2: Relative intensities and FWHM linewidths (Γ), and additionally the value of 1/q for the Breit–Wigner–Fano peak, for fits to the RRS and SERRS *anti-Stokes* spectra for metallic (*) nanotube components at $E_{\text{laser}} = 1.49\,\text{eV}$.

	RRS			SERS-Ag		
ω (cm^{-1})	†Rel. Int.	Γ (cm^{-1})	1/q	†Rel. Int.	Γ (cm^{-1})	1/q
1540*	0.75	60	-0.27	2.21	70	-0.20
1580*	1.0	38	—	1.0	52	—

† Intensity of $1540\,\text{cm}^{-1}$ feature (B–W–F lineshape) taken relative to $1580\,\text{cm}^{-1}$ feature (Lorentzian lineshape).

ference in relative intensities of the Lorentzian components from RRS to SERRS) and no measurable scattering intensity from metallic nanotubes (see Fig. 7-8), the anti-Stokes spectra in the tangential phonon region, for both the RRS and SERRS spectra can be fitted, using only the $1540\,\text{cm}^{-1}$ B–W–F feature and $1580\,\text{cm}^{-1}$ Lorentzian oscillator associated with metallic nanotubes and no measurable scattering intensity for semiconducting nanotubes, as shown in Table 7.2. The anti-Stokes spectra obtained at $E_{\text{laser}} = 1.49\,\text{eV}$ (Fig. 7-8) are therefore in a very special resonance condition, allowing discussion of the differences in the observed RRS and SERRS lineshapes when only metallic nanotubes appear to contribute to the anti-Stokes Raman signal. This condition is not observed in the Stokes spectra for our sample, for any of the available laser wavelengths. The different spectral RRS profiles between the Stokes and anti-Stokes Raman spectra were discussed in detail in Chapter 5 for the larger diameter nanotubes sample S2 ($d_t = 1.49 \pm 0.2\,\text{nm}$), and similar results are shown here for sample S3 ($d_t = 1.35 \pm 0.2\,\text{nm}$). The fact that, for the same laser wavelength, the Stokes and anti-Stokes spectra can be in a completely different (metallic vs semiconducting nanotube) regime can be understood in terms of resonance Raman scattering theory and the exceptional electronic structure of metallic and semiconducting nanotubes (see Fig. 7-1). However, if the incident photon is in weak resonance with the $E_{ii}(d_t)$ transitions (dashed horizontal line at 1.49 eV in Fig. 7-1), while the scattered photon is in a much stronger resonance condition, then RRS enhancement will emphasize the resonance with the scattered photon. Since the resonant enhancement factors

can be large ($> 10^2$), it is possible for the scattered photon to dominate the resonance enhancement process, thereby allowing a given E_{laser} excitation to probe either metallic or semiconducting nanotubes very selectively, thereby resulting in very different lineshapes at the Stokes and anti-Stokes sides. Such effects are clearly seen in Fig. 7-8(b).

We can account for this observation in the following way. Each component associated with metallic nanotubes (1540 and 1580 cm^{-1}) correspond to different normal mode displacements. The equation for the Raman scattering intensity for each of the Lorentzian components of the ensemble of metallic nanotubes that is involved in the resonant Raman process was shown in Chapters 4 and 5 (and here reproduced) to be written as:

$$\begin{aligned} I_M = \; & \sum A \exp\left\{\tfrac{-(d_t-d_0)^2}{\Delta d^2/4}\right\} \\ & \times[(E_{11}^M(d_t) - E_{\text{laser}} \pm E_{\text{ph}})^2 + \Gamma_e^2/4]^{-1} \\ & \times[(E_{11}^M(d_t) - E_{\text{laser}})^2 + \Gamma_e^2/4]^{-1} \end{aligned} \tag{7.1}$$

in which $I_M \equiv I_M(E_{\text{laser}}, d_t)$ is the scattering intensity for the Stokes process (+ sign) and for the anti-Stokes process (− sign) for each Lorentzian component of the ensemble of metallic nanotubes in resonance with the $E_{11}^M(d_t)$ electronic transition between the highest lying valence band van Hove singularity and the lowest lying conduction band singularity in their 1D electronic density of states [26, 89]. This formula was introduced before we started using the B–W–F lineshape analysis. However, the difference in integrated intensity of the B–W–F feature and a Lorentzian oscillator with similar fitting parameters (but setting 1/q=0) are expected to be small. The sum in Eq. (7.1) is over all metallic nanotubes having a diameter distribution given by $d_t = d_0 \pm \Delta d$ where d_0 is the average diameter and Δd is the FWHM width of a Gaussian distribution of nanotube diameters. Also E_{ph} denotes the phonon frequency for the tangential band (0.20 eV), Γ_e is a damping parameter determined by fitting experimental data to Eq. (7.1), A is a dimensionless factor proportional to the Boltzmann factor $\exp(-E_{\text{ph}}/kT)$ for the anti-Stokes process and a constant for the Stokes process [11, 89], and the magnitude of this factor A depends on the scattering cross section for the normal mode displacements and symmetry of a given vibrational

mode.

Equation (7.1) applies to each metallic component individually. For example, Fig. 7-5 shows the calculated intensity for the $1540\,\mathrm{cm}^{-1}$ Breit–Wigner–Fano lineshape (the dominant component in the Raman spectra for metallic nanotubes) as a function of E_{laser} for the Stokes and anti-Stokes RRS processes. The two components ($1540\,\mathrm{cm}^{-1}$ and $1581\,\mathrm{cm}^{-1}$) have somewhat different intensity profiles, which also differs for RRS relative to SERRS. Therefore the composite spectrum that is observed for the tangential modes after summing over the contributions from each nanotube in the sample may show different enhancements for the $1540\,\mathrm{cm}^{-1}$ and $1581\,\mathrm{cm}^{-1}$ components as a function of E_{laser}.

For the metallic nanotubes, which are observed in the anti-Stokes spectrum at $E_{\mathrm{laser}} = 1.49\,\mathrm{eV}$ [10, 55], the RRS spectra and the SERRS spectra, taken with nanotubes adsorbed on the colloidal Ag particles, are also consistent with the corresponding results observed at $E_{\mathrm{laser}} = 1.96\,\mathrm{eV}$, $1.92\,\mathrm{eV}$ and $1.83\,\mathrm{eV}$ for the Stokes process on Ag and Au film substrates. The same peak frequencies for the two components for the tangential band feature for metallic nanotubes, $1540\,\mathrm{cm}^{-1}$ (B–W–F) and $1581\,\mathrm{cm}^{-1}$ (Lorentzian), that give a good fit to the observed Raman band in the anti-Stokes spectra for both the RRS and SERRS spectra at $1.49\,\mathrm{eV}$, also give a good fit to the RRS and SERRS Stokes spectra at $E_{\mathrm{laser}} = 1.83$, 1.92 and $1.96\,\mathrm{eV}$.

A more detailed comparison of the relative intensities of each of these components associated with metallic nanotubes in the anti-Stokes spectra at $1.49\,\mathrm{eV}$ (while the nanotubes adsorbed on silver colloidal clusters [55]) is given in Fig. 7-8 and in Table 7.2. Both anti-Stokes tangential G-band spectra were fit with similar (metallic) lineshapes, although the SERRS features are broader and the 1/q value is decreased slightly relative to the corresponding RRS feature (Fig. 7-8(b)). However, the intensity ratio I_{1540}/I_{1580} is much larger for SERRS (2.21) than for RRS (0.75). For these anti-Stokes spectra (at $1.49\,\mathrm{eV}$), the metallic nanotubes dominate, and the $1540\,\mathrm{cm}^{-1}$ B–W–F component is the one that is most enhanced by SERRS.

Table 7.3: Wavenumbers (ω) and FWHM (Γ) (both given in cm^{-1}) for the second-order G' Raman band observed at the indicated wavelengths for resonant Raman and SERS spectra. Also listed for $E_{laser} = 2.41$ eV and 1.96 eV are the intensities of the G'-band feature taken relative to the tangential G-band feature from the corresponding spectrum (Rel. Int.).

	2.41 eV			1.96 eV			1.92 eV	
Spectra	ω	Γ	Rel. Int.	ω	Γ	Rel. Int.	ω	Γ
RRS	2662	63	0.15	2600	68	0.43	2604	66
SERS(Au)	2674	56	0.18	2624	51	0.59	2623	48
SERS(Ag)	2676	54	0.19	2624	49	0.63	2622	47

7.3.2 Other Raman Bands

In addition to changes in the tangential vibrational modes, other features in the Raman spectra for SWNTs are also perturbed by the presence of the metal substrate (see Fig. 7-3). In this figure, we see that the D-band feature (1307–1315 cm^{-1}) in the first-order Stokes spectrum at 1.96 eV is upshifted by 4–8 cm^{-1} in the SERRS spectrum relative to the RRS spectrum, while the corresponding second-order G'-band is upshifted by 24 cm^{-1} upon interaction with the metal substrate. The data in Table 7.3 for the G'-band at three values of E_{laser} [2.41 eV (514.5 nm); 1.96 eV (632.8 nm); 1.92 eV (647.1 nm)] show that the shift in the G' band is much larger for E_{laser} values where *metallic* nanotubes contribute strongly to the Raman spectra than for the E_{laser} value in the semiconducting regime.

Furthermore at $E_{laser} = 1.96$ eV (within the metallic window), the intensity of the G' band relative to that of the tangential mode, denoted simply by $(I_{G'}/I_{tang})$, has a value of 0.4 for the normal Raman spectra as compared to a significantly larger value of 0.6 for the SERS spectra. In contrast, for $E_{laser} = 2.41$ eV where only the semiconducting nanotubes are in resonance with E_{laser}, the ratio $(I_{G'}/I_{tang})$ has the same value of 0.2 for both the RRS and SERRS spectra.

Figure 7-8 for $E_{laser} = 1.49$ eV also shows a large upshift in the frequency of the second-order G'-band for the adsorbed nanotubes (from 2600 cm^{-1} for the normal resonant Raman spectrum to 2636 cm^{-1} for the SERRS spectrum) at the *anti-Stokes* side

of the Raman spectra. For the anti-Stokes spectra which is dominated by resonance with metallic nanotubes, the relative intensities of the G' band to the tangential band seems to be a factor of $\sim$2 larger for the RRS spectrum relative to the SERS spectrum which can be explained by laser heating of the samples in RRS. Such heating does not, however, appear for SERRS because of the good thermal contact between the nanotubes and the metal substrates.

In summary, the intensities in the SERS Stokes spectra of the G'-band are larger relative to the tangential vibrational band for the metallic single-wall carbon nanotubes, in contrast to the situation for the semiconducting nanotubes where the intensity ratios are the same for all E_{laser} values that were studied.

The $(\omega_{\text{tang}}+\omega_{\text{RBM}})$ and $(\omega_{\text{tang}}+2\omega_{\text{RBM}})$ combination band frequencies at 1730 cm^{-1} and 1905 cm^{-1}, respectively, in the RRS spectrum in Fig. 7-3 are also upshifted to 1740 cm^{-1} and 1931 cm^{-1}, respectively, for the adsorbed nanotubes in the corresponding SERRS spectra at 1.96 eV. It is interesting to note that the larger upshift for the $(\omega_{\text{tang}}+2\omega_{\text{RBM}})$ combination mode is consistent with the larger variation of this mode frequency with E_{laser} in the RRS spectra [11]. It is interesting to note that, as was shown in section 6.3, the combination feature $\omega_{\text{tang}}+2\omega_{\text{RBM}}$ was located at $\sim$1930 cm^{-1} when the tangential G-band features for *metallic* nanotubes were resonantly enhanced in the Raman spectra.

Since the mechanism responsible for resonant Raman scattering for the D-band in the first-order spectrum and for the G'-band in the second-order spectrum at twice the D-band frequency is quite different from that for the tangential band [74], a comparison of the behavior of these modes under normal resonant Raman scattering and under SERRS yields valuable information about these phenomena. From the above discussion on the tangential mode spectra, we conclude that the same Lorentzian components appear in the lineshape analysis of the RRS and the SERRS spectra for the semiconducting nanotubes (at 1552, 1565, 1591 and 1610 cm^{-1}) without change in the relative intensities of these Lorentzian components. And even in the RRS and SERRS spectra for the *metallic* nanotubes, the same components (1540 cm^{-1} B-W-F lineshape and 1580 cm^{-1} Lorentzian oscillator) appear in both the RRS and SERRS

spectra, though with different relative intensities at a given value of E_{laser}. From these results, we conclude that the normal mode vibrations are essentially unchanged by the interaction between the nanotubes and the metal substrate. But rather the electronic excitations are somewhat perturbed by this interaction, with evidence for this interpretation coming from the upshift in the D-band and the G'-band frequencies in the SERRS spectra for all nanotubes relative to the corresponding RRS spectra, and from the increase in the relative intensities of these Raman bands in the SERRS spectra relative to the RRS spectra for the metallic nanotubes. Following this line of reasoning, we argue that the interaction between the nanotubes and the metal substrate perturbs the electronic structure near the K point of the 2D Brillouin zone, so that the D-band and the G'-band vibrational spectra which are resonantly excited by a given laser energy E_{laser}, now correspond to a slightly upshifted k-point relative to the K point in the 2D Brillouin zone. But since the D-band (and the G'-band) phonon that is resonantly enhanced has the same wave vector as that of the resonant electronic transition [74], the upshift in the SERRS spectrum relative to the RRS spectrum is a measure of the strength of the electronic interaction between the nanotube and the metal substrate. Because of the much larger experimentally observed upshift of the G' band frequency for the *metallic* nanotubes, we conclude that the interaction of the metallic nanotubes with the metal substrate is much stronger than for the semiconducting nanotubes. This conclusion is also consistent with the increased intensity of the components (especially the B–W–F component) associated with the tangential G-band of metallic nanotubes in the SERRS spectra relative to the intensity of the same Lorentzian components in the RRS spectra. These arguments also lead to the conclusion that the electron-phonon interaction is stronger for the metallic nanotubes than for the semiconducting nanotubes.

Surface-enhanced resonant Raman spectroscopy predominantly enhances the symmetric vibrations for the nanotubes. The large upshift in the G' band for metallic nanotubes in the SERRS spectra (by $\sim 24\,\text{cm}^{-1}$) for $E_{\text{laser}} = 1.96\,\text{eV}$, and for the semiconducting nanotubes (by $\sim 13\,\text{cm}^{-1}$) at $E_{\text{laser}} = 2.41\,\text{eV}$ is consistent with the "breathing-mode" type motion of the carbon atoms for the mixed "quasi-acoustic" op-

tic phonon branch near the K-point [74]. Normal resonant Raman and SERS spectral intensities are both larger for the totally symmetric modes, and the very appearance of the G' band in the Raman spectra relies greatly on the "breathing-type" motion of the phonons involved [74]. The larger shift in the G' band in the SERS spectra for the metallic nanotube regime (which includes spectra taken at both 1.96 eV and 1.92 eV) would also be an indicator of a stronger interaction of the metallic nanotubes with the metal substrate reflected in the greater SERS enhancement for the metallic nanotubes while the smaller shift for the semiconducting nanotubes is consistent with a lesser SERS enhancement due to a smaller interaction between semiconducting nanotubes and the metal substrate. The frequency upshift of the combination bands ($\omega_{\text{tang}} + \omega_{\text{RBM}}$ and $\omega_{\text{tang}} + 2\,\omega_{\text{RBM}}$) also support the argument that the combination modes contain a totally symmetric mode in the decomposition of the direct product of the symmetry types contained in the combination mode.

7.3.3 The SERS Enhancement Mechanism

There are two major contributions to the surface enhancement of the resonant Raman scattering of carbon nanotubes adsorbed on metallic surfaces: the "electromagnetic" mechanism and the "chemical" mechanism, based on a charge transfer between the metallic surface and the nanotubes. The "electromagnetic" mechanism is due to the enhanced electromagnetic fields at or near nanometer size metallic particles, in our case "rough" silver and gold surfaces. Particularly strong field enhancement up to 10 to 12 orders of magnitude can exist for metallic substrates showing fractal cluster structures [73, 113, 115]. At the excitation wavelengths used in the reported experiments, the electromagnetic enhancement is expected to be based on resonances of the optical fields with the collective electronic excitations of such cluster structures and not with those of the isolated particles. This "cluster-based" field enhancement does not directly depend on the sizes and shapes of the individual particles, and therefore is expected to be similar for our metal island films and colloidal silver surfaces. The fields highly localized in small areas of the cluster [73] result in much stronger SERRS enhancement for clusters than for isolated particles [56, 57]. Theoretical

calculations predict that these SERS-active substrates should exhibit a particularly strong enhancement at longer wavelength (near infrared) excitation [115]. In general, the electromagnetic enhancement mechanism is independent of the chemical nature of the species, and is also expected to be the same for all vibrational modes. The existence of such large enhancement levels has been shown for both semiconducting and metallic nanotubes [55]. The second enhancement mechanism, the charge-transfer or chemical effect, strongly depends on the electronic structure of the nanotubes, and this mechanism should sensitively differentiate between the very different 1D density of states between the metallic and semiconducting nanotubes.

For Raman Stokes spectra within the semiconducting regime ($E_{\text{laser}} = 1.58\,\text{eV}$ and $2.41\,\text{eV}$), no significant dependence of the SERRS spectra is observed on the metal species (silver or gold) nor on the metal film thickness for a given E_{laser} value. In the semiconducting nanotube regime, all SERRS bands are enhanced by the same amount, as expected from the electromagnetic enhancement mechanism.

For laser excitation energies within the metallic resonance window, however, we observe an enhanced contribution to the SERRS spectra of the components associated with metallic nanotubes (the $1540\,\text{cm}^{-1}$ B–W–F component and the $1580\,\text{cm}^{-1}$ Lorentzian oscillator). We explain this effect in terms of a charge transfer enhancement, which is operative for the metallic nanotubes, in addition to the strong electromagnetic field effect discussed above. The different behavior between the SERRS spectra of metallic and semiconducting nanotubes arises from the major differences in their electronic structures, in their 1D density of states near the Fermi level, and from their stronger electron-phonon coupling compared to semiconducting nanotubes.

It is well established that the chemical mechanism of enhancement can be described as a resonant Raman effect involving electronic levels of the substrate and of the adsorbed molecules as well. The chemical effect therefore depends on the occurrence of a resonance condition between the laser energy and the energy separation of the van Hove singularities in the 1D peaks of the electronic density of states of the nanotube adsorbate, as modified by interaction with the metal substrate.

Furthermore, the selection rules for the charge transfer mechanism predict that

modes with different symmetries and with different vibrational normal mode displacements should behave differently, just as for the resonant Raman selection rules [21, 69]. In particular, totally symmetric modes are more likely to be enhanced through the Franck–Condon mechanism in both SERS and resonant Raman spectroscopy (A-term scattering) [19]. The fitted data in Fig. 7-6 indicate that the different tangential G-band components identified with the metallic nanotubes are enhanced by differing amounts, with a preferential enhancement of the $1540\,\mathrm{cm}^{-1}$ B–W–F component. Both the RRS and SERRS spectra indicate that the strongly enhanced $1540\,\mathrm{cm}^{-1}$ B–W–F component is the one that is more likely to have predominantly A_{1g} symmetry, although we have also found that a thoroughly convincing identification awaits definitive polarization measurements [94].

7.3.4 Breit–Wigner–Fano Coupling Mechanism

We could not conclude from any of the resonant Raman scattering experiments (Chapters 4, 5, and 6) whether the B–W–F coupling of the phonon was to a multiphonon or an electronic continuum. Because the SERS process greatly increases the B–W–F line intensity, we can therefore conclude that the coupling mechanism responsible for the B–W–F lineshape is a surface-plasmon-based continuum. It is very apparent that the presence of the conduction electrons at the Fermi level plays a crucial role in the appearance of the B–W–F coupled lineshape for the SWNTs. It should be noted that only the *metallic* forms of the curved carbon structures (C_{60}, SWNT) exhibit the B–W–F lineshape, such as the $\sim 270\,\mathrm{cm}^{-1}$ Raman feature of K_3C_{60} ($1/q = -0.22$) [126], and the $\sim 1600\,\mathrm{cm}^{-1}$ feature of alkali-metal doped SWNTs ($1/q = -0.35$) [93] and metallic SWNTs ($1/q \sim -0.25$) [51]. The Raman bands of the insulating forms (undoped C_{60} and K_6C_{60} [126], and semiconducting SWNTs) exhibit only Lorentzian lineshapes. Our RRS and SERS experiments also show that the π-band free carrier plasmon is at a photon energy lower than $\hbar\omega_{phonon} = 0.19$ eV, based on the negative sign of the 1/q coupling term in the B–W–F lineshape [34].

Even though the intensity of the tangential G-band from semiconducting SWNTs is enhanced by 10 - 12 orders of magnitude [55] in the SERRS experiment, the

relative intensity of the Lorentzian oscillators in a fit to the G-band remain the same for SERRS relative to normal resonant Raman scattering (RRS) [20]. But for metallic SWNTs, not only is the intensity of the tangential G-band enhanced, but the ratio I_{1540}/I_{1580} is also enhanced due to the chemical SERRS effect [20]. Figure 7-8(a,b) shows the anti-Stokes tangential G-band spectra ($E_{\text{laser}} = 1.49\,\text{eV}$) collected while sample S3 was adsorbed on silver colloidal clusters [55]. Both anti-Stokes tangential G-band spectra were fit with similar (metallic) lineshapes, although the SERRS features are broader and the magnitude of the 1/q value is decreased slightly relative to the corresponding RRS feature (Fig. 7-8). However, the intensity ratio I_{1540}/I_{1580} is larger for SERRS (2.21) than for RRS (0.75) (see Table 7.2). Also the $1580\,\text{cm}^{-1}$ feature is enhanced by the chemical SERRS effect. When the $1592\,\text{cm}^{-1}$ Lorentzian oscillator is used for normalization in fits to the Stokes tangential G-band feature ($E_{\text{laser}} = 1.96\,\text{eV}$) from sample S3 [see Fig. 7-6], the ratio I_{1580}/I_{1592} increases slightly from 0.9 (RRS) to 1.1 (SERRS using gold and silver island films). The largest change still occurred for the $1540\,\text{cm}^{-1}$ B–W–F feature, with I_{1540}/I_{1592} increasing from RRS (3.5) to SERRS on gold (5.9) or on silver (7.2). The chemical mechanism of SERRS enhancement can be described as a resonant Raman effect involving electronic levels of the substrate and of the adsorbed SWNTs [20, 85]. Totally symmetric modes couple mostly to electronic excitations through a Franck–Condon mechanism, and are most affected by both an RRS process and the chemical SERRS effect, and so the behavior of the two metallic components are consistent with predominantly A (A_{1g}) symmetry [20]. Because the SERRS process greatly increases the B–W–F line intensity, we conclude that the coupling mechanism responsible for the B–W–F lineshape relates to the π-electron plasma continuum.

It is apparent that the presence of the conduction electrons at the Fermi level plays a crucial role in the appearance of the B–W–F coupled lineshape for the SWNTs, since only the *metallic* forms of the curved carbon structures exhibit the B–W–F lineshape. Our RRS and SERRS experiments also show that the π-band free carrier plasmon is at a photon energy lower than $\hbar\omega_{\text{phonon}} = 0.19\,\text{eV}$, based on the negative sign of the 1/q coupling term in the B–W–F lineshape [34]. The free carrier plasma resonance ($\hbar\omega_p$)

for graphite (calculated to be at 0.17 eV, experimentally set at 0.3 eV) [76], is higher than $\hbar\omega_p$ expected for metallic SWNTs (due to the nanotube's smaller carrier density relative to graphite). The screened free carrier plasma resonance has been reported to be $\hbar\omega_p = 0.15$ eV for multi-walled nanotubes [9], and below 0.2 eV for SWNTs [92, 119]. There is no such coupling (i.e., a B–W–F lineshape) of the G-band in graphite to the collective excitations of the electron gas (plasmons), since the longitudinal oscillations in the electron gas do not couple to the orthogonal in-plane vibrations in graphite. However, the curvature of the nanotubes breaks the symmetry, and coupling between the plasmons and the tangential G-band phonons with displacements in the circumferential direction can occur. We find experimentally that the B–W–F effect increases strongly with decreasing tube diameter (see Fig. 5-11), which supports this interpretation. Lin *et al.* [67] have performed calculations of the low frequency plasmons supported by an armchair carbon nanotube superlattice, and found acoustic plasmons that transfer their momentum *perpendicular* to the nanotubes axis which supports the argument for the differing amount of coupling of the two A (A_{1g}) modes from carbon nanotubes to the plasmons. In order to get more specific information about the surface plasmons on the hollow morphology of the carbon nanotubes, future calculations will be needed.

7.4 Conclusions

We have studied in detail the surface enhancement of resonance Raman scattering of SWNTs on silver and gold nanostructures. By looking at small changes between the RRS and SERRS spectra at various laser excitation energies for selected modes of the metallic nanotubes, we have found a small (factor of ~2) contribution of "chemical" SERRS enhancement to the very strong total enhancement factor inferred in previous work [55]. This finding is in agreement with RRS studies, which also show a stronger electron-phonon coupling for the metallic nanotubes as compared to the semiconducting nanotubes. Therefore changes in the electronic states which appear through interaction between the nanotubes and the metal substrate show up as changed SERRS

conditions for observing the related phonon bands. In principle, the electronic states for semiconducting nanotubes might also be changed by the interaction of the nanotubes with the metal. Wildöer *et al.* have reported [124] an interaction effect (resulting in a shift of the electronic density of states) between carbon nanotubes in contact with a smooth gold substrate in their STM/STS study of the electronic density of states in carbon nanotubes. However, due to the weaker electron-phonon coupling for semiconducting nanotubes, the surface interaction effect is too weak to be monitored in the SERRS spectra of the semiconducting nanotubes, except through our observations of a small upshift ($13\,\mathrm{cm}^{-1}$) in the G'-band frequency for semiconducting nanotubes, compared to the larger ($24\,\mathrm{cm}^{-1}$) upshift for the metallic nanotubes. Therefore, the fact that we did not find a charge transfer contribution to SERRS from the tangential mode in the semiconducting nanotubes does not prove that there is no electronic interaction between these tubes and the metal substrate. Because of the weaker electron-phonon coupling in semiconducting nanotubes, SERRS is simply not a sensitive enough tool to look for changes in their electronic states. But, our independent probe of measuring the upshift of the G' band in SERS, indicates a stronger interaction of the electronic states of the metallic nanotubes with the metal substrate than for the semiconducting nanotubes. The selective enhancement of modes which can be assigned to a totally symmetric mode (most significantly the $1540\,\mathrm{cm}^{-1}$ Breit-Wigner-Fano feature) is also in agreement with RRS and SERRS studies of molecules [19].

Chapter 8

Conclusions

8.1 Summary

Resonance Raman spectroscopy is an effective technique to probe not only the vibrational properties of carbon nanotubes, but also the electronic density of states, because the photon-assisted electronic transitions between the van Hove singularities in their 1-D electronic density of states results in a great increase in the Raman scattering cross-section of nanotubes relative to bulk graphite. Through comparing and contrasting the resonance Raman spectra of three different carbon nanotube samples, I have been able to provide guidelines to the science community on how to interpret the observed Raman spectra.

Resonance Raman spectroscopy for the first-order Raman spectra has identified features with completely different types of resonant behavior, which serve to provide different types information about the nanotubes. Experimentalists now use the frequencies of the radial breathing mode (RBM) feature to gauge the diameter distribution of the carbon nanotubes in their samples, since for isolated single-walled nanotubes $\omega_{\mathrm{RBM}} \propto 1/d_t$. The high frequency tangential G-band feature ($\sim$1600 cm^{-1}) has been shown to provide information about the electronic density of states of the carbon nanotubes, due to the resonant enhancement of the Raman band attributed to metallic carbon nanotubes in a narrow laser excitation window when either the incident laser or the scattered photon (or both) match the lowest energy allowed

electronic transition [89]. Polarized Raman spectroscopy studies [44] identified the symmetries [A (A_{1g}), E_1 (E_{1g}) and E_2 (E_{2g})] of the various components of the Raman tangential G-band feature attributed to the semiconducting nanotubes in the sample [94].

Whenever the broad, downshifted Raman G-band features attributed to metallic nanotubes have resonantly enhanced features in the Stokes window, these features have appeared as a superposition along with resonant Raman G-band features attributed to semiconducting nanotubes. By performing resonant Raman spectroscopy in the anti-Stokes window, I identified an unusual Stokes vs. anti-Stokes asymmetry due the 1-D electronic density of states of the carbon nanotubes causing completely *different* nanotubes being resonantly enhanced in the anti-Stokes and Stokes windows, which highlights the very important role of the scattered photon in the resonant Raman process. In performing resonant anti-Stokes Raman scattering, I have devised a means of collecting the Raman tangential G-band spectra from the metallic carbon nanotubes in our samples, completely devoid of those from semiconducting nanotubes. As a result, I was able to perform detailed analyses (Lorentzian oscillator vs. the Breit-Wigner-Fano lineshape) of the tangential "metallic" G-band feature, and in doing so reduced the number of components needed to fit the metallic band to only two ($1580\,\mathrm{cm}^{-1}$ and $\sim 1540\,\mathrm{cm}^{-1}$), and associated the various B-W-F lineshapes with different degrees of coupling to a continuum. I highlight here the very important role of curvature on the two different components of the tangential G-band feature of metallic carbon nanotubes in that: (1) the frequency of the phonon mode involving circumferential displacement of the carbon atoms ($\sim 1540\,\mathrm{cm}^{-1}$) appears at lower frequencies than the modes involving displacements along the tube axis due to the different force constants along the tube axis versus circumferentially, and (2) the curvature of the nanotube lowers the symmetry and causes greater coupling of the discrete phonon line to a continuum, resulting in a Breit-Wigner-Fano (interaction) lineshape for the $\sim 1540\,\mathrm{cm}^{-1}$ peak. The higher frequency component ($1580\,\mathrm{cm}^{-1}$) has a Lorentzian lineshape and is identified with atom displacements along the tube axis, which reproduce the situation in graphite and show no coupling to the continuum.

The sign of the interaction parameter (1/q) from the Breit-Wigner-Fano lineshapes is negative, which indicates that the coupling is to a continuum with lower energy than the discrete phonon line.

I have identified overtones and combination modes for the two dominant features in the first-order spectra, the radial breathing mode (ω_{RBM}) and the tangential mode (ω_{tang}). These features in the second-order spectra have been identified with the resonant Raman enhancement process arising from the 1D electronic density of states. Just as for the case of the first-order spectra, the resonant contributions to the second-order spectra also involve a different set of (n, m) nanotubes at each laser excitation energy E_{laser}. A second-order analog is observed for the broad spectral band identified with contributions from metallic nanotubes to the first-order tangential mode spectra. The unique feature of the second-order tangential overtone band shows a larger E_{laser} range over which the metallic nanotubes contribute. This effect is attributed to the large ($\hbar\omega_{\mathrm{phonon}} \sim 0.4\,\mathrm{eV}$) energy of these phonons and can be explained within the framework of the energy dependence of the electron 1D density of states. Combination modes associated with $(\omega_{\mathrm{tang}} + \omega_{\mathrm{RBM}})$ and $(\omega_{\mathrm{tang}} + 2\omega_{\mathrm{RBM}})$ have been identified, and show behaviors as a function of E_{laser} that are consistent with the behavior of their first-order constituents, namely that different nanotubes contribute to the spectra at each value of E_{laser}. Our results also indicate that the resonance process (electron-phonon coupling) occurs more strongly for metallic nanotubes than for semiconducting nanotubes. This increased electron-phonon coupling is evidenced by the presence of the G' band and the second-order features at $\omega^{M}_{\mathrm{tang}} + \omega_{\mathrm{RBM}}$ and at $\omega^{M}_{\mathrm{tang}} + 2\omega_{\mathrm{RBM}}$ in the metallic anti-Stokes spectrum at 1.58 eV, but their absence in the 1.96 eV semiconducting anti-Stokes spectrum. The much better resolution of the overtone of the radial breathing mode ($2 \times \omega_{\mathrm{RBM}}$) feature in the Stokes window when the incident laser energy is in the "metallic" energy window also indicates greater electron-phonon coupling through a Franck-Condon mechanism involving the A-term resonant Raman scattering process. These results also highlight the very important role of the *scattered* photon in the second-order resonant Raman process for the carbon nanotubes.

We have studied in detail the surface enhancement of resonance Raman scattering of SWNTs on silver and gold nanostructures. By looking at small changes between the RRS and SERRS (surface-enhanced resonant Raman scattering) spectra at various laser excitation energies for selected modes of the metallic nanotubes, we found a relatively small contribution (factor of 10^2) of "chemical" SERRS enhancement to the very strong total enhancement factor (factor of 10^{10} - 10^{12}) inferred in previous work [55]. This finding is in agreement with resonant Raman studies in the Stokes and anti-Stokes spectra, which also show a stronger electron-phonon coupling for the metallic nanotubes as compared to the semiconducting nanotubes. Therefore changes in the electronic states which appear through interaction between the nanotubes and the metal substrate show up as changed SERRS conditions for observing the related phonon bands. Due to the weaker electron-phonon coupling for semiconducting nanotubes, the surface interaction effect is too weak to be monitored in the SERRS spectra of the semiconducting nanotubes, except through our observations of a small upshift ($13\,\mathrm{cm}^{-1}$) in the G'-band frequency for semiconducting nanotubes, compared to the larger ($24\,\mathrm{cm}^{-1}$) upshift for the metallic nanotubes. Therefore the fact that we did not find a charge transfer contribution to SERRS from the tangential mode in the semiconducting nanotubes does not prove that there is no electronic interaction between these tubes and the metal substrate. Because of the weaker electron-phonon coupling in semiconducting nanotubes, SERRS is simply not a sensitive enough tool to look for changes in their electronic states. But, our independent probe of measuring the upshift of the G' band in SERS, indicates a stronger interaction of the electronic states of the metallic nanotubes with the metal substrate than for the semiconducting nanotubes. Totally symmetric modes couple most strongly to electronic excitations through a Franck-Condon mechanism (A-term), and are most affected by a resonance Raman experiment and by SERRS, and so the behavior of both metallic G-band features ($1580\,\mathrm{cm}^{-1}$ and $\sim 1540\,\mathrm{cm}^{-1}$) is consistent with predominantly A_{1g} symmetry. The SERS experiments have also served to identify the nature of the continuum resulting in the Breit-Wigner-Fano coupling as being electronic. We attribute this to a coupling between the discrete phonon and the free carrier plasmons and this coupling

is supported on metallic nanotubes. Since semiconducting nanotubes have a much lower free carrier density, the free carrier plasmon coupling mechanism is not operative for semiconducting nanotubes. Independent measurements have set the plasma resonance as occurring at an energy of ~ 0.15 eV in metallic SWNTs [92, 119], which is consistent with the negative sign of the interaction parameter that I have observed, indicating a coupling of the discrete phonon to a lower energy continuum.

8.2 Future Work

My thesis work has answered many of the questions that have been raised about carbon nanotubes, but there are still a number of new issues that need to be addressed in future work on the nanotubes. The intensity dependence and composition of the low frequency radial breathing mode feature (which is composed of $\omega_{\mathrm{RMB}} \propto 1/d_t$ for any carbon nanotube resonantly enhanced in the spectrum) as a function of $\mathrm{E_{laser}}$ has not been satisfactorily explained. Polarization experiments need to be performed to verify the that symmetry of the two Raman G-band features attributed to metallic tubes are indeed totally symmetric. While the intensity of the D-band ($\sim 1300\,\mathrm{cm}^{-1}$) of other sp^2 carbons increase monotonically relative to the tangential G-band ($\sim 1600\,\mathrm{cm}^{-1}$), there is no explanation for the fact that for carbon nanotubes the D-band intensity (relative to the tangential G-band) increases by an order of magnitude when the scattered photon is in the metallic resonance energy window. Even the second-order features we tentatively attributed to combination bands (and other groups have attributed to surface-plasmon-phonon coupling [48]) are better resolved in the Raman spectra in this narrow metallic energy window and more experiments are needed to explain the behavior of these combination bands as a function of the nanotube diameter. Even though the second-order scattering at the K-point is a non-resonant feature for other sp^2 carbons ($\sim 2430\,\mathrm{cm}^{-1}$), this feature is seen at a higher frequency ($\sim 2440\,\mathrm{cm}^{-1}$) when the scattered photon is in the metallic resonance window, than when semiconducting nanotubes are in resonance ($\sim 2420\,\mathrm{cm}^{-1}$). The experimental results from this thesis will contribute to the body of work needed to explain these

different behaviors.

My thesis work has also pointed out directions for research study on carbon nanotubes. In performing Raman spectroscopy for the anti-Stokes process, one is able to simultaneously probe completely *different* carbon nanotubes than for the Stokes process: for example, at selected E_{laser} it is possible for the anti-Stokes spectra to show resonance only with metallic tubes and the Stokes spectra only with semiconducting tubes, and vice versa. Therefore with a suitable choice of laser excitation energy for a given sample of carbon nanotubes with a narrow diameter distribution, such as E_{laser}=1.49 eV for tubes with d_t=1.49±0.2 nm (see Fig. 5-6), one could introduce dopants into the system or perform pressure experiments while monitoring the effect of these perturbations on the tangential G-band of metallic and semiconducting nanotubes sequentially. Through Near-Field microscopy it is possible to image an individual nanotube, but usually the amount of light is not enough to perform spectroscopy on the same nanotube. Enhancement factors of 10^{10} to 10^{12} have been achieved from the surface-enhanced resonance Raman spectroscopy experiments on carbon nanotubes [55]. These are very encouraging results and will eventually allow the study of the Raman spectra of a single, well characterized and imaged carbon nanotube. The answer to these questions I am sure will raise many more issues about the carbon nanotubes, which have already been the subject of lot of research effort over the last decade.

Bibliography

[1] A. Loiseau, private communication.

[2] T. Aizawa, R. Souda, S. Otani, Y. Ishizawa, and C. Oshima. *Phys. Rev. B*, 42:11469, 1990.

[3] H. Ajiki and T. Ando. Aharonov-bohm effect in carbon nanotubes. *Physica B, Condensed Matter*, 201:349, 1994.

[4] L. Alvarez, A. Righi, T. Guillard, S. Rols, E. Anglaret, D. Laplaze, and J.-L. Sauvajol. Resonant raman study of the structure and electronic properties of swnts. *Chem. Phys. Lett.*, 316:186–190, 2000.

[5] L. Alvarez, A. Righi, T. Guillard, S. Rols, E. Anglaret, D. Laplaze, and J.-L. Sauvajol. *Chem. Phys. Lett.*, 316:186, 2000.

[6] E. Anglaret, N. Bendiab, T. Guillard, C. Journet, G. Flamant, D. Laplaze, P. Bernier, and J. L. Sauvajol. *Carbon*, 36:1815, 1998.

[7] A. V. Baranov, A. N. Bekhterev, Y. S. Bobovich, and V. I. Petrov. *Opt. Spectrosc. USSR*, 62:612, 1987.

[8] L. X. Benedict, S. G. Louie, and M. L. Cohen. *Solid State Commun.*, 100:177–180, 1996.

[9] F. Bommeli, L. Degiorgi, P. Wachter, W. S. Bacsa, W. A. de Heer, and L. Forro. *Solid State Comm.*, 99:513, 1996.

[10] S. D. M. Brown, P. Corio, A. Marucci, M. S. Dresselhaus, M. A. Pimenta, and K. Kneipp. Anti-stokes raman spectra of single-walled carbon nanotubes. *Phys. Rev. B Rapid Comm.*, 61:R5137–R5140, 2000.

[11] S. D. M. Brown, P. Corio, A. Marucci, M. A. Pimenta, M. S. Dresselhaus, and G. Dresselhaus. Second-order resonant raman spectra of single-walled carbon nanotubes. *Phys. Rev. B*, 61:7734–7742, March 2000.

[12] A. Campion, J. E. Ivanecky III, C. M. Child, and M. J. Foster. *J. Am. Chem. Soc.*, 117:11807, 1995.

[13] A. Campion and P. Kambhampati. *Chem. Soc.*, 27:241, 1998.

[14] A. Charlier, E. McRae, M.-F. Charlier, A. Spire, and S. Forster. Lattice dynamics study of zigzag and armchair carbon nanotubes. *Phys. Rev. B*, 57:6689–6696, 1998.

[15] J.-C. Charlier, T. W. Ebbesen, and Ph. Lambin. Structural and electronic properties of pentagon-heptagon pair defects in carbon nanotubes. *Phys. Rev. B*, 53:11108, 1996.

[16] J.-C. Charlier and Ph. Lambin. Electronic structure of carbon nanotubes with chiral symmetry. *Phys. Rev. B*, 57:R15037, 1998.

[17] J.-C. Charlier and J. P. Michenaud. Energetics of multilayer carbon tubules. *Phys. Rev. Lett.*, 70:1858–1861, 1993.

[18] Jean-Christophe Charlier. Private communication.

[19] R. J. H. Clark and T. J. Dines. *Angewandte Chemie Int. Ed. Engl.*, 25:131, 1986.

[20] P. Corio, S. D. M. Brown, A. Marucci, M. A. Pimenta, , K. Kneipp, G. Dresselhaus, and M. S. Dresselhaus. Surface-enhanced resonant raman spectroscopy of single-wall carbon nanotubes adsorbed on silver and gold surfaces. *Phys. Rev. B*, 61, 2000. Submitted PRB on 10/27/99 MS #BK7404.

[21] P. Corio, J. C. Rubim, and R. Aroca. *Langmuir: ACS J. Surf. Colloids*, 14:4162, 1998.

[22] Q. Ding, Q. Jiang, Z. Jin, and D. Tian. *Fullerene Science & Technology*, 4:31, 1996.

[23] P. A. M. Dirac. *Proc. Roy. Soc. (London)*, 114:710, 1927.

[24] G. Dresselhaus, M. A. Pimenta, R. Saito, J.-C. Charlier, S. D. M. Brown, P. Corio, A. Marucci, and M. S. Dresselhaus. On the $\pi - \pi$ overlap energy in carbon nanotubes. In D. Tománek and R. J. Enbody, editors, *Science and Applications of Nanotubes*, New York, 1999. Kluwer Academic. Proceedings of the International Workshop on the Science and Applications of Nanotubes, Michigan State University, East Lansing, MI, USA, July 24-27, 1999.

[25] M. S. Dresselhaus. News and views 'new tricks with nanotubes'. *Nature (London)*, 391:19–20, 1998.

[26] M. S. Dresselhaus, G. Dresselhaus, and P. C. Eklund. *Science of Fullerenes and Carbon Nanotubes.* Academic Press, New York, NY, 1996.

[27] M. S. Dresselhaus, G. Dresselhaus, M. A. Pimenta, and P. C. Eklund. Raman scattering in carbon materials. pages 367–434, Oxford, UK, 1999. Blackwell Science Ltd. Analytical Applications of Raman Spectroscopy.

[28] M. S. Dresselhaus, G. Dresselhaus, and R. Saito. Carbon fibers based on c_{60} and their symmetry. *Phys. Rev. B*, 45:6234, 1992.

[29] M. S. Dresselhaus, G. Dresselhaus, and R. Saito. Physics of carbon nanotubes. *Carbon*, 33:883–891, 1995.

[30] M. S. Dresselhaus, G. Dresselhaus, K. Sugihara, I. L. Spain, and H. A. Goldberg. *Graphite Fibers and Filaments*, volume 5 of *Springer Series in Materials Science.* Springer-Verlag, Berlin, 1988.

[31] M. S. Dresselhaus, P. C. Eklund, and M. A. Pimenta. Fullerenes and related carbon-based materials. In W. Weber and R. Merlin, editors, *Raman Scattering in Materials Science*, Berlin, 1999. Springer-Verlag. in press.

[32] M. S. Dresselhaus, M. A. Pimenta, K. Kneipp, S. D. M. Brown, P. Corio, A. Marucci, and G. Dresselhaus. First and second-order resonant raman spectra of single-walled carbon nanotubes. In D. Tománek and R. J. Enbody, editors, *Science and Applications of Nanotubes*, pages 253–274, New York, 2000. Kluwer Academic. Proceedings of the International Workshop on the Science and Applications of Nanotubes, Michigan State University, East Lansing, MI, USA, July 24-27, 1999.

[33] G. S. Duesberg, W. J. Blau, H. J. Byrne, J. Muster, M. Burghard, and S. Roth. *Chem. Phys. Lett.*, 310:8, 1999.

[34] P. C. Eklund, G. Dresselhaus, M. S. Dresselhaus, and J. E. Fischer. *PRB*, 16:3330, 1977.

[35] P. C. Eklund, J. M. Holden, and R. A. Jishi. Vibrational modes of carbon nanotubes: spectroscopy and theory. *Carbon*, 33:959, 1995.

[36] U. Fano. *Phys. Rev.*, 124:1866, 1961.

[37] T. Hamada, M. Furuyama, T. Tomioka, and M. Endo. Preferred orientation of pitch precursor fibers and carbon fibers prepared from isotropic pitch. *J. Mater. Res.*, 7:1178–1188, 1992. ibid., 2612-2620.

[38] K. Harigaya. Lattice distortion and energy level structures of doped c_{70}. *Chem. Phys. Lett.*, 189:79, 1992.

[39] L. Henrard, A. Loiseau, C. Journet, and P. Bernier. *Euro. Journal of Phys.*, 2000.

[40] S. Iijima. *Nature (London)*, 354:56, 1991.

[41] R. A. Jishi, D. Inomata, K. Nakao, M. S. Dresselhaus, and G. Dresselhaus. Electronic and lattice properties of carbon nanotubes. *J. Phys. Soc. Jpn.*, 63:2252–2260, 1994.

[42] R. A. Jishi, L. Venkataraman, M. S. Dresselhaus, and G. Dresselhaus. Phonon modes in carbon nanotubules. *Chem. Phys. Lett.*, 209:77–82, 1993.

[43] A. Jorio. *Private communications.*

[44] A. Jorio, G. Dresselhaus, M. S. Dresselhaus, M. Souza, M. S. S. Dantas, M. A. Pimenta, A. M. Rao, R. Saito, C. Liu, and H. M. Cheng. Polarized raman study of single wall semiconducting carbon nanotubes. *Phys. Rev. Lett.*, 86, 2000.

[45] C. Journet, W. K. Maser, P. Bernier, A. Loiseau, M. Lamy de la Chapelle, S. Lefrant, P. Deniard, R. Lee, and J. E. Fischer. Large scale production of single-wall carbon nanotubes by the electric arc technique. *Nature (London)*, 388:756–758, 1997.

[46] D. Kahn and P. Lu. *Phys. Rev. B*, 60:6535, 1999.

[47] J. Kastner, J. Winter, and H. Kuzmany. Raman spectroscopy of conjugated caron systems: polymers, carbynes and fullerenes. *Mater. Sci. Forum*, 191:161–170, 1995.

[48] A. Kasuya. *Private communications.*

[49] A. Kasuya, M. Sugano, T. Maeda, Y. Saito, K. Tohji, H. Takahashi, Y. Sasaki, M. Fukushima, Y. Nishina, and C. Horie. *Phys. Rev. B*, 57:4999, 1998.

[50] H. Kataura, Y. Kumazawa, N. Kojima, Y. Maniwa, I. Umezu, S. Masubuchi, S. Kazama, X. Zhao, Y. Ando, Y. Ohtsuka, S. Suzuki, and Y. Achiba. Optical absorption and resonant raman scattering of carbon nanotubes. In H. Kuzmany, M. Mehring, and J. Fink, editors, *Proc. of the Int. Winter School on Electronic Properties of Novel Materials (IWEPNM'99)*, Woodbury, N.Y., 1999. American Institute of Physics. AIP conference proceedings (in press).

[51] H. Kataura, Y. Kumazawa, Y. Maniwa, I Umezu, S. Suzuki, Y. Ohtsuka, and Y. Achiba. *Synthetic Metals*, 103:2555, 1999.

[52] H. Kataura, Y. Kumazawa, Y. Maniwa, I. Umezu, S. Suzuki, Y. Ohtsuka, and Y. Achiba. Optical properties of single-wall carbon nanotubes. *Synthetic Metals*, 103:2555–2558, 1999.

[53] N. Khokhryakov, S. Savinskiĭ, and J. Molina. *JETP Lett. (Pis'ma Zh. Eksp. Teor.)*, 62:617, 1995.

[54] M. V. Klein. *Light Scattering in Solids*, page 169. Springer-Verlag, New York, 1975.

[55] K. Kneipp, H. Kneipp, P. Corio, S. D. M. Brown, K. Shafer, J. Motz, L. T. Perelman, E. B. Hanlon, A. Marucci, G. Dresselhaus, and M. S. Dresselhaus. Surface-enhanced and normal stokes and anti-stokes raman spectroscopy of single-walled carbon nanotubes. *Phys. Rev. Lett.*, 84:3470–3473, 2000.

[56] K. Kneipp, H. Kneipp, V. B. Kartha, R. Manoharan, G. Deinum, I. Itzkan, R. R. Dasari, and M. S. Feld. *Phys. Rev. E*, 57:R6281–R6284, 1998.

[57] K. Kneipp, H. Kneipp, R. Manoharan, E. B. Hanlon, I. Itzkan, R. R. Dasari, and M. S. Feld. *Appl. Spectrosc.*, 527:1493, 1998.

[58] K. Kneipp, Y. Wang, H. Kneipp, I. Itzkan, R. R. Dasari, and M. S. Feld. *Phys. Rev. Lett.*, 76:2444, 1996.

[59] K. Kneipp, Y. Wang, H. Kneipp, L. T. Perelman, I. Itzkan, R. R. Dasari, and M. S. Feld. *Phys. Rev. Lett.*, 78:1667, 1997.

[60] H. A. Kramers and W. Heisenberg. *Z. Phys.*, 31:681, 1925.

[61] J. Kürti, G. Kresse, and H. Kuzmany. *Phys. Rev. B*, 58:R8869, 1998.

[62] H. Kuzmany, B. Burger, M. Hulman, J. Kurti, A. G. Rinzler, and R. E. Smalley. Spectroscopic analysis of different types of single wall carbon nanotubes. *Europhys. Lett.*, 44:518–524, 1998.

[63] H. Kuzmany, B. Burger, A. Thess, and R. E. Smalley. Vibrational spectra of single wall carbon nanotubes. *Carbon*, 36:709–712, 1998.

[64] Ph. Lambin and V. Meunier. effective π-electron hamiltonian taking the curvature into account. In H. Kuzmany, J. Fink, M. Mehring, and S. Roth, editors, *Proceedings of the Winter School on Electronic Properties Novel Materials*, pages 504–508, 1998. Kirchberg Winter School, (AIP Conference proceedings 442, Woodbury, 1998).

[65] P. C. Lee and D. Meisel. *J. Phys. Chem.*, 86:3391, 1982.

[66] H. D. Li, K. t. Yue, Z. L. Lian, Y. Zhan, L. X. Zhou, S. L. Zhang, Z. J. Shi, Z. N. Gu, B. B. Liu, R. S. Yang, H. B. Yang, G. T. Zou, Y. Zhang, and S. Iijima. *Applied Phys. Lett.*, 76:2053, 2000.

[67] M. F. Lin. *Phys. Lett. A*, 259:158, 1999.

[68] C. Liu, H. T. Cong, F. Li, P. H. Tan, H. M. Cheng, K. Lu, and B. L. Zhou. *Carbon*, 37:1865, 1999.

[69] J. R. Lombardi, R. L. Birke, T. H. Lu, and J. Xu. *J. Chem. Phys.*, 84:4174, 1986.

[70] S. G. Louie. Carbon nanotubes, fibers, etc. In Wanda Andreoni, editor, *Physics and Chemistry of Materials with Low-Dimensional Structures: Fullerene-Based Materials*, page xx, New York, 1998. Marcel Dekker, Inc.

[71] O. Madelung. *Introduction to Solid State Theory*, chapter 1. Springer-Verlag, 1978.

[72] B. Marcus, L. Fayette, M. Mermoux, L. Abello, and G. Lucazeau. Analysis of the structure of multicomponent carbon films by resonant raman scattering. *J. Appl. Phys.*, 76:3463–3470, 1994.

[73] V. A. Markel, V. M. Shalaev, P. Zhang, W. Huynh, L. Tay, T. L. Haslett, and M. Moskovits. *Phys. Rev. B*, 59:10903, 1999.

[74] M. J. Matthews, M. A. Pimenta, G. Dresselhaus, M. S. Dresselhaus, and M. Endo. Origin of dispersive effects of the raman d-band in disordered carbon materials. *Phys. Rev. B*, 59:R6585, 1999.

[75] J. W. McClure. *Phys. Rev.*, 104:666, 1956.

[76] J. W. McClure. *IBM Journal*, page 255, 1964.

[77] M. Menon, E. Richter, and K. R. Subbaswamy. *J. Chem. Phys.*, 104:5875, 1996.

[78] T. P. Mernagh, R. P. Cooney, and R. A. Johnson. *Carbon*, 22:39, 1984.

[79] G. Mie. *Ann. Physik*, 25:377, 1908.

[80] J. W. Mintmire, B. I. Dunlap, and C. T. White. Are fullerene tubules metallic? *Phys. Rev. Lett.*, 68:631–634, 1992.

[81] J. W. Mintmire and C. T. White. Electronic and structural properties of carbon nanotubes. *Carbon*, 33:893, 1995.

[82] M. Moskovits. *Rev. Mod. Phys.*, 57:783 - 826, 1985.

[83] T. W. Odom, J. L. Huang, P. Kim, and C. M. Lieber. Atomic structure and electronic properties of single-walled carbon nanotubes. *Nature (London)*, 391:62–64, 1998.

[84] C. Oshima, T. Aizawa, R. Souda, Y. Ishizawa, and Y. Sumiyoshi. *Solid State Commun.*, 65:1601, 1988.

[85] A. Otto, I. Mrozek, H. Grabhorn, and W. Akemann. *J. Phys. Condens. Matter*, 4:1143, 1992.

[86] G. S. Painter and D. E. Ellis. *Phys. Rev. B*, 1:4747, 1970.

[87] M. A. Pimenta, E. B. Hanlon, A. Marucci, P. Corio, S. D. M. Brown, S. Empedocles, M. Bawendi, G. Dresselhaus, and M. S. Dresselhaus. The anomalous dispersion of the second-order raman g'-band in carbon nanotubes. *Brazilian J. Phys.*, page in press, 2000.

[88] M. A. Pimenta, A. Marucci, S. D. M. Brown, M. J. Matthews, A. M. Rao, P. C. Eklund, R. E. Smalley, G. Dresselhaus, and M. S. Dresselhaus. Resonant raman effect in single-wall carbon nanotubes. *J. Mater. Research*, 13:2396–2404, 1998.

[89] M. A. Pimenta, A. Marucci, S. Empedocles, M. Bawendi, E. B. Hanlon, A. M. Rao, P. C. Eklund, R. E. Smalley, G. Dresselhaus, and M. S. Dresselhaus. Raman modes of metallic carbon nanotubes. *Phys. Rev. B*, 58:R16016–R16019, 1998.

[90] I. Pocsik, M. Hundhausen, M. Koos, and L. Ley. *J. Non-Cryst. Solids*, 227-230 B:1083, 1998.

[91] M. Ramsteiner and J. Wagner. *Appl. Phys. Lett.*, 51:1355, 1987.

[92] A. M. Rao. *private communications.*

[93] A. M. Rao, P. C. Eklund, S. Bandow, A. Thess, and R. E. Smalley. *Nature*, 388:257, 1997.

[94] A. M. Rao, A. Jorio, M. A. Pimenta, M. S. S. Dantas, R. Saito, G. Dresselhaus, and M. S. Dresselhaus. Polarized raman study of aligned multiwalled carbon nanotubes. *Phys. Rev. Lett.*, 84:1820–1823, 2000.

[95] A. M. Rao, E. Richter, S. Bandow, B. Chase, P. C. Eklund, K. W. Williams, M. Menon, K. R. Subbaswamy, A. Thess, R. E. Smalley, G. Dresselhaus, and M. S. Dresselhaus. Infrared and raman spectroscopic studies of single-wall carbon nanotubes. *Science*, 275:187–191, 1997.

[96] G. A. M. Reynolds, A. W. P. Fung, Z. H. Wang, M. S. Dresselhaus, and R. W. Pekala. *Phys. Rev. B*, 50:18590, 1994.

[97] E. Richter and K. R. Subbaswamy. Theory of size-dependent resonance raman scattering from carbon nanotubes. *Phys. Rev. Lett.*, 79:2738, 1997.

[98] D. H. Robertson, D. W. Brenner, and J. W. Mintmire. Energetics of nanoscale graphitic tubules. *Phys. Rev. B*, 45:12592, 1992.

[99] R. Saito. Private communication.

[100] R. Saito, G. Dresselhaus, and M. S. Dresselhaus. Topological defects in large fullerenes. *Chem. Phys. Lett.*, 195:537, 1992.

[101] R. Saito, G. Dresselhaus, and M. S. Dresselhaus. Electronic structure of double-layered graphene tubules. *J. Appl. Phys.*, 73:494, 1993.

[102] R. Saito, G. Dresselhaus, and M. S. Dresselhaus. *Physical Properties of Carbon Nanotubes.* Imperial College Press, London, 1998.

[103] R. Saito, G. Dresselhaus, and M. S. Dresselhaus. Trigonal warping effect of carbon nanotubes. *Phys. Rev. B*, 61:2981–2990, 2000.

[104] R. Saito, M. Fujita, G. Dresselhaus, and M. S. Dresselhaus. Electronic properties of carbon fibers based on c_{60}. In L. Y. Chiang, A. F. Garito, and D. J. Sandman, editors, *Electrical, Optical and Magnetic Properties of Organic Solid State Materials, MRS Symposia Proceedings, Boston*, volume 247, page 333, Pittsburgh, PA, 1992. Materials Research Society Press.

[105] R. Saito, M. Fujita, G. Dresselhaus, and M. S. Dresselhaus. Electronic structure of chiral graphene tubules. *Appl. Phys. Lett.*, 60:2204–2206, 1992.

[106] R. Saito, M. Fujita, G. Dresselhaus, and M. S. Dresselhaus. Electronic structures of carbon fibers based on c_{60}. *Phys. Rev. B*, 46:1804–1811, 1992.

[107] R. Saito, T. Takeya, T. Kimura, G. Dresselhaus, and M. S. Dresselhaus. Raman intensity of single-wall carbon nanotubes. *Phys. Rev. B*, 57:4145–4153, 1998.

[108] R. Saito, T. Takeya, T. Kimura, G. Dresselhaus, and M. S. Dresselhaus. Finite size effect on the raman spectra of single-wall carbon nanotubes. *Phys. Rev. B*, 59:2388–2392, 1999.

[109] Y. Saito, Y. Tani, N. Miyagawa, K. Mitsushima, A. Kasuya, and Y. Nishina. High yield of single wall carbon nanotubes by arc discharge using rh-pt mixed catalysts. *Chem. Phys. Lett.*, 294:593–598, 1998.

[110] D. Sanchez-Portal, E. Artacho, J. M. Soler, A. Rubio, and P. Ordejón. Ab initio structural, elastic, and vibrational properties of carbon nanotubes. *Phys. Rev. B*, 59:12678–12688, 1999.

[111] K. Sattler. Stm analysis of carbon nanotubes and nanocones. *Carbon*, 33:915–920, 1995.

[112] J. F. Scott. *Rev. Mod. Phys.*, 46:83, 1974.

[113] V. M. Shalaev and M.I. Stockman. *Sov. Phys. JETP*, 65:287, 1987.

[114] T. G. Spiro. *Biological Applications of Raman Spectroscopy.* John Wiley & Sons, 1987.

[115] M. I. Stockman, V. M. Shalaev, M. Moskovits, R. Botet, and T. F. George. *Phys. Rev. B*, 46:2821, 1992.

[116] M. Sugano, A. Kasuya, K. Tohji, Y. Saito, and Y. Nishina. Resonance raman scattering and diameter-dependent electronic states in single-wall carbon nanotubes. *Chem. Phys. Lett.*, 292:575–579, 1998.

[117] K. Tanaka, M. Okada, K. Okahara, and T. Yamabe. Structure and electronic state of c_{60}^{-}. *Chem. Phys. Lett.*, 191:469, 1992.

[118] A. Thess, R. Lee, P. Nikolaev, H. Dai, P. Petit, J. Robert, C. Xu, Y. H. Lee, S. G. Kim, A. G. Rinzler, D. T. Colbert, G. E. Scuseria, D. Tománek, J. E. Fischer, and R. E. Smalley. Crystalline ropes of metallic carbon nanotubes. *Science*, 273:483–487, 1996.

[119] A. Ugawa, A. G. Rinzler, and D. B. Tanner. Far-infrared gaps in single-wall carbon nanotubes. *Phys. Rev. B*, 60:R11305, 1999.

[120] U. D. Venkateswaran, A. M. Rao, E. Richter, M. Menon, A. Rinzler, R. E. Smalley, and P. C. Eklund. Probing the single wall carbon nanotube bundle: A raman scattering study under high pressure. *Phys. Rev. B*, 59:10928, 1999.

[121] R. P. Vidano, D. B. Fishbach, L. J. Willis, and T. M. Loehr. *Solid State Commun.*, 39:341, 1981.

[122] Y. Wang, D. C. Alsmeyer, and R. L. McCreery. *Chem. Mater.*, 2:557, 1990.

[123] C. T. White and T. N. Todorov. Carbon nanotubes as long ballistic conductors. *Nature (London)*, 393:240, 1998.

[124] J. W. G. Wildöer, L. C. Venema, A. G. Rinzler, R. E. Smalley, and C. Dekker. Electronic structure of carbon nanotubes investigated by scanning tunneling spectroscopy. *Nature (London)*, 391:59–62, 1998.

[125] J. Yu, K. Kalia, and P. Vashishta. Phonons in graphitic tubules. *J. Chem. Phys.*, 103:6697, 1995.

[126] P. Zhou, K.-A. Wang, A. M. Rao, P. C. Eklund, G. Dresselhaus, and M. S. Dresselhaus. *PRB*, 45:10838, 1992.